Aeroacoustic Study of a Model-Scale Landing Gear in a Semi-Anechoic Wind-Tunnel

Marcel C. Remillieux

Thesis submitted to the Faculty of the Virginia Polytechnic Institute and State University
in partial fulfillment of the requirements for the degree of

Master of Science
in
Mechanical Engineering

Dr. Ricardo A. Burdisso, Co-Chair
Dr. Wing F. Ng, Co-Chair
Dr. Saad A. Ragab

March 19, 2007
Blacksburg, Virginia

Keywords: Phased Array, Landing Gear Noise, Conventional Beamforming, Beamforming in Flow, Hard-Walled Wind Tunnel, Semi-Anechoic Wind Tunnel, Passive Noise Control.

Aeroacoustic Study of a Model-Scale Landing Gear in a Semi-Anechoic-Wind-Tunnel

Marcel C. Remillieux

ABSTRACT

An aeroacoustic study was conducted on a 26%-scale Boeing 777 main landing gear in the Virginia Tech (VT) Anechoic Stability Wind Tunnel. The VT Anechoic Stability Wind Tunnel allowed noise measurements to be carried out using both a 63-elements microphone phased array and a linear array of 15 microphones. The noise sources were identified from the flyover view under various flow speeds and the phased array positioned in both the near and far-field. The directivity pattern of the landing gear was determined using the linear array of microphones. The effectiveness of 4 passive noise control devices was evaluated. The 26%-scale model tested was a faithful reproduction of the full-scale landing gear and included most of the full-scale details with accuracy down to 3 mm. The same landing gear model was previously tested in the original hard-walled configuration of the VT tunnel with the same phased array mounted on the wall of the test section, i.e. near-field position. Thus, the new anechoic configuration of the VT wind tunnel offered a unique opportunity to directly compare, using the same gear model and phased array instrumentation, data collected in hard-walled and semi-anechoic test sections.

The main objectives of the present work were (i) to evaluate the validity of conducting aeroacoustic studies in non-acoustically treated, hard-walled wind tunnels, (ii) to test the effectiveness of various streamlining devices (passive noise control) at different flyover locations, and (iii) to assess if phased array measurements can be used to estimate noise reduction.

As expected, the results from this work show that a reduction of the background noise (e.g. anechoic configuration) leads to significantly cleaner beamforming maps and allows one to locate noise sources that would not be identified otherwise. By using the integrated spectra for the baseline landing gear, it was found that in the hard-walled test section the levels of the landing gear noise were overestimated.

Phased array measurements in the near and far-field positions were also compared in the anechoic configuration. The results showed that straight under the gear, near-field measurements located only the lower-truck noise sources, i.e. noise components located behind the truck were shielded. It was thus demonstrated that near-field, phased-array measurements of the landing gear noise straight under the gear are not suitable. The array was also placed in the far-field, on the rear-arc of the landing gear. From this position, other noise sources such as the strut could be identified. This result demonstrated that noise from the landing gear on the flyover path cannot be characterized by only taking phased array measurement right under the gear.

The noise reduction potential of various streamlining devices was estimated from phased array measurements (by integrating the beamforming maps) and using the linear

array of individually calibrated microphones. Comparison of the two approaches showed that the reductions estimated from the phased array and a single microphone were in good agreement in the far-field. However, it was found that in the near-field, straight under the gear, phased array measurements greatly overestimate the attenuation.

To Elisha and Estella

ACKNOWLEDGEMENTS

First, I would like to thank my advisor, Dr. Ricardo Burdisso, and my co-advisor, Dr. Wing Ng for having given me the opportunity to enter Virginia Tech and work for them as a graduate research assistant. I am grateful to them for always encouraging my creativity during the course of this project and for giving me independence in my work.

I would like to express my sincere gratitude to Dr. Saad Ragab for behind part of my committee.

I would like to thank Dr. Patricio Ravetta who provided his beamforming code to post-process the acoustic data. I also appreciate his help and insights throughout this project.

The completion of this work would not have been possible without Mr. Hugo Camargo. I have greatly appreciated his help for setting up the experiments of noise measurements in the wind tunnel throughout the summer 2006.

Many people in the Vibration and Acoustics Laboratories have volunteered their time to help and I would like to thank them all.

I would like to dedicate this work to Elisha and to our daughter, Estella.

TABLE OF CONTENTS

INDEX OF FIGURES

Page

INDEX OF TABLES

Page

1 INTRODUCTION

In less than a century, the invention of the Wright brothers has become one of the major means of transportation for individuals and freight. A fact of this expansion is the current 29 millions jobs globally generated by the air transport industry. We could also enumerate the various sectors of an economy that depend on this industry. In order to ensure their commercial success, aircraft and aircraft engine manufacturers have made significant progress in fuel efficiency and noise reduction over the past decades. Therefore, aircraft entering today's fleets are 75% quieter and 70% more fuel efficient than comparable aircraft 40 years ago. The fuel efficiency responds to a direct demand of the airlines and freight companies to fly at lower cost, and the noise reduction responds to the stringent regulations imposed by the aviation authorities to reduce the environmental impact of aircraft.

Aircraft noise began being an issue in the late 1950s with the introduction of turbojet engines that increased the level of noise on many aircraft. Rapidly, the "noise pollution" generated by these new aircraft prompted complaints among the communities surrounding the airports. The first attempts in regulating aircraft noise include the rules imposed by the airport authorities of London Heathrow and New York JFK airports that constrained long range aircraft to take off at reduced weight so that they could get farther from populated areas faster. More standardized regulations were later imposed by the Federal Aviation Administration with the firm intention to have technologies developed toward quieter aircraft. Earliest efforts were focused on reducing engine noise. Some solutions were proposed such as, venting the exhaust with tubes or corrugating the outer edge of the exhaust nozzle, but provided only marginal results. In the 1970s, the development of high bypass ratio turbofan engines, prompted by the need of greater thrust and fuel efficiency that the new generation of aircraft required, achieved some significant noise reduction.

At take-off, maximum engine power is required and engine constitutes the principal noise source in spite of the significant progress in engine noise reduction over the past decades. However, on approach to landing, aircraft operate at lower thrust and airframe

noise has become comparable to engine noise. In the case of some modern aircraft, airframe has even become the predominant noise source in the landing phase. Besides, in traditional approaches, aircraft begin descending many miles from the runway, spending substantial time at relatively low altitude, as shown in Figure 1.1. Expected increases in air traffic associated with the fact that many airports are surrounded by highly populated areas is likely to reinforce the noise impact on the communities as well as the need for further airframe noise reduction.

Figure 1.1: Aircraft approaching the Hong Kong International airport [1]

1.1 Literature review

With the development of quieter turbofan engines, airframe noise has become a major component of the overall noise generated by an aircraft in its landing configuration. Research in airframe noise reduction began in the 1970s. Basic insights were gained such as by Heller and Dobrzynski [2] who showed that, in its landing configuration, an aircraft generates a level of noise 10 dB higher than in its cruise configuration. More recent studies revealed that high lift devices (flaps and slats) and landing gears are the components contributing the most to the airframe noise [3]. Airframe noise is also highly dependent on aircraft size. In the case of large capacity aircraft, airframe noise is dominated by landing gears [4]. The relevance of investigating landing gear noise is thus emphasized by the current tendency of the aircraft manufacturers to design super-sized aircraft such as the A380 of Airbus.

A landing gear is a very complex structure primarily designed to support the load of a landing aircraft. In order to ease inspection and maintenance, the aerodynamic design is not refined. As a result, many components such as, hydraulic cables, electric wiring, torque links, front and rear braces are exposed to the air flow. Flow separation over the landing gear components constitutes the potential noise source mechanism through unsteady wake flow and large-scale vortex instability and deformation [5]. On the other hand, the magnitude of the sources is determined by their aerodynamic load, a function of the 6th power of flow velocity [6]. As pointed out by Heller and Dobrzynski [2], from the main landing gear components, low frequency noise will be radiated whereas small elements such as wire hoses, screw holes, and so forth, will generate high frequency noise. It was also shown in a later investigation on a full-scale A320 landing gear, by Dobrzynski and Buchholz [4], that aerodynamic noise is essentially broadband. Moreover, noise levels in 1/3 octave bands are almost constant from low frequencies up to few thousands Hz.

After having been set aside for about a decade, airframe noise regained interest in the 1990s. In October 1993, NASA started a major noise reduction program, AST (Advanced Subsonic Technology). This program aimed to develop technologies to ensure that the U.S. aviation industry would be prepared to meet the demands placed on the aviation system by growing traffic volume and safety requirements. The AST Program called for 10 EPNLdB (Effective Perceived Noise Levels) over 1992 technology [7,8]. As opposed to the 1970s, this new era of research has been focused on specific components of the airframe. This has been eased by the simultaneous development of measurement "tools" such as microphone phased arrays and elliptic mirrors. The advent of microphone phased arrays has also made possible the investigation of airframe noise in hard-walled wind tunnels.

Traditionally, open-jet and hard-walled wind tunnels are the two types of facility where aeroacoustic measurements are performed. Open-jet wind tunnels offer a large space in an anechoic environment but achieve a lower maximum Reynolds number than hard-walled wind tunnels. When a small-scale model is tested, a high Reynolds number

is required to keep the dimensionless parameters constant with regard to the full-scale model. In this case, hard-walled wind tunnels are preferred. However, if these facilities are not acoustically treated, background noise levels are relatively high and in some cases may exceed the noise radiated from the model tested. The major wind-tunnel components that contribute to the background noise are the drive fan, flow through tunnel circuit components such as corner turning vanes and screens, wall boundary layer from high speed flow in the test section in the case of hard-walled wind tunnels or shear layer turbulence in the case of open-jet wind tunnels [9]. The importance of these sources usually varies from one facility to another. The background noise issue was first overcome by testing in anechoic facilities. The advent of microphone phased arrays has then offered the advantage over a single, or possibly a pair of microphones, of locating noise sources and performing accurate acoustic measurement regardless of the background noise. In other words, microphone phased arrays allow aeroacoustic testing to be conducted in hard-walled wind tunnels. Before the Virginia Tech (VT) Stability Wind Tunnel was upgraded to an anechoic facility, only open-jet wind tunnels were acoustically treated. The VT wind tunnel is an alternative to hard-walled and open-jet wind tunnels. The hard-walls of the test section were replaced by stretched Kevlar membranes with low acoustic impedance. Anechoic chambers were mounted on the sides of the test section which allowed the acoustic instrumentation to be located in the far-field, outside the flow. This hybrid facility is open from an acoustic point of view and closed from a fluid point of view. More details about the facility are given in Section 2.2.

Full-scale models are rarely tested. Most of the recent experimental airframe noise research has been performed using small-scale models, [3,10-13]. Dobrzynski et al. pointed out the difficulty of using model-scale results for full-scale noise predictions due to the lack of details in the geometrical modeling, [2]. Therefore, it was suggested that experimental airframe noise research should be based on full-scale aircraft landing gears. Although open-jet wind tunnel tests on full-scale models were performed successfully [14,15], they do not represent a cost-effective way to investigate airframe noise, mainly because the facilities required as well as the experimental setup need to be extremely large. Working with full-scale models also reduces the ease in changing configurations.

In order to reduce the gap between full-scale flight tests and wind tunnel tests on small-scale models, Boeing and Rolls-Royce joined their efforts in the Quiet Technology Demonstrator (QTD) program that took place in Glasgow, MT, in September 2001. A total of 60 hours of flight test was performed using a Boeing 777-200ER with Rolls Royce Trent 800 engines. Although the primary purpose of this program was to evaluate the engine noise reduction concepts developed from model-scale research, airframe noise flight tests were also conducted. Data was collected using over 200 microphones and a phased array located on the flyover path of the aircraft. As a continuation of the QTD program, Boeing, associated with General Electric Aircraft Engines, Goodrich Corporation, NASA, and All Nippon Airways, conducted a three-week flight test program in 2005 under the name QTD2 [16]. More details about the program are given in reference [17]. During these tests, a fairing designed by Goodrich was mounted on the 777's main landing gear. Because the program is relatively recent, no literature is yet available to discuss the performance of the fairing.

The gear fairing used in the fly-test was based on the measurements and evaluation of multiple fairing designs tested on a small-scale gear model in a hard-wall wind-tunnel. To this end, a high-fidelity 26%-scale 777's main landing gear was used [11-13,18-20]. Through the incorporation of complex parts made by stereo lithography up to an accuracy of 3 mm in full-scale, this model addressed the issues associated with the low fidelity models used in past investigations. Figure 1.2 depicts the 26%-scale Boeing 777 main landing gear as mounted in the Virginia Tech (VT) Stability Wind Tunnel, hard-walled test section and fitted with a model-scale lower truck fairing [21].

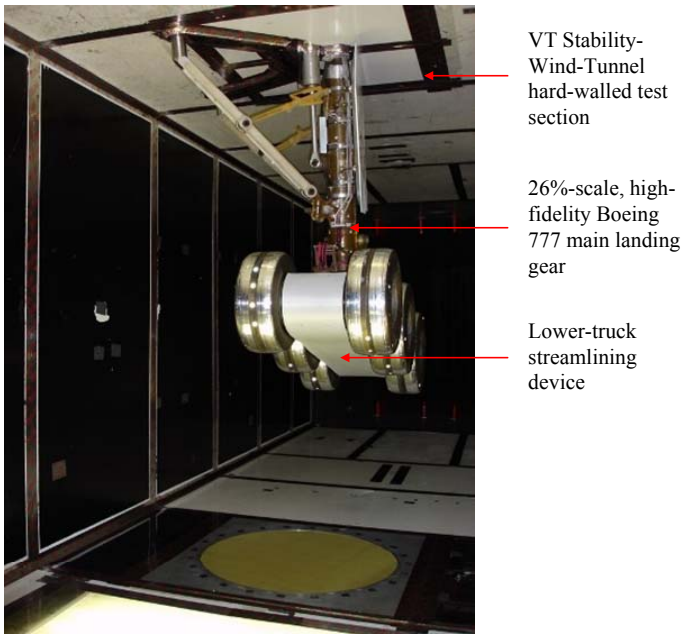

Figure 1.2: A photograph of the 26%-scale, high fidelity Boeing 777 main landing gear as mounted in the Virginia Tech (VT) Stability Wind Tunnel, hard-walled test section and fitted with the model-scale lower-truck fairing [21].

As a first step in noise control design, new insights were gained in the noise generation mechanisms of this particular landing gear. Stoker and Sen [13], Stoker et al. [18] and Horne et al. [19] investigated the airframe noise of the Boeing 777, using 6.3%- and 26%-scale models. Detailed high lift systems and landing gears (low and high fidelity) were mounted on a semi-span 26%-scale Boeing 777. The presence of a landing gear – flap interaction was pointed out from the tests. It was also shown that discrepancies exist between the low and high fidelity models and between the flight and wind tunnel tests. Although the landing gear noise was present in the three scales, the fact of using a higher level of fidelity produced more sound at higher frequencies, which is in agreement with previous investigations [2]. The possible reasons for the discrepancies observed between flight and wind tunnel tests were given as: the significant variations of the Reynolds number between full- and model-scale airframes, the difficulty to maintain constant speed when testing in flight, the fact that different methods were used to locate the noise sources and the lack of details on some of the components of the model-scale airframe.

Jaeger et al.,[11], Burnside et. al [20], and Ravetta et al. [12] conducted aeroacoustic studies on the high fidelity 26%-scale 777 landing gear, isolated, in hard wall wind tunnel. Noise sources of the landing gear were identified and ranked according to their sound level. In term of noise reduction, only an estimate was given based on idealized configurations of the landing gear. It was speculated that noise could be reduced from 2 to 6 dB through careful design of the main components of the landing gear and some additional reduction could be achieved via fairings and streamlining. As mentioned by Lazos, [22], high frequency noise is generated by small components and can be easily suppressed through streamlining. Low frequency noise is associated with the major landing gear components and streamlining that allows easy access to the gear for inspection and maintenance is not trivial. A prototype of the fairing designed for the QTD2 program was tested on the high fidelity 26%-scale landing gear in the VT Stability Wind Tunnel and showed that a noise reduction of 3 dB was achievable (results not published yet).

Within the European homologue of the AST program started in 1998 and known as RAIN (Reduction of Airframe and Installation Noise), Dobrzynski et al. [15] investigated some noise reduction devices on full-scale Airbus 340 nose- and main landing gears. Figure 1.3 depicts a full-scale Airbus 340 main landing gear fitted with various streamlining devices such a bogie beam undertray, brake fairings, wheel caps, leg door filler, and articulated link cover. Dobrzynski et al. [15] were able to reduce noise by as much as 3 dB, which is consistent with the results obtained more recently from the QTD2 program.

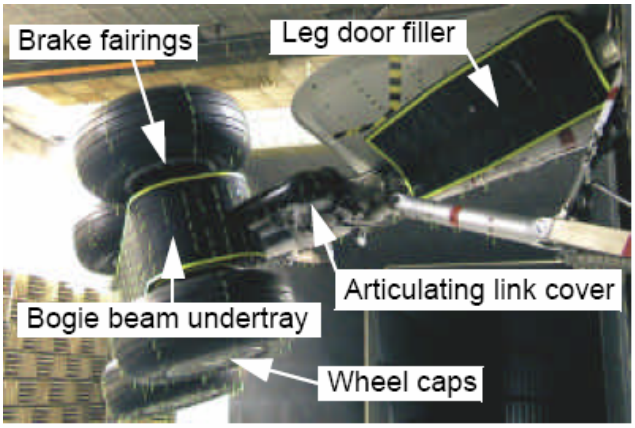

Figure 1.3: Passive noise control devices mounted on the Airbus 340 main landing gear [15].

More advanced methods to control landing gear noise have been attempted. Thomas et al. [23] proposed plasma actuators to control flow separation from a generic landing gear model. They were shown to be effective in reducing flow separation and associated vortex shedding. Unfortunately, the implementation of such devices is not trivial and the research being at its early stage, their noise reduction potential has not been evaluated yet.

Predicting accurately airframe noise would be desirable. This would allow accounting for aerodynamic aspects and its noise in the early design stages of an aircraft. It would also significantly reduce the cost associated with wind tunnel and flight testing. In the few numerical investigations on landing gear noise [24-27], flow field computations were performed in the near-field and noise was predicted in the far-field using the Ffowcs Williams-Hawkings (FW-H) equation [28]. Unfortunately, memory limitations of current computers restrain the study to very simplified landing gears. To address these limitations, other methods have been considered to predict noise. These include a semi-empirical model, which is based on a data base of full-scale tests [29]; a statistical model that classifies the landing gear components into three groups: low, medium, and high frequencies, so as to consider more detailed landing gears [30]; and a directivity pattern approach [31]. Since accurate models to predict landing gear noise are not available yet, experimental investigations remain necessary for landing gear noise reduction.

1.2 Objectives

Many investigations on landing gear noise have been conducted in hard-walled wind tunnels. Although it allows one to work at higher Reynolds number than in open-jet wind tunnel, it also includes some limitations,

1. Measurements are often taken in the near field, due to the space limitation in the wind-tunnel test section.
2. Tests conducted in hard-walled wind tunnel are subjected to acoustic-wave reflections on the walls of the test section. For the case of a model semi-span symmetry plane, it was shown that the reverberation at the center of the test section could be responsible for some discrepancies in the aeroacoustic noise measurement, [32]. More generally, the interaction between direct and reflected waves results in the corruption of the sound field.
3. Background noise might, in some cases, be higher than the sound from the model tested.
4. Usually, the aeroacoustic model is located in the flow stream whereas the sensor is outside the flow. Sound passes through the boundary layer (or shear layer in the case of open-jet wind tunnels) before reaching the sensor. It was shown that when elliptic mirrors or phased arrays are used, the loss of coherence of the acoustic wave passing through the boundary or shear layer, results in the loss of effective gain of the sensor and leads to estimated sources levels that are too low [33].

In the herein study, the noise source identification on a 26%-scale 777 main landing gear model is discussed. Aeroacoustic tests on this model have already been performed in the VT Stability Wind Tunnel, and specific noise sources could be located through the use of a microphone phased array [12]. In July 2006, the VT Stability Wind Tunnel was upgraded to an anechoic facility (for a detailed description, see Section 2.2). This new configuration of the VT wind tunnel offered a unique opportunity to directly compare, using the same landing gear model, data collected in hard-walled and semi-anechoic test sections. The specific objectives of this study are:

a. To evaluate the validity of conducting aeroacoustic studies in non-acoustically treated, hard-walled wind tunnels.

The background noise in the semi-anechoic VT wind tunnel was significantly lower than hard-walled wind tunnels. The effects of the acoustic environment on phased array measurement are discussed through a comparison between hard-walled and semi-anechoic, near-field, phased-array data.

In Ravetta et al. [12] study, the measurement systems were in the geometric near-field of the model because of the dimensions of the hard-walled test section. When measurements are taken in the near-field, the acoustic field is not strictly representative of the sound propagating to the far-field. Unlike in the far-field, in the near-field results cannot be integrated. Therefore, if measurements are taken in the near-field, they need to be extrapolated. To do so, it is necessary to know each source location of the model tested and extrapolate from each source to the far-field, which is allowed by the phased array technology. Using the new configuration of the wind tunnel, acoustic data was collected at various locations in the far-field, on the flyover path. The validity of collecting acoustic data in the near-field was investigated by comparing data collected in the semi-anechoic wind tunnel in the near-field and in the far-field.

b. To test the effectiveness of various streamlining devices (passive noise control).

The performance of various streamlining devices was tested in hard-walled wind tunnel by Ravetta et al. [12]. In the herein study, the effectiveness of these streamlining devices on the flyover path was tested again but in an environment suitable for aeroacoustic measurements.

c. To assess if phased array measurements can be used to estimate noise reduction

Additional acoustic measurements were taken in the semi-anechoic wind tunnel with a linear array of 15 microphones located in the far-field. The noise reduction of the various streamlining devices measured with the linear array is compared to the far-field, phased-array results.

1.3 Organization

This thesis is organized in four chapters and two appendices. Chapter 1 is an introduction to the problem studied and a comprehensive literature review on landing gear noise. In this chapter, the objectives of this study are also presented. Chapter 2 describes the experimental setup for measurement of the landing gear noise. This includes the model scale gear, the semi-anechoic test section of the VT Stability Wind Tunnel, the instrumentation, and the tests configurations. Chapter 3 reports the experimental results. First, phased array data collected in hard-walled and semi-anechoic test sections are compared to evaluate the effects of the acoustic environment on phased array measurement. Then, the validity of taking phased array measurements in the near field is discussed by comparing acoustic data collected in the near- and far-field in the semi-anechoic wind tunnel. Finally, the effectiveness of various passive noise control devices is evaluated from far-field phased array measurements. Chapter 4 presents the main conclusions of the work presented in this thesis.

Appendix A presents a brief derivation of the conventional beamforming algorithm. Some elements of theoretical acoustics necessary to modify the conventional beamforming algorithm so as to account for flow effects are also presented. Appendix B reports results from preliminary tests conducted in the VT semi-anechoic wind tunnel. First, tests were conducted to validate the theoretical approach developed in Appendix A. Then, a calibration procedure for the array levels is described.

2 EXPERIMENTAL SETUP

This chapter describes the experimental setup for measurements of the landing gear noise. This chapter is divided in subsections describing the high fidelity 26%-scale landing gear, the noise control devices, the new test section of the VT Stability Wind Tunnel, the instrumentation, and the testing configurations.

2.1 The high fidelity 26%-scale 777 main landing gear model

Experiments were conducted using a high fidelity 26%-scale model of the Boeing 777 main landing gear. The model was originally tested by Horne et al. [19] in the NASA Ames 40- by 80-ft wind tunnel as a part of the STAR (Subsonic Transport Aeroacoustic Research) program. It was designed to address the issues associated with low fidelity models. Figure 2.1 depicts CAD drawings (braces-side and bottom views) of the Boeing 777 gear and a photograph of the landing gear model. Key gear components are also identified in this figure. The major parts constituting the primary structural framework were made of steel and aluminum. Using stereo lithography, most of the full-scale details were reproduced with accuracy down to 3 mm in full scale. The details include wheel hubs, brakes cylinders, hydraulic valves, and so forth. Other significant details, not present in the low-fidelity model, are the hydraulic lines and cables that were reproduced using electrical wires. Note that in the CAD drawings, the lower truck is at an angle of attack of 0°, whereas during the tests it was set at 13°.

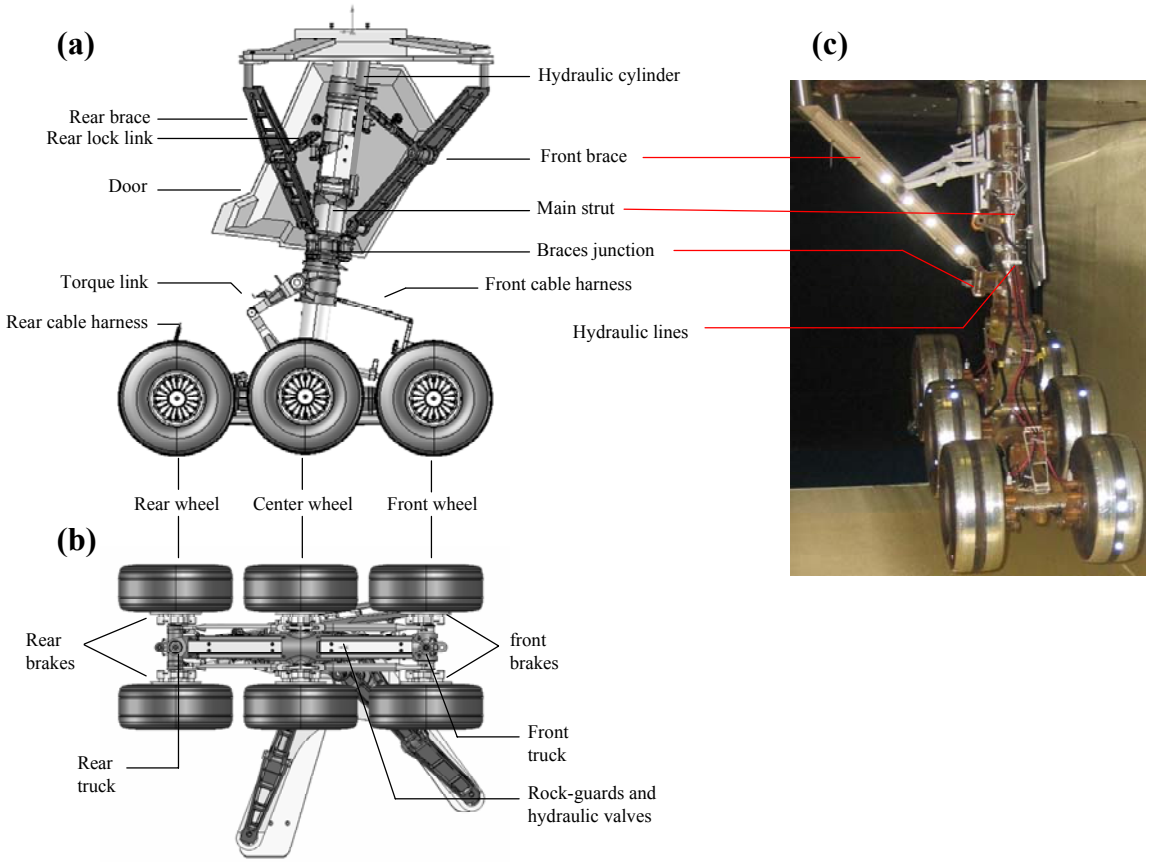

Figure 2.1: CAD drawings, braces-side view (a) and bottom view (b), and a photograph (c) of the high fidelity 26%-scale Boeing 777 main landing gear model.

Figure 2.2 is a photograph of the full-scale Boeing 777-200 main landing gear. Although the model depicted in Figure 2.1 is a very faithful representation of the full-scale gear, several details were omitted. The small door mounted on the top of the main door in the full-scale model, is not present in the small-scale model. Wheel hubs, which should be open, do not allow air to pass through. The wheel threads shown in Figures 2.1a and b were taped since Jaeger et al. [11] showed that these threads were an unrealistic noise source due to possible scaling effects. The wing cavity, where the landing gear is stored in the cruise configuration of the aircraft, is not modeled in this study.

Figure 2.2: Photograph of the full-scale Boeing 777-200 main landing gear, [1].

2.2 The Virginia Tech (VT) Stability Wind Tunnel

The landing gear was mounted in the VT Stability Wind Tunnel. Originally it was a NACA facility located at Langley Field in Virginia, designed to provide a very low turbulence-level flow for dynamic stability measurements. The wind tunnel was installed at Virginia Tech in 1958. Figure 2.3 is a schematic description of the wind tunnel. The facility is a closed-loop tunnel with an air-exchange tower open to the atmosphere. The test section is 7.3 m (24 ft.) long with a constant square cross section of 1.83 m (6 ft.). The flow passing through the test section undergoes a 9:1 area contraction. The test section is enclosed in an air-tight control room so that the pressure in the control room equates the pressure in the test section via a window located downstream the test section. The problem of air leakage into the test section flow is thus minimized. Since its installation at Virginia Tech, the wind tunnel has undergone some modifications such as the renovation of the fan and a re-insulation of the motor windings, resulting in the increase of the overall tunnel efficiency. Although the Stability Wind Tunnel was shown to have very good flow quality and was used for aeroacoustic measurement in the past, it was not primarily built as an acoustically quiet facility.

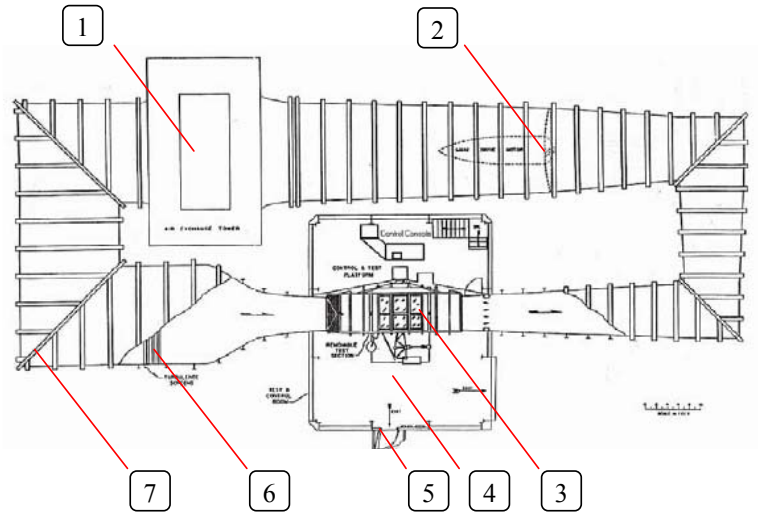

Figure 2.3: The VT Stability Wind Tunnel : (1) drive fan; (2) air exchange tower; (3) test section; (4) air-tight control room; (5) air lock; (6) turbulence screens; (7) corners.

In July 2006, as a part of a project to render the Stability Wind Tunnel suitable for aeroacoustic measurements, the hard-walled test section was removed and replaced by an anechoic one. Other parts of the wind tunnel were quieted such as the drive fan [34]. Figure 2.4 is a CAD drawing depicting a three-dimensional view and a cross-sectional view of the test section. The test section is supported with 6 by 6 inches steel beams (1). The bottom and the top of the test section are fitted with acoustic wedges (6). Stretched Kevlar® membranes glued on perforated metal sheets (4) separate the flow area from these acoustic wedges.

Two anechoic chambers (10) are mounted on both sides of the test section as shown in Figure 2.4b. The anechoic chamber has an inner height of 102 inches, an inner width of 97.5 inches, and an inner length of 162.75 inches. Stretched Kevlar cloth forms the side walls of the test section. Kevlar is hold in tension by aluminum frames (2) that are bolted to the structural beams (1) with L-brackets (3). Steel panels (7) seal the ends of the test section.

Stretched Kevlar membranes were first utilized in aeroacoustic measurement by Jaeger et al. [35] as an answer to flow induced noise. Relevant properties of Kevlar for aeroacoustic measurement were shown to be:

i. very high strength and durability that makes it tolerate flow-induced fatigue very well,
ii. when stretched, it appears as a hard surface to the flow, and
iii. very low acoustic impedance up to high frequencies.

Depending on the type of fabrics utilized, the acoustic attenuation may vary. In this application, 120 style, 7.9 grams/cm^2 (1.7 oz/in^2), plain weave Kevlar was chosen [36]. Jaeger et al. [35] found that the insertion loss varied from nearly 0 at low frequencies to about 2 dB at 25 kHz.

Theoretically, the new wind tunnel configuration is open from an acoustic point of view and closed from a fluid point of view. Therefore, noise measurements could be performed through the Kevlar membrane to the anechoic chamber. However, the experimental setup exhibited some limitations. It was observed that the Kevlar membrane does not exactly appear as a hard surface to the flow but let air go through in a relatively small amount. The same problem was observed with the material used to seal the gap between the structural beams of the test section and the ones of the anechoic chamber. Last, Kevlar is not completely transparent from an acoustic point of view and its impedance needs to be considered when post-processing the acoustic data.

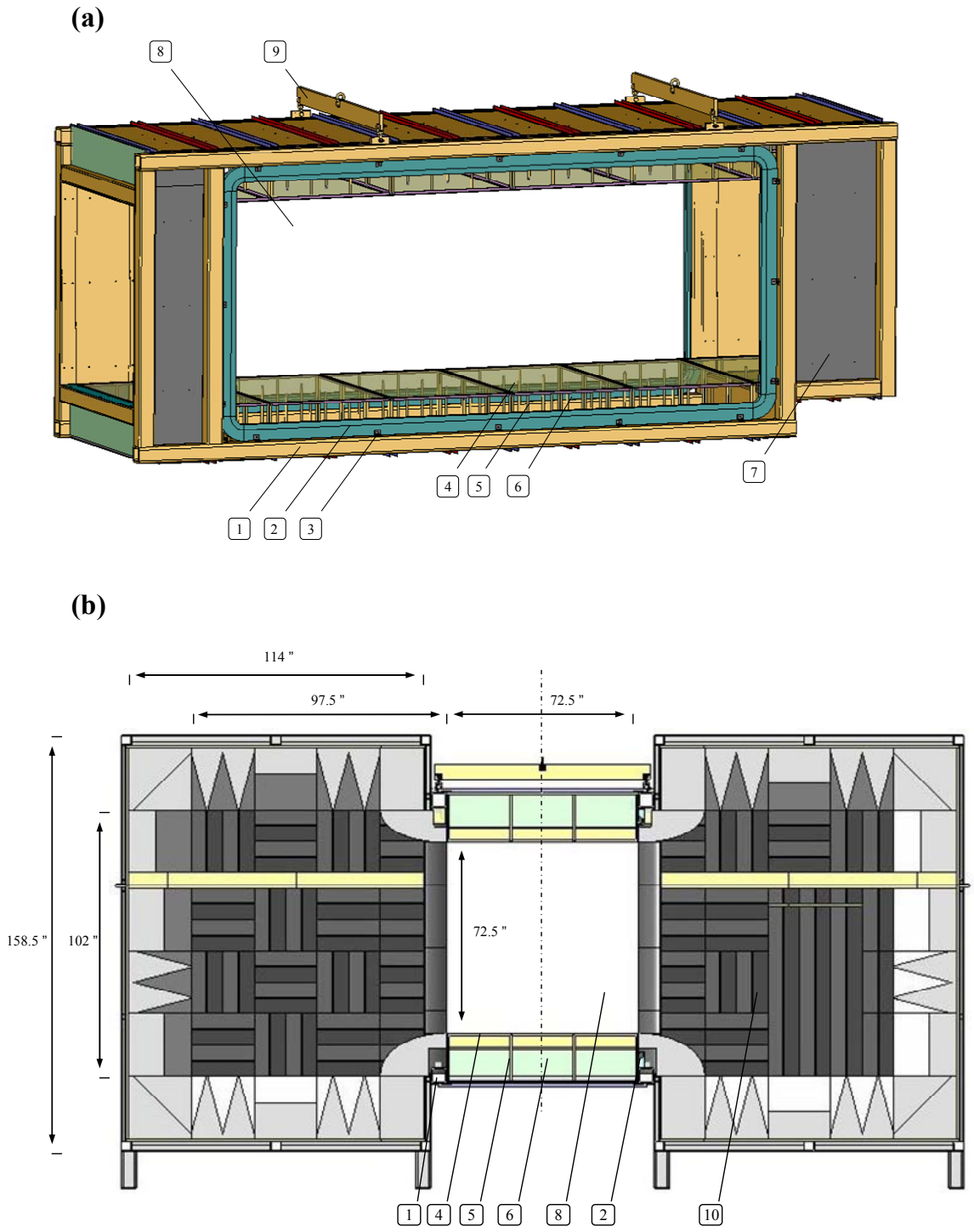

Figure 2.4: (a) Perspective view and (b) cross-sectional view of the test section: (1) structural beams of the test section; (2) aluminum Kevlar tensioning frame; (3) L-brackets connecting the Kevlar tensioning frame to the structural beams of the test section; (4) Kevlar membranes glued on perforated metal sheets; (5) supports for the perforated metal sheets; (6) emplacement for acoustic wedges; (7) steel panels (thickness: 1/8 inch) sealing the test section; (8) flow area; (9) hoist beams, (10) anechoic chambers.

For the purpose of our experiments, one anechoic chamber was removed and the corresponding Kevlar wall was replaced by a hard wall. The hard wall consisted of aluminum honeycomb core sandwiched between 2 aluminum sheets. A frame made of 3 by 1.75 inches oak beams supported the panels and was connected to the test section via the L-brackets the Kevlar tensioning frame was bolted to. Therefore, experiments were conducted in a semi-anechoic environment. Figure 2.5 is a photograph of the semi-anechoic test section. An opening with dimensions 44 by 45 inches was located at the center of the hard wall to allow the model to be supported from outside the flow area. During the various experiments, this opening was sealed.

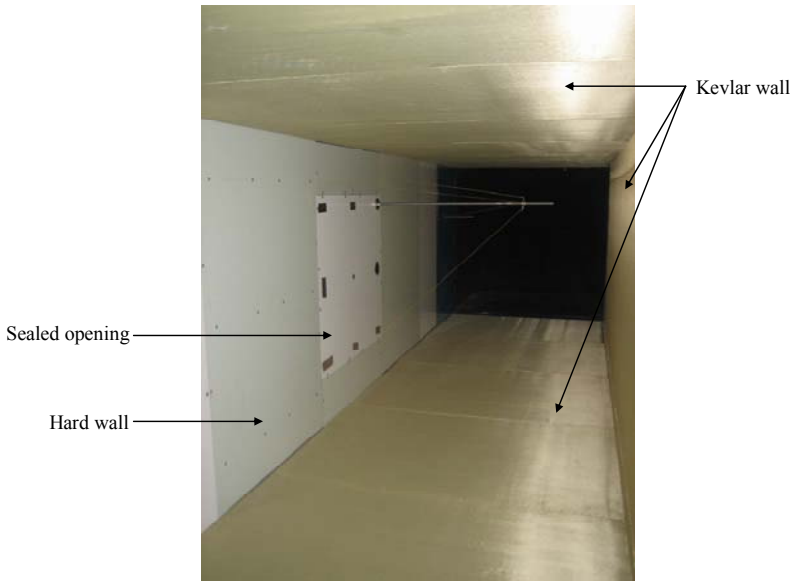

Figure 2.5: A photograph of the semi-anechoic test section.

Figure 2.6 illustrates the setup of the landing gear. In Figures 2.6a and b, the model is observed from outside and inside the test section, respectively. The model was mounted sideway in the test section. A structure made of steel (2), whose bottom was bolted to a turn table (5) and whose top was bolted to the top structural beam of the test section, supported the model (3). The opening in the wall was sealed with a transparent Plexiglas plate (4) so that the experiments could be observed from outside the test section.

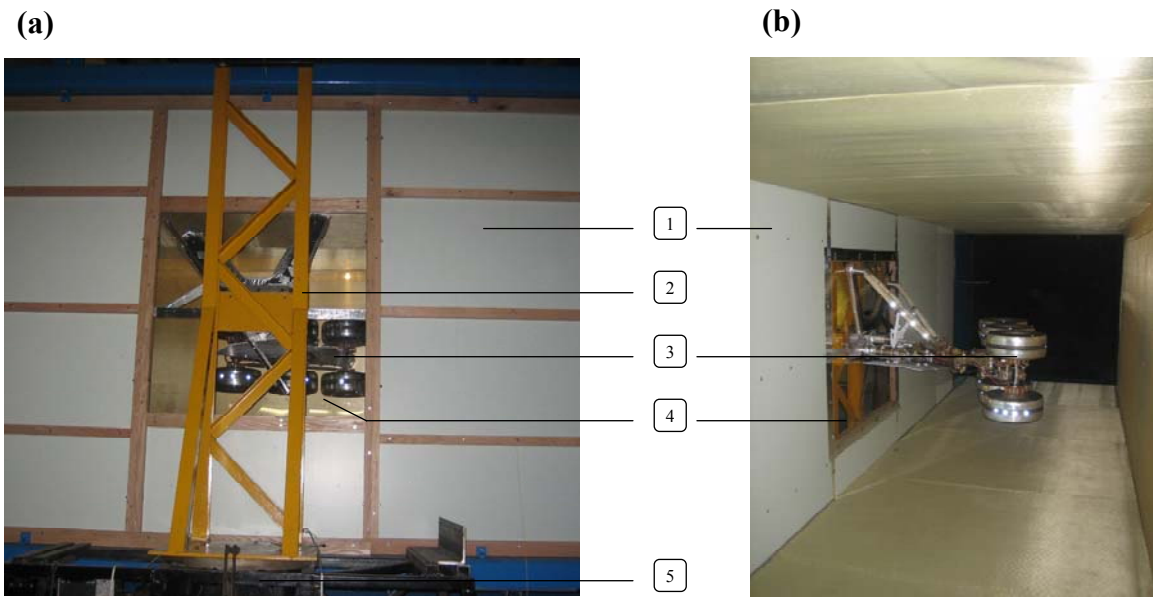

Figure 2.6: Photographs of the landing gear mounted in the semi-anechoic test section, (a) viewed from outside, and (b) view from inside the test section: (1) test-section hard wall; (2) supporting structure for the landing gear; (3) model-scale landing gear; (4) Plexiglas window; (5) turn table.

2.3 Instrumentation

Two instrumentation systems were used for the acoustic measurements of the landing gear. A 63-element microphone phased array was primarily used to locate noise sources of the model. A linear array of 15 microphones was also used to determine the directivity pattern. Flow measurements were carried out in the test section during the experiments to estimate the Mach number.

2.3.1 Microphone phased array system

The acoustic data acquisition was primarily carried out with the 63-element microphone phased array depicted in Figure 2.7a. This array was designed for VT by J. Underbrink and R. Stoker from the Boeing Co. The microphones of the phased array (Panasonic WM-60AY Electret microphones) were patterned in a multi-arm spiral manner as depicted in Figure 2.7b. The microphones were found to be reliable only up to about 20 kHz, i.e. the microphone signal rolled off steeply at 20 kHz. An aluminum plate was used to position the microphones accurately. Tapped holes in the plate, at the microphone locations, allowed the custom-made microphone adaptors to be bolted in the plate so that the microphones were mounted flush with the plate surface. The 63

microphones signals were sampled simultaneously at 51200 samples per second in 25 separate blocks of 16384 samples each.

Time domain data was processed using a frequency-domain, phased array beamforming developed at Virginia Tech using Intel Fortran Compiler 7 and Intel Math Kernel Library 6 [37]. This beamforming differs from the conventional one used in Ravetta's study [37] because it accounts for flow effects. The beamforming algorithm used in the herein study is presented in detail in Appendix A.

Data was processed from 2 to 25 kHz in $1/12^{th}$ octave bands. The spatial resolution of array is given in term of the beamwidth (BW), i.e. the region of the beamforming map within 3 dB of the peak level. It was shown that the beamwidth of this array for a plane at 36 inches is $BW_{36} = 2.45\ \lambda$ [37], where λ is the sound wavelength. The signal to noise ratio was found to be about 10 dB at high frequencies [37]. Figure 2.8 depicts the array response for the frequencies f = 5, 10, and 25 kHz [37]. Data visualization was helped by the software Tecplot®.

(a) **(b)**

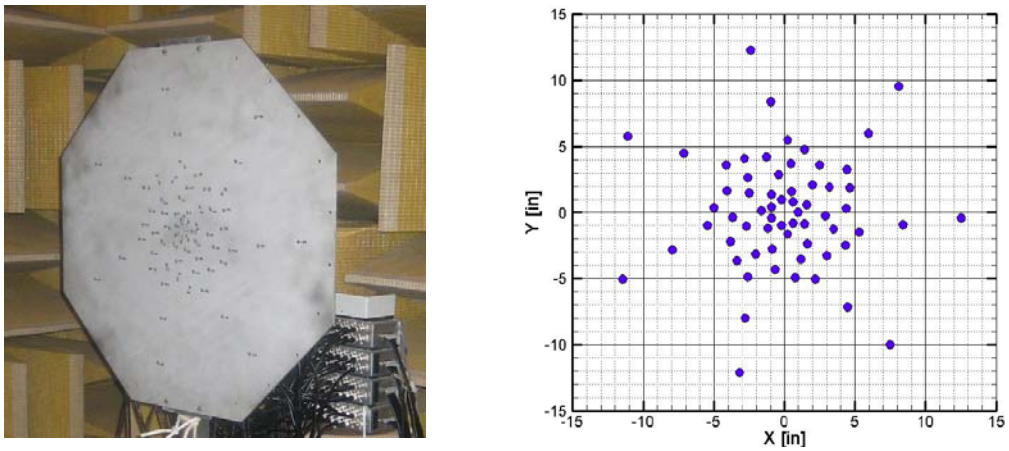

Figure 2.7: (a) A photograph of the 63-element microphone phased array. (b) The microphone pattern of the array [37].

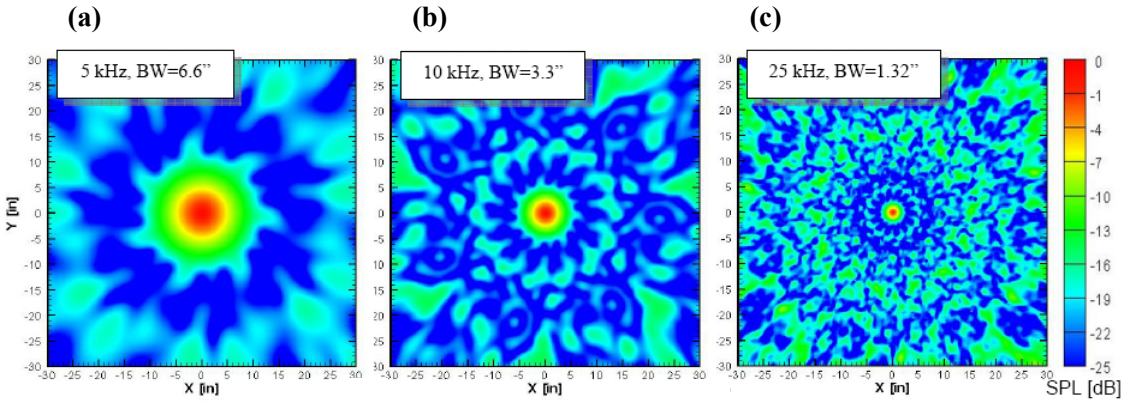

Figure 2.8: 63-element phased array response for a) 5, b) 10 and c) 25 kHz in a plane 36 inches from the array [37].

a. Phase calibration of the microphone phased array

Following Mosher et al. [38], the microphone phased array was calibrated in an anechoic chamber to account for phase mismatch in the signals that can arise from using an inaccurate estimate of the microphone locations, phase mismatch in the electronic circuitry, and phase mismatch in the microphones.

A speaker located consecutively 37.8 and 135.4 inches from the center of the array and driven with white-noise was used to generate the calibration matrices. These matrices contained the phase delay for each microphone, when the source was close and far from the array. These factors were subsequently used to correct the data in the beamforming process. A comprehensive derivation and implementation of the calibration procedure may be found in reference 37.

b. Calibration of the array levels

Tests were conducted in the VT semi-anechoic wind tunnel to determine the sensitivity of the array as well as to account for the presence of the Kevlar wall and the dissipation effects of the boundary layer in the wind-tunnel test section. In the following, the calibration procedure is briefly described. A more comprehensive description of the procedure may be found in Appendix B.

The calibration of the array levels was based on a calibration of the beamforming output and not an individual calibration of each of the 63-microphones. A point source with known characteristics and driven with whitenoise was used to calibrate the levels of the phased array. First, the sound field of the source was accurately measured in an anechoic chamber using a single microphone positioned at various directions from the source. Subsequently, the point source was installed in the test section and the 63-element microphone phased array was used to locate the source. The beamforming maps of the point source were integrated 8 dB down the peak value. The integrated spectrum was compared to the single microphone measurements to determine the sensitivity of the array. Note that tests were conducted in the presence of the Kevlar wall at the interface of the test section and the anechoic chamber. Therefore, the presence of Kevlar is accounted for in the calculation of the array sensitivity.

The levels of the array were also corrected for flow effects. The point source was located with the phased array at various wind tunnel speeds. Correction factors for flow effects were determined by comparing the integrated spectra with and without flow.

2.3.2 Linear array of microphones

The linear array of 15 microphones shown in Figure 2.9a was used to determine the directivity pattern of the landing gear. The microphones used in this array were 1/4-inch diameter PCB TMS130. The microphones were individually calibrated with a B&K model 4231 pistonphone prior to measurement. The beams supporting the microphones were treated with acoustic foam to minimize acoustic reflections. The pattern of the linear array is depicted in Figure 2.9b. The array was designed to have its microphones spaced apart by a constant angle with respect to a reference point located on the model gear during the various wind tunnel tests.

(a)

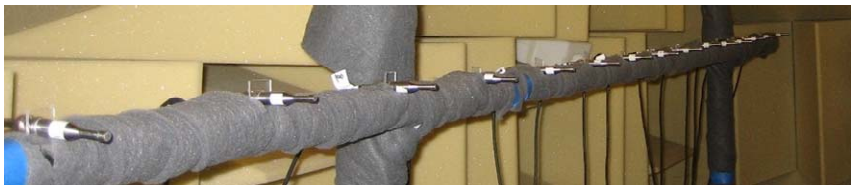

(b)

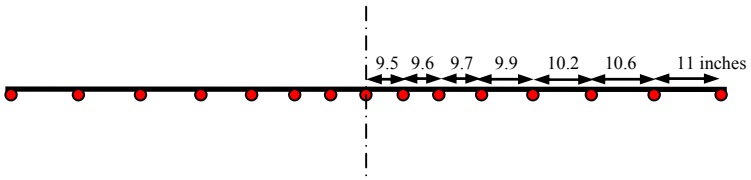

Figure 2.9: (a) A photograph of the linear array of microphones. (b) The microphone pattern of the array.

2.3.3 Flow measurements

During the various experiments, flow measurements were carried out in the test section to estimate the Mach number. The quantities measured were the temperature and the dynamic pressure also known as tunnel Q, using, respectively, a thermometer and a pitot-probe installed upstream the test section. The fan RPM was also recorded for each test. The flow speed was computed from Bernoulli equation,

$$p + \frac{1}{2}\rho V^2 + \rho g h = \text{Constant}, \tag{2.1}$$

where p is the pressure, ρ is the density, V is the flow speed, h is the elevation, which is neglected, and g is the gravitational acceleration.

2.4 Testing configurations of the landing gear

The experimental setup for noise measurement of the model gear is presented in the following. The various configurations of the measurement systems and the landing gear will be described. The setup of the landing gear in the test section was presented in Section 2.2.

2.4.1 Test setup for phased array measurement of the landing gear

The 63-element phased array was placed in the anechoic chamber at three locations labeled from 1 to 3 in Figure 2.10. The array was positioned in such a way as to take acoustic data on the flyover path of the model, i.e. at the mid-height of the anechoic chamber. To help locate the landing gear with respect to the array, a laser pointer was installed at the center of the array. The laser beam was pointing toward the lower truck of the landing gear, as shown in Figure 2.11. The position of the laser beam on the lower truck served as a reference point to place the landing gear model in the beamforming maps.

The array position labeled 1 corresponds to the same position used by Ravetta et al [12]. The array was positioned 2.75 inches behind the Kevlar wall. The gap between the array and the Kevlar membrane was to provide significant attenuation of flow-induced noise caused by the unsteadiness of the boundary layer, as demonstrated by Jaeger et al [35]. Comparing results between position 1 in this test entry and the flyover position in Ravetta et al.'s work allows investigation of the effects of the acoustic environment on phased array measurement, i.e. hard wall versus semi-anechoic wind tunnel. The relevance of the comparison is emphasized by the fact that both experiments took place in the same facility using the same landing gear model. However, some discrepancies between the two experiments should be pointed out. Ravetta et al's array was recessed 1.25 inches behind a Kevlar membrane significantly smaller than the one used in this study. The deflection of the Kevlar wall observed during the tests forced us to recess the array deeper, i.e. 2.75 inches.

The array in position labeled 2 was located in the far-field, 82.5 inches from the Kevlar wall. This distance was limited by the dimensions of the anechoic chamber and the need for the array to be at least half a wavelength away from the wedges, for the range of frequencies considered, i.e. 2 to 20 kHz. The distance d between the array and the model was sufficiently large for the array to be in the acoustic far field ($d > 10\lambda$) and nearly in the geometric far field (d was about 3 times the largest dimension of the landing gear). Phased array measurements carried out from this position were compared to the

near field data (position 1). Therefore, the validity of collecting acoustic data in the near-field with a microphone phased array could be evaluated.

Additional far field measurements were carried out with the array in position 3. In this position, the center of the array was located 82.5 inches from the Kevlar wall. Data from these measurements was used to determine other possible noise sources of the landing gear on the flyover path. To avoid distortion effects, the phased array was oriented such that the normal to its surface was pointing toward the center of the hard wall.

In addition to the baseline model, various streamlining devices were tested. Past experiments in the VT hard-walled Stability Wind Tunnel allowed the noise reduction potential of these devices to be evaluated. Since the opportunity was given to conduct tests with the same landing gear model, in the same facility but in an anechoic environment and in the far-field, the noise reduction potential of the streamlining devices was evaluated again. Three fairings were developed at Virginia Tech by Ravetta [37] to streamline the landing gear components identified as major noise sources. The devices were made of a double-layer of elastic "lycra-like" cloth and were held in place with Velcro. The material used was light, stretchable, strong, and did not interfere with the steering mechanism of the landing gear. The devices streamlined the truck, the braces and the strut, and achieved significant noise reduction as shown by Ravetta [37] from measurements in a hard-wall tunnel configuration and in the near-field. A more comprehensive description of the fairings design may be found in reference 37. A rigid fairing streamlining the lower truck and referred to as toboggan was also tested. This model-scale device was originally designed by NASA, the Boeing Co., and Goodrich, for mitigation purposes in the QTD2 Program. Figures 2.12a through c are photographs of the VT lower truck fairing, the VT braces, strut and lower truck fairings, and the NASA toboggan, as mounted on the landing gear, respectively.

The various configurations of the experimental setup are listed in Table 2.1. Four configurations of the landing gear were tested: Baseline, VT lower truck faring, all VT

fairings, and NASA toboggan configurations. Each configuration was tested at 3 wind tunnel speeds, M = 0.12, 0.15, and 0.17, and for the 3 phased array positions. The fan RPM, tunnel Q, atmospheric pressure, and tunnel temperature, which were utilized to calculate the Mach number in the test section, are also listed in the table.

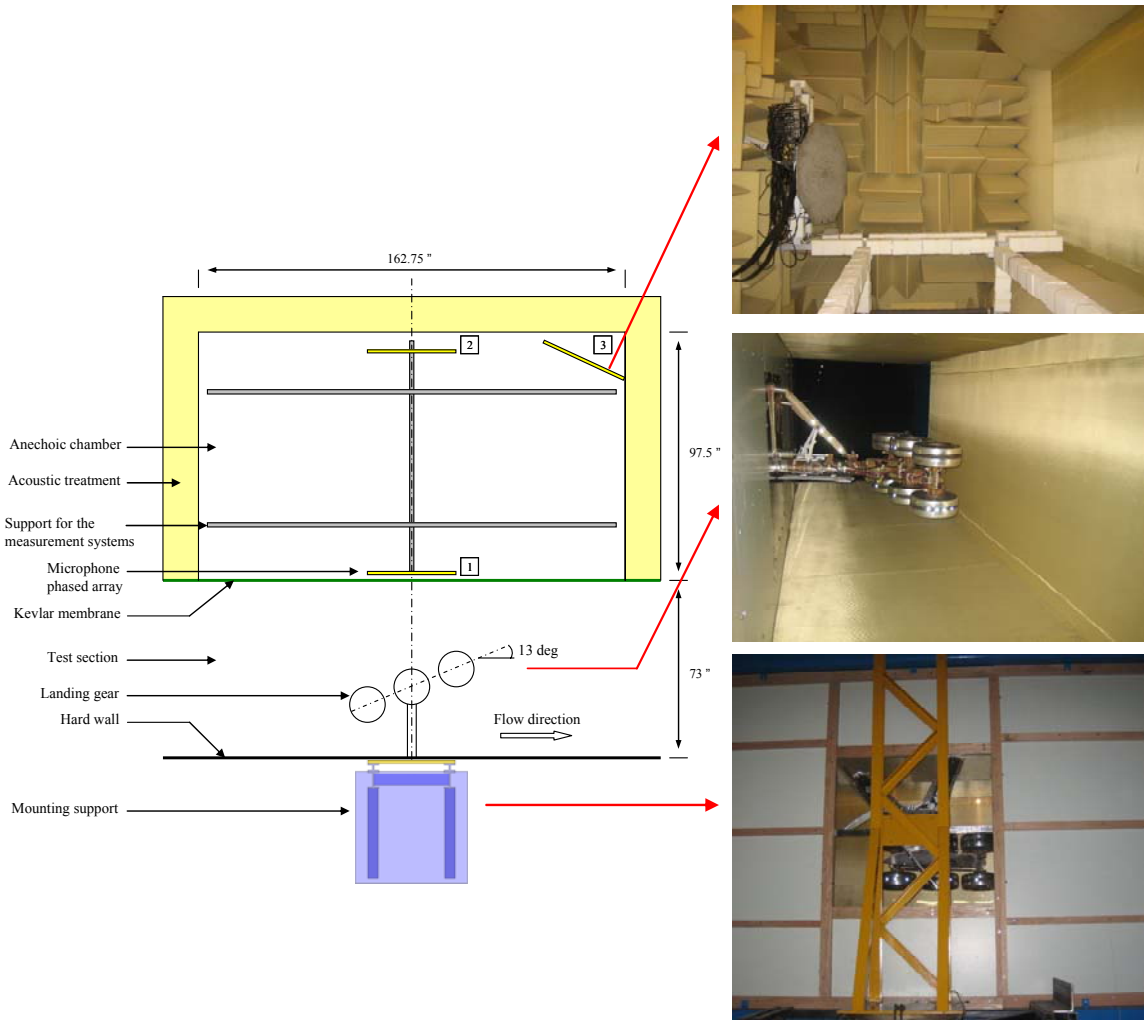

Figure 2.10: The phased array measurement setup.

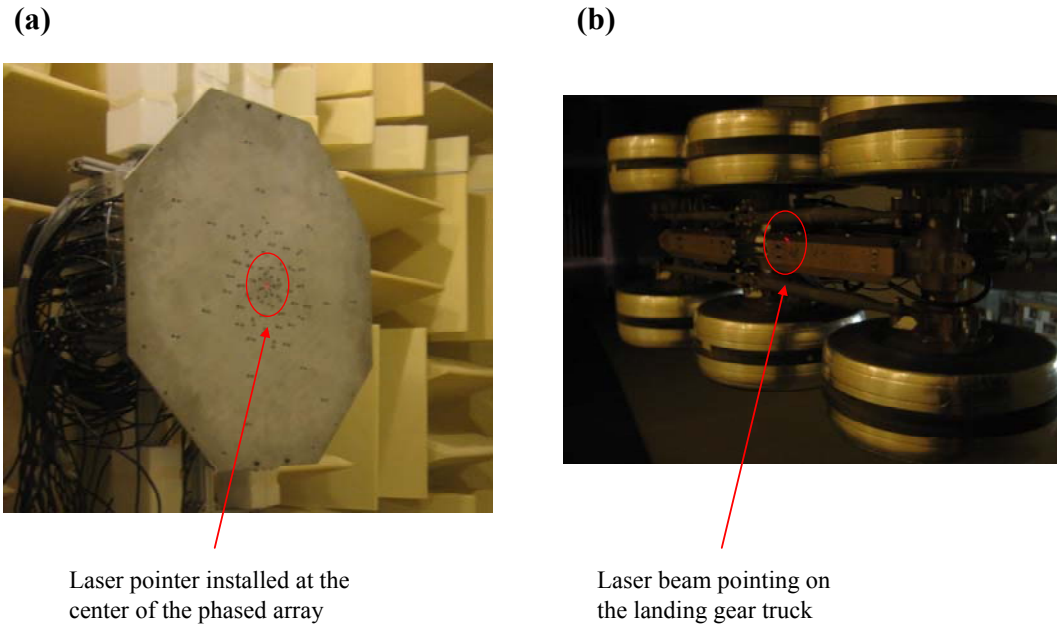

Figure 2.11: (a) Laser pointer installed at the center of the phased array. (b) Laser beam pointing on the lower truck of the landing gear.

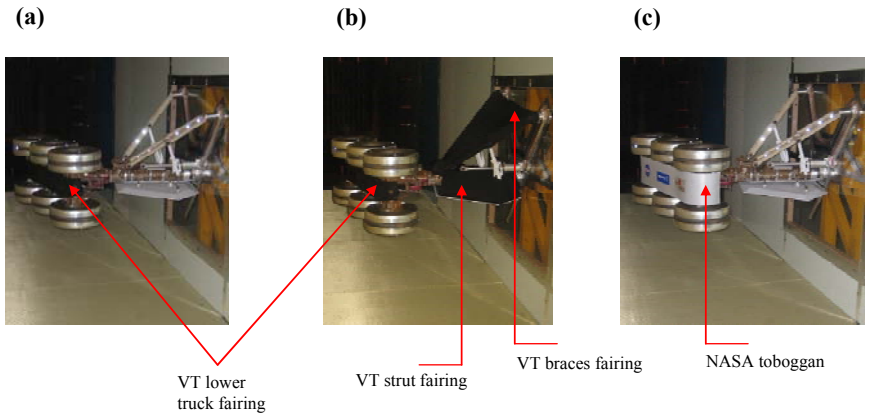

Figure 2.12: Photographs of the streamlining devices as mounted on the landing gear: (a) the VT lower truck fairing, (b) all VT fairings, (c) the NASA toboggan.

Table 2.1: The various configurations of the experimental setup for phased-array measurement of the landing gear noise.

LG Configuration	Array Position	Fan RPM	Tunnel Q (in WC)	Atm Pressure	Tunnel Temp (F)	Flow Speed (m/s)	Mach Number
Baseline	1	394	3.55	27.75	89.4	40.59	0.118
Baseline	1	489	5.5	27.62	90.4	50.69	0.148
Baseline	1	549	7	27.51	91.8	57.37	0.167
VT lower truck fairing	1	386	3.55	27.67	96	40.89	0.119
VT lower truck fairing	1	477	5.5	27.54	96.9	51.06	0.149
VT lower truck fairing	1	538	7	27.43	98.1	57.78	0.168
All VT fairings	1	392	3.55	27.67	94.3	40.83	0.119
All VT fairings	1	487	5.5	27.53	95.5	51.01	0.149
All VT fairings	1	548	7	27.43	97	57.73	0.168
NASA toboggan	1	393	3.55	27.74	95.6	40.83	0.119
NASA toboggan	1	486	5.5	27.61	96.3	50.97	0.149
Baseline	2	382	3.55	27.7	90.3	40.66	0.119
Baseline	2	474	5.5	27.56	91.4	50.79	0.148
Baseline	2	535	7	27.45	92.7	57.48	0.168
VT lower truck fairing	2	383	3.55	27.7	92	40.72	0.119
VT lower truck fairing	2	475	5.5	27.56	93.7	50.90	0.148
VT lower truck fairing	2	535	7	27.46	95.3	57.61	0.168
All VT fairings	2	391	3.55	27.7	100	41.02	0.120
All VT fairings	2	487	5.5	27.56	100	51.18	0.149
All VT fairings	2	550	7	27.46	100.6	57.88	0.169
NASA toboggan	2	377	3.55	27.7	87.9	40.57	0.118
NASA toboggan	2	466	5.5	27.56	89.7	50.71	0.148
NASA toboggan	2	527	7	27.46	91.6	57.41	0.167
Baseline	3	399	3.55	27.58	107.4	41.44	0.121
Baseline	3	492	5.5	27.45	108.6	51.77	0.151
Baseline	3	555	7	27	110	52.87	0.154
VT lower truck fairing	3	390	3.55	27.59	97.5	41.01	0.120
VT lower truck fairing	3	482	5.5	27.46	98.3	51.20	0.149
VT lower truck fairing	3	541	7	27.35	99.6	57.94	0.169
All VT fairings	3	410	3.55	27.59	98.2	41.03	0.120
All VT fairings	3	502	5.5	27.45	99.1	51.25	0.149
All VT fairings	3	555	7	27.34	100	57.98	0.169
NASA toboggan	3	381	3.55	27.6	91.6	40.78	0.119
NASA toboggan	3	472	5.5	27.47	92.4	50.92	0.148
NASA toboggan	3	530	7	27.37	94.1	57.64	0.168

2.4.2 Test setup for linear array measurement of the landing gear

Figure 2.13 illustrates the experimental setup for acoustic measurement of the landing gear noise using the linear array of 15 microphones described in Section 2.3.2. The linear array was used to determine the radiation pattern of the model. The array was positioned 10 inches from the back of the anechoic chamber. Microphones were spaced 4.3° apart with respect to a reference point located on the landing gear's lower truck.

Like for the phased array measurements, the same 4 landing gear configurations were planned to be tested with the linear array. These configurations were described in detail

in Section 2.4.1. However, due to time limitation, only part of tests could be completed. The configurations tested and relevant flow data are listed in Table 2.2.

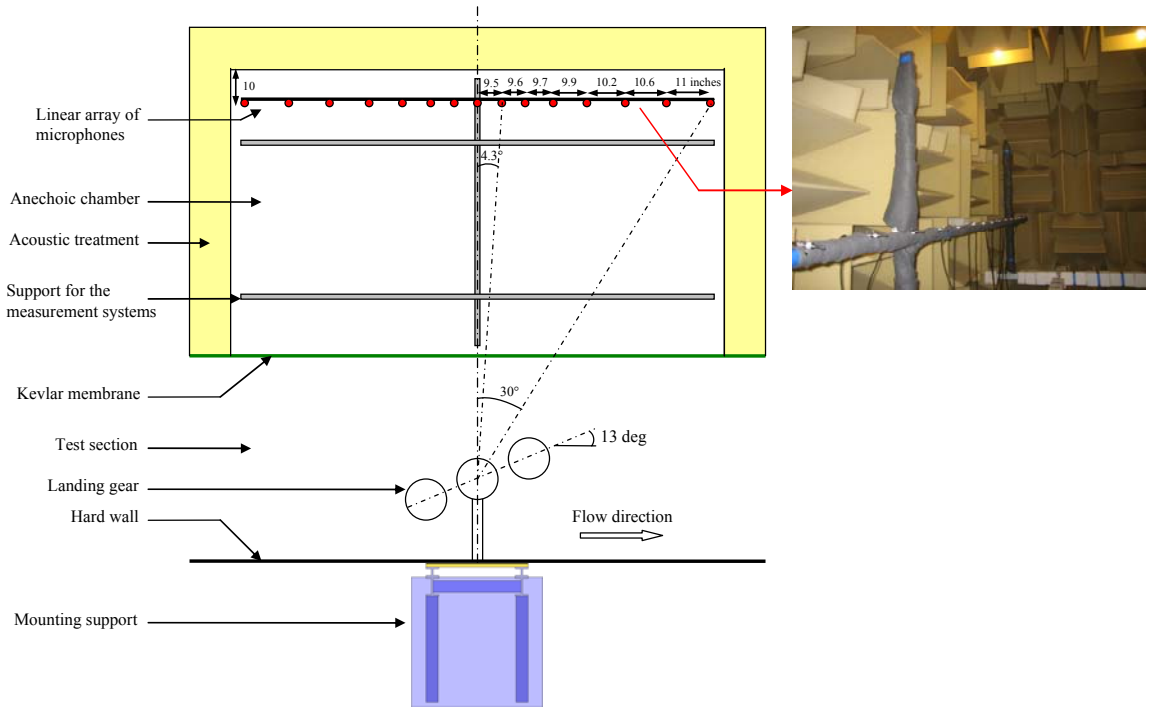

Figure 2.13: The linear array measurement setup.

Table 2.2: Configurations of the experimental setup for linear-array measurement of the landing gear noise.

LG Configuration	Fan RPM	Tunnel Q (in WC)	Atm Pressure	Tunnel Temp (F)	Flow Speed (m/s)	Mach Number
Baseline	391	3.55	27.6	89.7	40.6	0.118
Baseline	484	5.5	27.65	90.4	50.7	0.148
NASA toboggan	393	3.55	27.74	95.6	40.8	0.119
NASA toboggan	486	5.5	27.61	96.3	51.0	0.149

3 EXPERIMENTAL RESULTS

In this chapter, results from the landing gear tests are presented. Though 3 speeds were tested for each configuration of the landing gear, only the case for M = 0.17 is presented. Data from the 63-element microphone phased array and from the linear array of 15 microphones was used to locate noise sources in the landing gear and to determine the radiation pattern of gear, respectively. Phased array data was primarily post-processed with a revised beamforming code that accounts for flow effects. More details about the modifications of the conventional beamforming algorithm are found in Appendix A.2. For comparison purposes, some acoustic data was also processed with conventional beamforming. All the frequencies discussed in this section have been scaled to full-scale frequencies by the following relation:

$$f_{full-scale} = scale\ factor * f_{measured}, \tag{3.1}$$

where the scale factor is 0.26.

In Section 2.3.1 the calibration procedure for the array levels was briefly explained. Although absolute levels of the landing gear noise were obtained, in this thesis, only relative levels are presented from 0 to -15 dB. At the beginning of each subsection 3.1, 3.2, and 3.3, the reference 0 dB will be defined.

To better aid in the visualization of the key components of the gear noise, cross-sectional plots of the 3-dimensional beamforming maps originally generated are presented. The locations of the cross-sections are depicted in Figure 3.1 as red lines. The cross-sections located at the bottom and at the top are the most representative of the noise generated by the truck, and by the strut, door, and braces, respectively. For the sake of clarity, these planes are referred as “truck” and “strut” planes in the rest of the document. In the figure, the lower truck is at an angle of attack of 0° whereas it was at 13° during the tests. Despite what the drawing suggests, the “truck” plane does not pass through the rear and front brakes. Therefore, on the truck plane, noise levels of the front and rear brakes are slightly off the actual levels. However, it should not alter the content of the discussion since in this chapter, the beamforming maps are presented for qualitative analysis mainly.

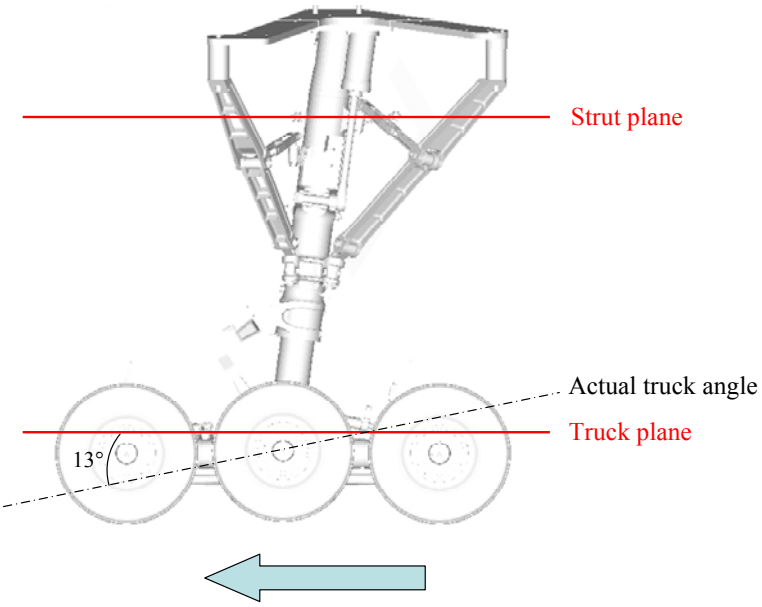

Figure 3.1: Locations of the cross-sectional plots presented.

First, the effect of the acoustic environment on phased array measurement is discussed. Data collected in the semi-anechoic wind tunnel, in the near-field of the baseline model, is compared to the data collected in hard-walled-wind-tunnel. Data was processed with both a conventional and a revised beamforming code, which allowed for comparison between the two post -processing algorithms. Subsequently, the relevance of taking phased array measurements in the far-field is underlined by comparing the data collected in the near-field and far-field of the baseline model, in the semi-anechoic wind-tunnel test section. Ultimately, the effectiveness of various passive noise control devices will be compared.

3.1 Effects of the acoustic environment on phased array measurement and limitations of conventional beamforming in a moving medium

In this section the effects of the acoustic environment on phased array measurement are discussed. Then, conventional beamforming and beamforming accounting for flow are compared. The discussion is based on beamforming maps of the landing gear noise on the "truck" plane. For each frequency, the reference 0 dB corresponds to the peak

value of the beamforming map of the landing gear noise obtained in hard-walled test section.

Figure 3.2 depicts the beamforming maps of the landing gear noise with the array in the near-field (array position 1 in Figure 2.10), in the hard-walled test section (left maps) and in the semi-anechoic test section (right maps). Results for four frequencies are shown in this figure, i.e. full scale frequencies of 1128, 1898, 3381, and 4781 Hz. Hard-walled data was collected by Ravetta [37]. A beamforming code with diagonal removal and accounting for flow was used to process the data. As explained in Appendix A, a new Green's function, exact solution of the convected wave equation, was implemented in the beamforming code.

The figure indicates that, in term of noise-source identification, the beamforming maps from the tests conducted in hard-walled and semi-anechoic test sections are in good agreement. Indeed, both tests show that on the flyover view, in the near-field of the model, the front and rear brakes (lower truck components) are the major noise sources of the landing gear. The figure also indicates that a reduction of the background noise leads to significantly cleaner beamforming maps. In the hard-walled test section, at f = 3381 and 4782 Hz, noise from the front brakes is not clearly identified. However, it is obvious in the semi-anechoic test section. Reducing the background noise levels leads to a significant attenuation of the sidelobes levels and reflections, and thus, a better identification of actual noise sources. Furthermore, the reduction of the sidelobes levels is important in the estimation of the noise levels generated by the model. Indeed, when beamforming maps are integrated to estimate the sound pressure level (SPL) of the sources, so are the sidelobes, which are not representative of the actual noise generated.

In term of levels, the beamforming maps indicate that the peak values of the main lobes are higher in hard-walled test section than in semi-anechoic one. Tests were conducted in the same facility, at the same speeds, and using the same model. Noise levels of the landing gear were expected to be about the same in both the anechoic and hard-walled test sections, regardless of the background noise levels. The difference in

levels is quantified by the integrated spectrum presented and discussed at the end of this section in Figures 3.4 and 3.5.

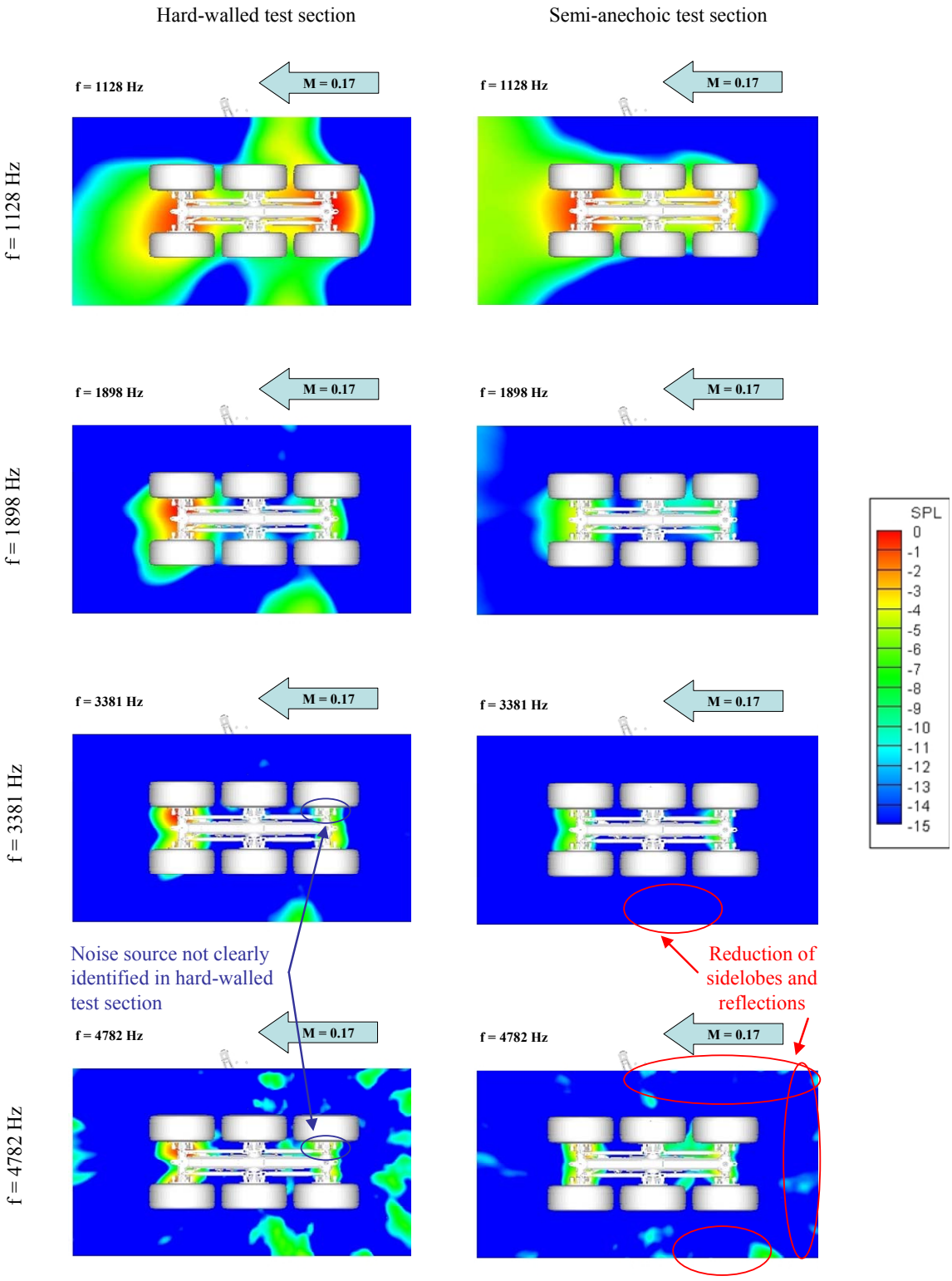

Figure 3.2: Beamforming maps of the baseline landing gear at full scale frequencies, f = 1128, 1898, 3381, and 4782 Hz, as obtained with the phased array in the near-field of the model (position 1). Data was post-processed using a beamforming code that accounts for flow and using diagonal removal. Reference 0 dB for each frequency: peak value of beamforming maps in hard-walled test section (left maps).

Figure 3.3 depicts the same results as in Figure 3.2 but using the conventional beamforming code used in previous experiments by Ravetta [37]. The maps obtained with conventional beamforming are solely presented for comparison purpose with the revised beamforming code. To account for the convective effect of flow on source location, the beamforming maps presented in Figure 3.3 were shifted by a constant distance determined analytically as explained in Appendix A. The shift is the distance between the actual noise source and the apparent noise source as located with conventional beamforming. The shift was computed for a point located 36.75 inches from the center of the array on the "truck" plane in the direction of the outward normal to the array surface. This shift was found to be 6.3 inches for a flow speed of 0.17 Mach. It is shown in Appendix A.2.1 (see Figure A.3) that the farther from the point where the shift is computed, the larger the error in source location. In other words, the shift should be computed for each point of the scanning grid. Note that Ravetta et al. [12] used the same shift correction technique but determined it experimentally. It is shown in Appendix B that theory and experiments match very well and the shift may be determined either way.

The maps presented in Figures 3.2 and 3.3 differ in several ways. First, the main lobes of the maps in Figure 3.3 appear stretched as compared to the ones in Figure 3.2. This is consistent with the analysis presented in Appendix A.2.1. The distance by which the maps were shifted was computed at a point located near the center of the truck. This shift is proportional to the distance the acoustic wave has to travel in the flow region before it can reach the center of the array. However, the maps are translated or shifted by a constant distance. This approach results in stretching the main lobes that are away from the center of the map, where the shift was computed. The same reasoning explains why noise generated by the rear and front brakes are not located accurately. Note that the error in noise source location should be smaller upstream than downstream as shown in Figure A.3. For this reason, in Figure 3.3, noise generated by the front brakes is located with more accuracy than noise generated by the rear brakes. Another observation concerns the levels of the beamforming maps. The peak values of the maps depicted in

Figure 3.3 are about 1 dB lower than in Figure 3.2. If a conventional beamforming code is used to locate a point source in airflow, the travel time of an acoustic wave is misestimated. As result, the noise levels of the source are misestimated too. In the revised beamforming code, the Green's function used for the steering vector is an exact solution of the convected wave equation. In this case, the travel time of the noise source is computed exactly.

Thus, the results presented here indicate that the beamforming algorithm that accounts for flow is preferred for reliable noise source identification of a model located in airflow, in particular if the array is positioned in the near-field. Henceforth, only results using the beamforming code accounting for flow will be presented in the remaining of the thesis.

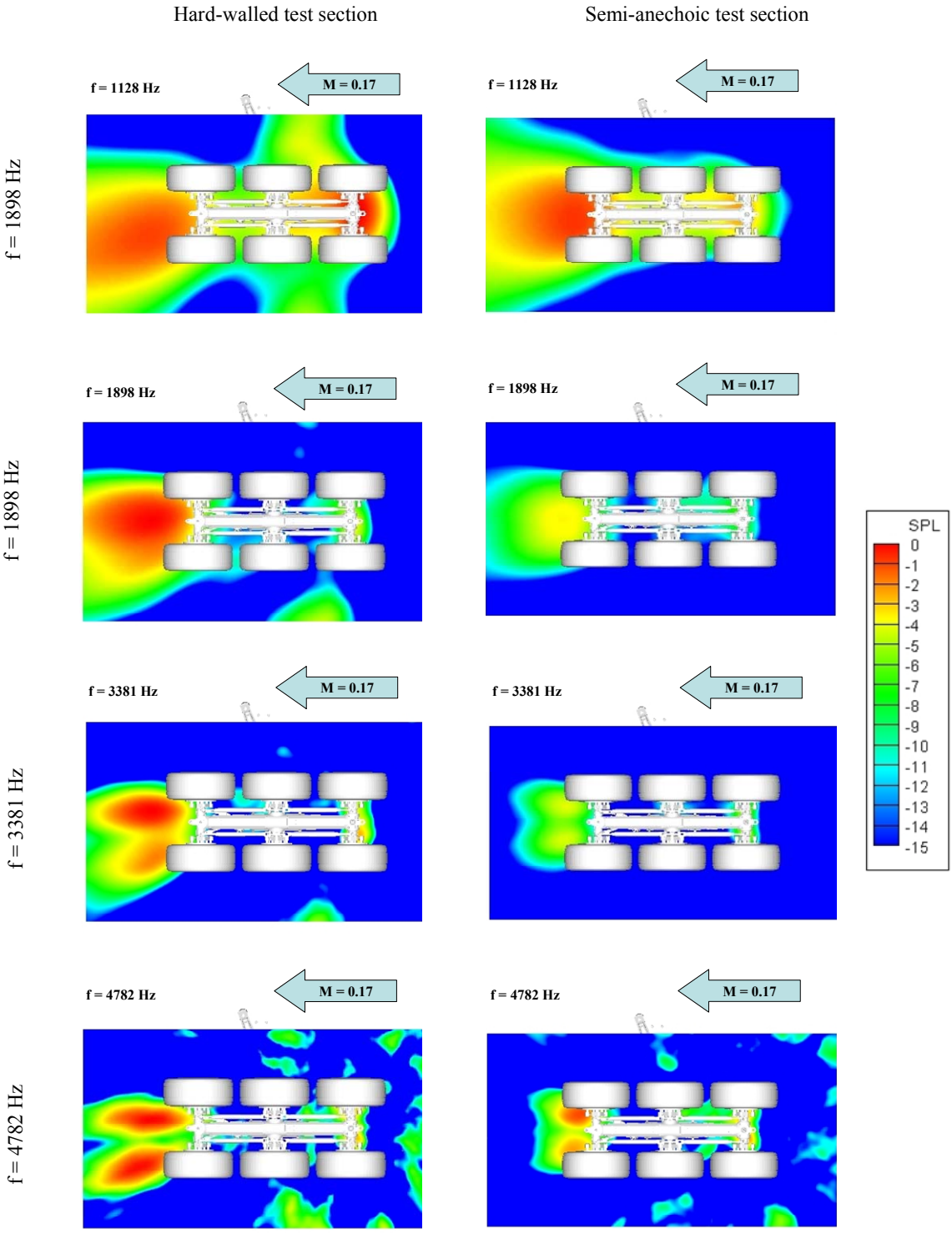

Figure 3.3: Beamforming maps of the baseline landing gear at full scale frequencies of 1128, 1898, 3381, and 4782 Hz, as obtained with the phased array in the near-field of the model (position 1). Data was post-processed with a conventional beamforming code and using diagonal removal. Reference 0 dB for each frequency: peak value of beamforming map in hard-walled test section (left maps)

As explained in reference 37, a way to quantify results from phased array measurements is to look at the integrated spectra. Integrated spectra are obtained by integrating the beamforming maps. Using the point spread function, the levels in the scanning grid encompassing a region of interest are summed to a single value for each frequency. In this study, the levels were integrated 8 dB down from the peak value to avoid adding levels related to the sidelobes. The scanning grid was the same for every configuration presented and encompassed the entire landing gear. The grid contains 323031 points and has the dimensions 70 x 56 x 39 inches.

Figure 3.4 depicts the integrated spectra of the baseline landing gear noise as obtained in hard-walled (blue curve) and semi-anechoic (red curve) wind tunnels. The calculation of the integrated spectra was based on the maps obtained with beamforming accounting for flow. The curves have similar patterns and differ from only few decibels. This result is remarkable considering the time elapsed between the two series of tests (about a year and a half) and the modifications of the facility.

For better visualization, the difference between the integrated spectra of the landing gear in hard-walled and semi-anechoic test sections is depicted in Figure 3.5. In the figure, a positive value of the curve indicates that the sound pressure level of landing gear is higher in hard-walled test section than in semi-anechoic test section. The solid red circles indicate the difference between the peak values of the beamforming maps obtained from tests conducted on the baseline landing gear in hard-walled and semi-anechoic test sections. The difference between the peak values may slightly differ from what is inferred by Figure 3.2 since here, a three-dimensional beamforming map is considered. The integrated spectrum of the landing gear in hard-walled test section is up to 5.2 dB higher than in the semi-anechoic test section. The same landing gear and phased array were used in both tests. Therefore, the difference in levels between hard-walled and semi-anechoic test sections is most likely caused by the higher background noise levels in the hard-walled test section. The figure also shows that the peak levels difference (red solid circles) matches within a decibel the integrated spectra difference (blue curve).

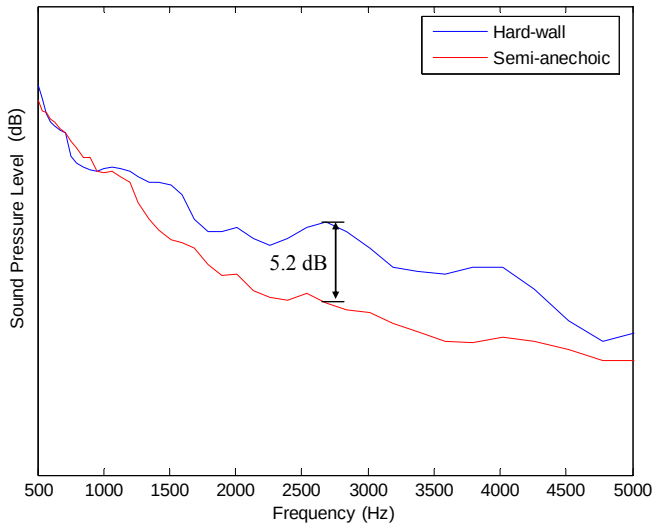

Figure 3.4: Integrated spectra of the landing gear in hard-walled (blue curve) and semi-anechoic (red curve) test sections at M = 0.17, as a function of frequency.

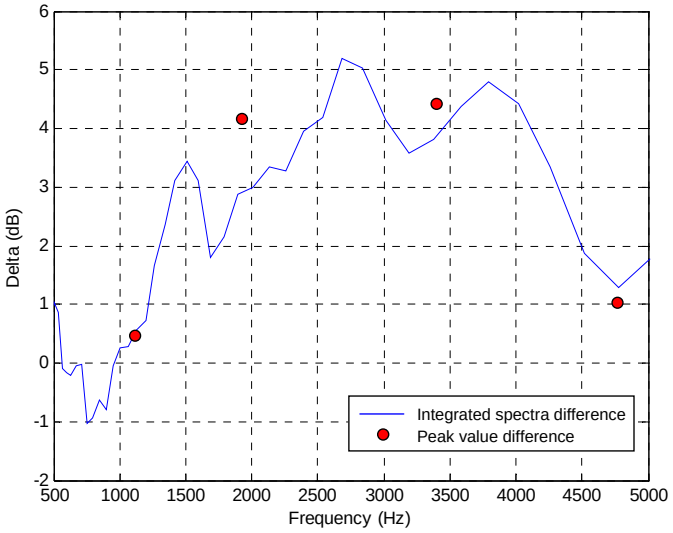

Figure 3.5: Difference between the integrated spectra of the landing gear in hard-walled and semi-anechoic test sections at M = 0.17, as a function of frequency.

3.2 Near-field effects on phased array measurement

The effects of taking aeroacoustic measurement in the near-field were investigated by a qualitative comparison between data collected with the phased array in the near-field (position 1) and far-field (positions 2 and 3) of the baseline model, in the semi-anechoic wind-tunnel test section. All phased array data presented in this section was post-processed with the beamforming algorithm that accounts for flow. For each frequency,

the reference 0 dB corresponds to the peak value of the beamforming map shown. In other words, maps obtained from array positions 1, 2, and 3 will have different 0 dB references.

Figures 3.6 and 3.7 depict the beamforming maps of the landing gear noise as obtained with the array in the anechoic chamber in positions 1 and 2. Results for the full-scale frequencies of 3381 and 4782 Hz are shown. In these figures, right and left maps correspond to the strut and truck planes, respectively. In these figures and in the rest of the section, FB-x, RB-x, S-x, D-x, UB-x, and DB-x identify the front brakes, rear brakes, strut, door, and upstream- and downstream-brace noise sources, respectively, where x is an integer between 1 and 3 corresponding to the three array positions.

First let us consider the beamforming maps obtained with the array in the near field (array position 1). This corresponds to the top maps in Figures 3.6 and 3.7. For both frequencies shown, looking at the truck and strut planes indicates that the front and rear brakes are the only noise sources identified. Similar observations were made at other frequencies not depicted here.

Then, the array was moved to the far-field, in position 2, which corresponds to the bottom maps in Figures 3.6 and 3.7. The front and rear brakes are still seen as major noise sources. However, with the array in the far-field other noise sources can be identified such as the noise radiated from the upstream and downstream braces. This result is observed from lower frequencies, shown in Appendix A of reference 40 (Figures A.1-A.4), up to 3381 Hz as shown in Figure 3.6. Noise from the upstream and downstream braces appears clearly on the maps. At 4782 Hz, noise from the upstream brace is no longer identified. For frequencies above 5000 Hz, not plotted here, the noise generated by the braces was insignificant. This result is in agreement with past studies where it was shown that from the main landing gear components, low frequency noise will be radiated whereas small elements such as wire hoses, screw holes, and so forth, will generate high frequency noise [2].

It is surmised that when the array is too close to the landing gear, the lower truck acts like an acoustic barrier and other noise sources located behind this barrier are shielded. In references 11 and 12, the microphone phased array was in the near-field of the 26%-scale landing gear. In the flyover view, straight under the truck, noise generated by the braces could not be identified. Results from past experiments [11,37] and from this study indicate that phased-array measurements of the landing gear noise on the flyover path are not reliable when they are performed in the near-field.

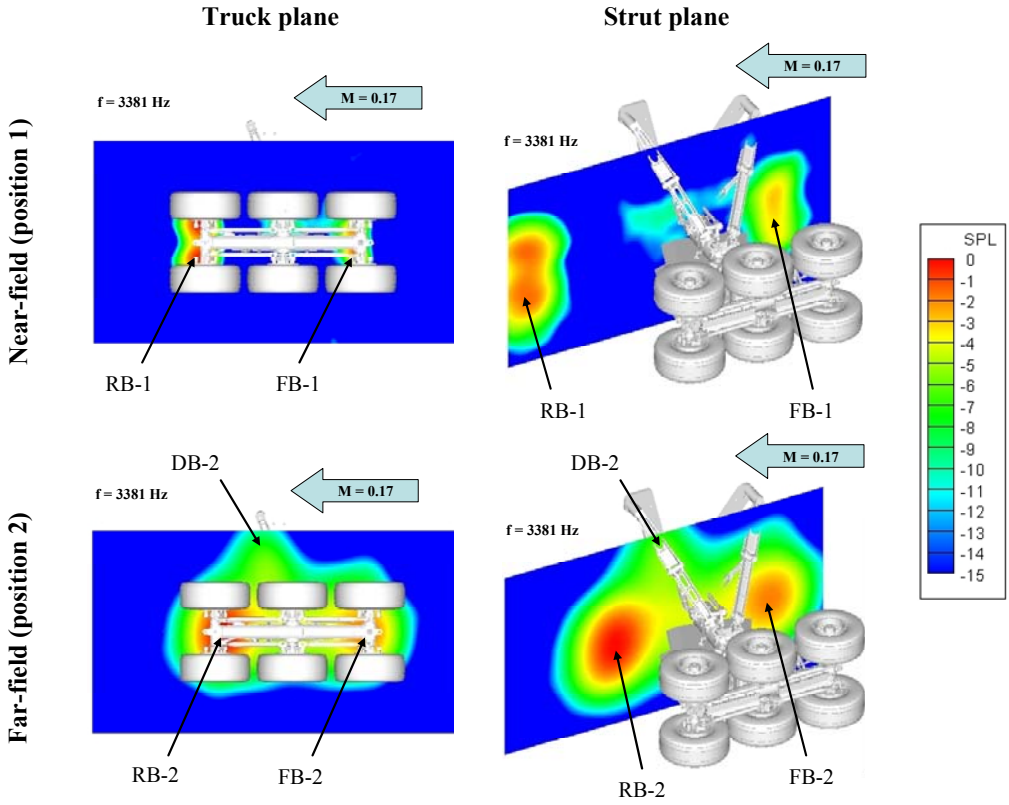

Figure 3.6: Beamforming maps of the landing gear in its baseline configuration, at full scale frequency of 3381 Hz, as obtained with the phased array in the anechoic chamber in positions 1 and 2. Reference 0 dB: peak value of beamforming map in the truck plane.

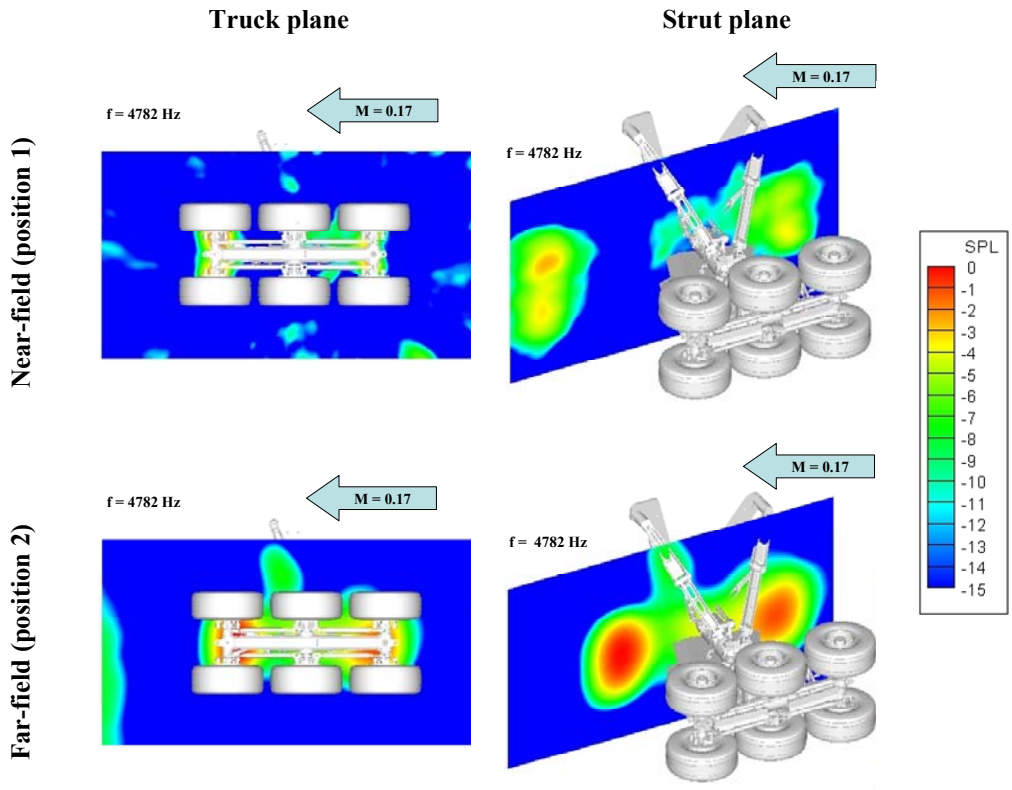

Figure 3.7: Beamforming maps of the landing gear in its baseline configuration, at full scale frequency of 4782 Hz, as obtained with the phased array in the anechoic chamber in positions 1 and 2. Reference 0 dB: peak value of beamforming map in the truck plane.

It is also very interesting to show the results from the array position 3. From the array position 3, the rear and front part of the lower truck appeared very close to each other because of the array orientation and the angle of attack of the landing gear. As a result, when beamforming maps on the truck plane are plotted, the lobes associated with the rear-and front-brakes appear almost at the same location. This is illustrated in Figure 3.8. In the figure, noise generated by the front and rear brakes is projected onto the strut plane for the 3 array positions. From the array position 3, the components of the landing gear such as the braces and strut were not hidden or shielded by the lower truck and much information could be obtained from the maps on the strut plane.

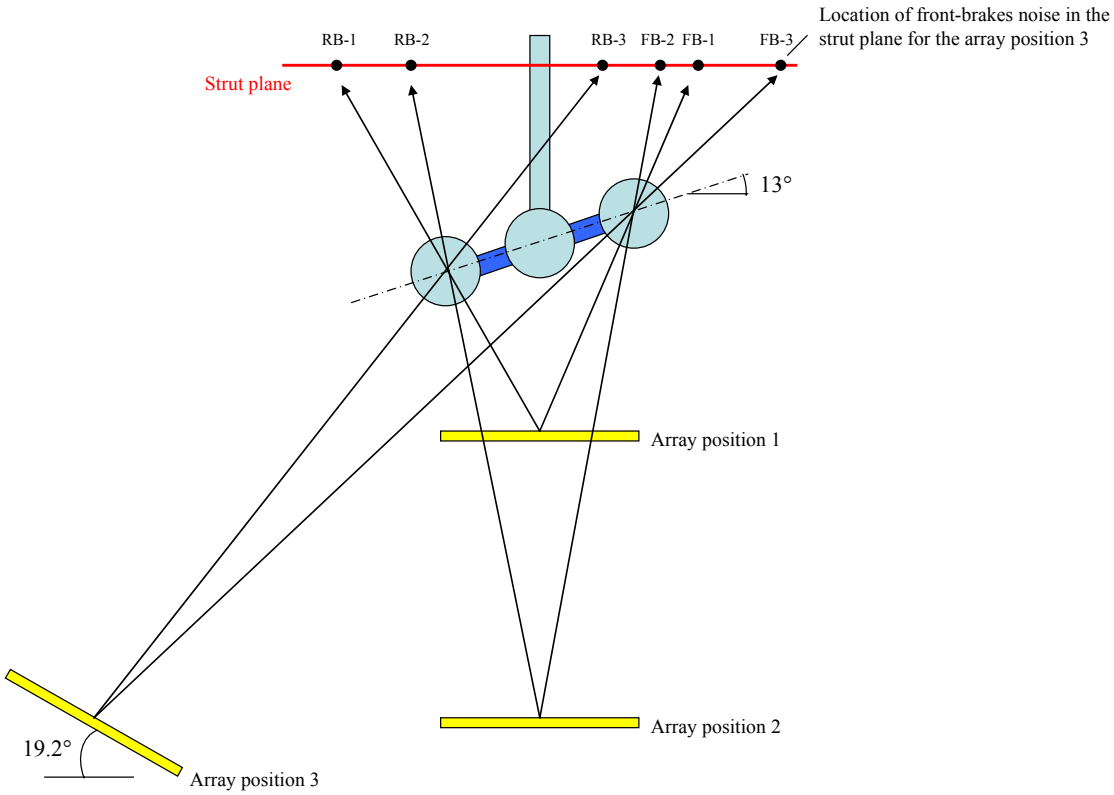

Figure 3.8: Locations of the front- and rear-brakes noise projected onto the strut plane for array positions 1 to 3.

Figure 3.9 depicts the beamforming maps of the landing gear as obtained with the array in positions 2 and 3. The left and right maps correspond to array positions 2 and 3, respectively. Results for the full-scale frequencies of 3381 and 4782 Hz are shown in top and bottom maps, respectively.

The beamforming maps obtained from array positions 2 and 3 look very different, though both positions are in the far-field. As mentioned earlier on, when the array is in position 2 (left maps) noise is not only generated by the lower truck but also by the upstream and downstream braces. However, the projection of the lower-truck noise on the strut plane indicates clearly that the lower truck is still the major noise source. As indicated by the maps, for the array position 3 (right maps), the strut is the major noise component of the landing gear in its baseline configuration. As explained in Figure 3.8, noise generated by the front and rear brakes are projected upstream of the strut onto the strut plane. It will be shown in the next section that if the lower truck is streamlined, the

lobes corresponding to these noise sources are eliminated. Notice the difference in levels between array positions 2 and 3. On the strut plane, noise levels of the gear as obtained with the array in position 3 are nearly 2 dB higher that the levels obtained with the array in position 2 for both frequencies shown. The difference is most likely caused by the noise contribution of the strut that is hidden when the array is in position 2.

Noise from the landing gear on the flyover path cannot be characterized by only taking phased array measurement right under the gear. For instance, some of the strut noise is seen by the array in position 3 whereas it is not in array position 2. This source is radiating on the rear arc of the flyover path and most likely on the forward arc too. These results imply that noise measurements directly underneath the landing gear are not the most representative since it will underestimate the radiation.

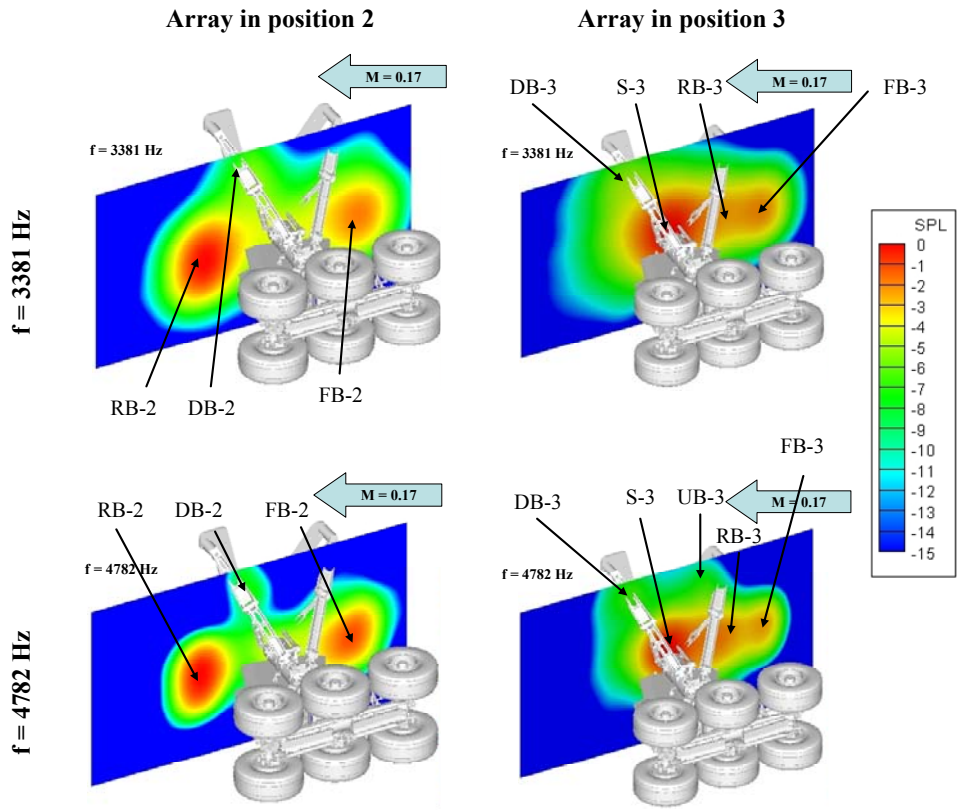

Figure 3.9: Beamforming maps of the landing gear, in its baseline configuration at full scale frequencies of 3381 and 4782 Hz, as obtained with the phased array in the anechoic chamber in positions 2 and 3. Reference 0 dB for each frequency: peak value of beamforming map shown.

3.3 Passive noise control

In this section, the performance of the noise control devices described in Section 2.4.1 is discussed. In past experiments conducted by Ravetta [37], the performance of landing gear noise control devices was evaluated from data collected in the near-field in a hard-walled wind tunnel, i.e. a reverberant environment. It was shown earlier on that, on the flyover path and in the near-field, phased array measurement of the landing gear noise are not reliable. It was also shown that, in the far-field, noise measurements right under the gear are not sufficient to characterize landing gear noise on the flyover path. One of the objectives of this study was to give an accurate estimate of the noise reduction achieved by the noise control devices. The noise reduction was primarily estimated from far-field phased-array measurements conducted in semi-anechoic test section. Additional measurements were performed with a linear array or microphones in the far-field. Data collected with the linear array of microphone was compared to the far-field phased-array results.

The following discussion is based on the data collected with the array placed in the far-field for both positions 2 and 3. The beamforming maps presented in this section have been corrected for amplitude similarly to the far-field results in the previous section or according to the correction curves presented in Appendix B.2.

First, noise reduction is examined qualitatively by looking at the beamforming maps of the landing gear fitted with various noise control devices. Then the noise reduction potential of the streamlining devices is quantified by looking at the difference between integrated spectra of the baseline and streamlined configurations. Noise reduction is also quantified using far-field, single-microphone measurements. The two approaches are compared to assess the best way to estimate noise reduction in semi- anechoic wind tunnels.

For each frequency, the reference 0 dB corresponds to the peak value of the beamforming map of the baseline landing gear as obtained with the array in position 3.

3.3.1 Lower-truck noise reduction

Figures 3.10 and 3.11 show the beamforming maps of the baseline (top maps), VT-lower-truck-fairing (middle maps), and NASA-toboggan (bottom maps) configurations of the landing gear at the full scale frequencies of 3381 and 4782 Hz, respectively. In both figures, results are shown in the strut plane. As mentioned earlier, beamforming maps aid in discussing qualitatively the noise generated by the model. Most of the useful information may be extracted from looking at the beamforming maps in the strut plane. Noise generated by the lower truck may still be seen on the strut plane but its levels are not representative. The actual levels of the truck noise may be obtained from the beamforming maps in the truck plane shown in Appendix A of reference 39 (Figures A.15 and A.16). In the same reference, additional maps at lower frequencies are shown.

The beamforming maps of the landing gear fitted with the VT lower-truck fairing are described first (middle maps in Figures 3.10 and 3.11). A comparison with the baseline configuration (top maps) indicates that the VT lower-truck fairing manages to reduce noise from the lower truck. For instance, for the array in position 2 (left middle maps), the reduction of the peak level in the strut plane due to the VT-lower-truck fairing is about 3.9 and 4.8 dB at 3381 and 4782 Hz, respectively. The reduction as seen in the truck plane is 3.4 and 4.1 dB at 3381 and 4782 Hz (see Appendix A in reference 39). Consequently, for the array in position 2, noise from the downstream and upstream braces may be identified more clearly than in the baseline configuration. From the array in position 3, most of the landing gear components were not acoustically shielded by the lower truck. As a result, the performance of the truck fairing is deteriorated. For the array in position 3 (right middle maps), the noise reduction due to the VT-lower-truck fairing is about 2.1 and 1.2 dB at 3381 and 4782 Hz, respectively As shown in Figures 3.10 and 3.11 (right middle maps), the strut and the braces are the major noise sources whereas noise from the lower truck is hardly identifiable.

Now consider the model as fitted with the NASA toboggan. Figures 3.10 and 3.11 (bottom maps) indicate that the NASA toboggan was very effective at suppressing noise

from the lower truck at 3381 Hz and totally eliminated it at 4782 Hz, i.e. the source cannot be seen by the array. For the array in position 2, at 3381 Hz (Figure 3.10 – left bottom map), the downstream brace appears as the major noise source. At 4782 Hz, (Figure 3.11 – left bottom map), the downstream brace and the leading edge of the door are the major noise sources. At 4782 Hz, neither in the baseline configuration nor in the VT lower-truck-fairing configuration (Figure 3.11 - top and middle maps), could the leading edge of the door be identified as a noise source. For the array in position 2 and the landing gear in its NASA-toboggan configuration (Figure 3.11 – left bottom map), the door could be identified as a noise source because other major noise sources were sufficiently reduced. For the array in position 3 (Figure 3.11 – right bottom map), the noise generated by the leading edge of the door cannot be identified, most likely because the noise levels of the strut are significantly larger. Noise from the upstream brace may also be clearly identified but its levels are 5.6 and 9.5 dB lower than the downstream brace at 3381 and 4782 Hz, respectively.

Note that for the array in position 3, the strut appears as a major noise source, regardless the type of device streamlining the lower truck. Therefore, the noise reduction potentials of the VT-lower truck fairing and the NASA-toboggan is expected to be poor or not sufficient when viewed from a position other than straight under the landing gear, i.e. the upper landing gear components such as the strut, braces, and so forth are not acoustically shielded by the truck. This implies that an effective noise control of the landing gear must include the reduction of the strut source in addition to the truck.

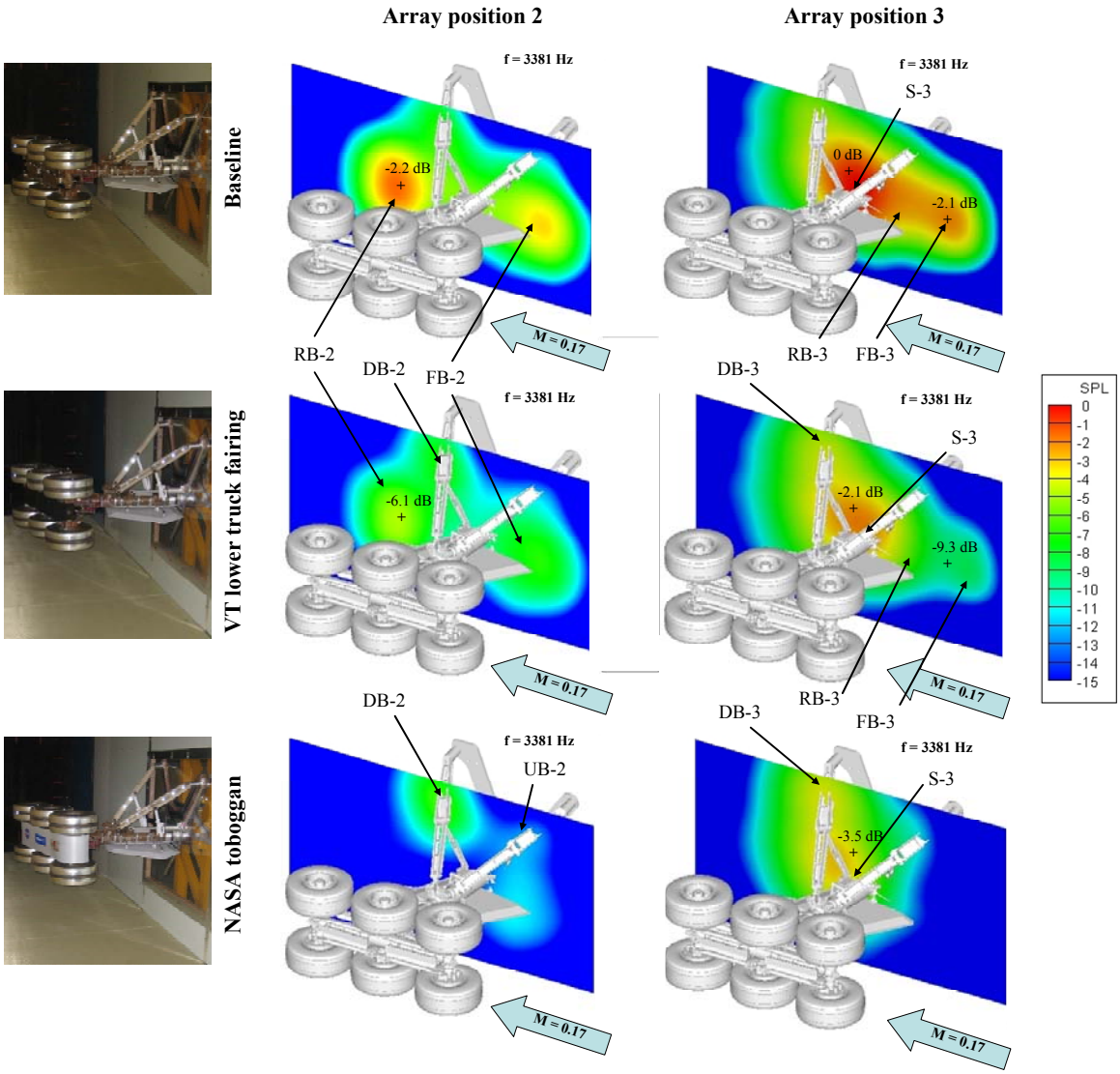

Figure 3.10: Beamforming maps of the baseline, VT-lower-truck-fairing, and NASA-toboggan configurations of the landing gear at full scale frequency of 3381 Hz, as obtained with the phased array in the anechoic chamber in positions 2 and 3. Reference 0 dB: peak value of beamforming map of the baseline landing gear with array in position 3 (top right map).

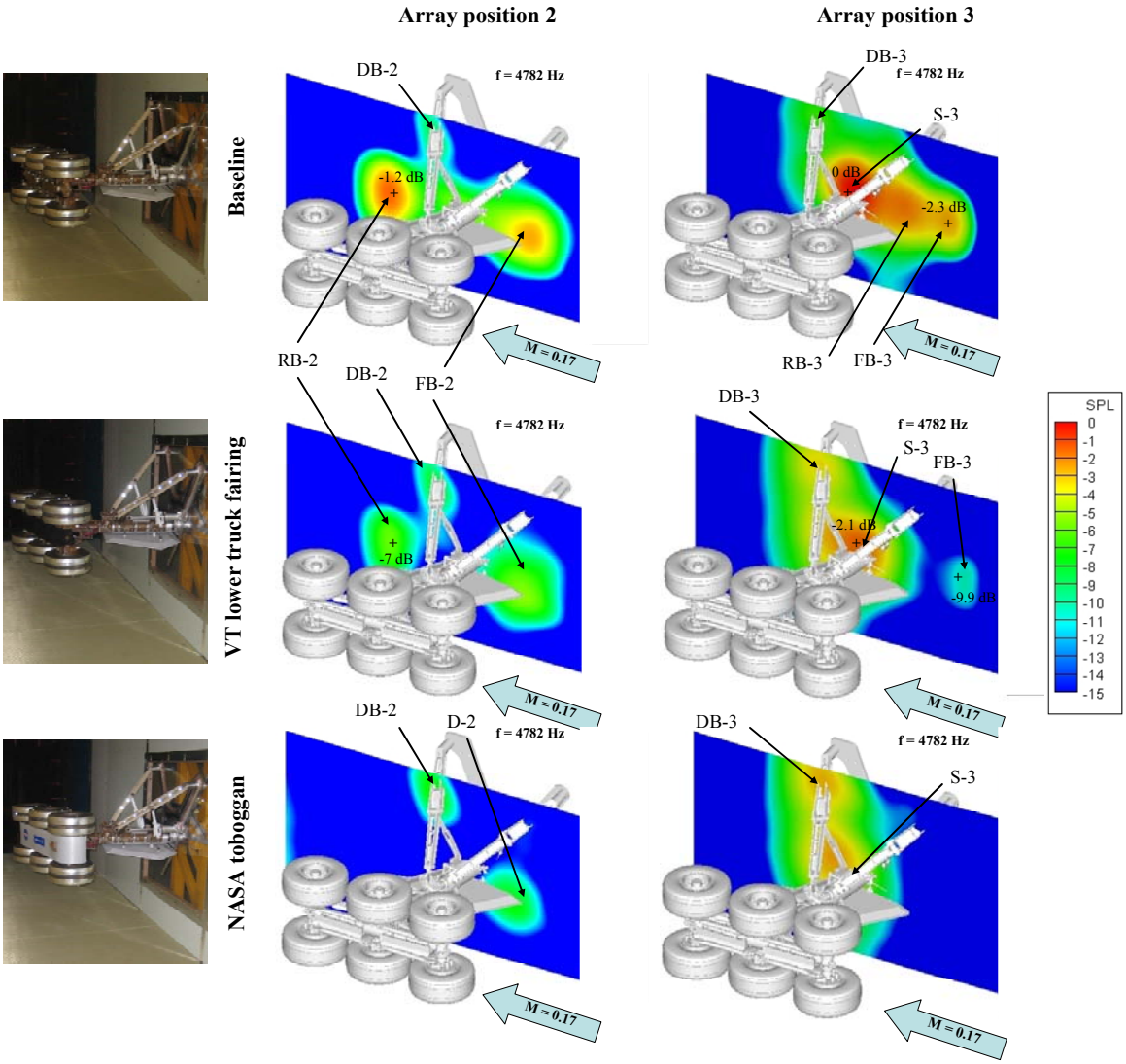

Figure 3.11: Beamforming maps of the baseline, VT-lower-truck-fairing, and NASA-toboggan configurations of the landing gear at full scale frequency of 4782 Hz, as obtained with the phased array in the anechoic chamber in positions 2 and 3. Reference 0 dB: peak value of beamforming map of the baseline landing gear with array in position 3 (top right map).

3.3.2 Braces and strut noise reduction

Figures 3.12 and 3.13 depict the beamforming maps of the baseline (top maps), VT-lower-truck-fairing (middle maps), and all-VT-fairings (bottom maps) configurations of the landing gear. Results are shown for full scale frequencies of 3381 and 4782 Hz in Figures 3.12 and 3.13, respectively. The VT-lower-truck-fairing and all-VT-fairings configurations are compared to show the noise reduction achieved by the strut and braces fairings for both far-field positions of the array.

For array position 2, noise generated by the braces and the door is much lower in the all-VT-fairings configuration than in the VT-lower-truck-fairing configuration. For instance, noise from the downstream brace is reduced by about 6.7 at 3381 Hz and by more than 10 dB at 4782 Hz. When the array is in position 3, noise reduction occurs at the links and downstream brace locations. Noise from the downstream brace is reduced by about 5.1 and 2.7 dB at 3381 and 4782 Hz, respectively.

Like the lower-truck-fairings discussed in the previous section, the noise reduction potential of the strut and braces fairings is reduced as the array is moved from straight under the gear (position 2) to the rear arc (position 3).

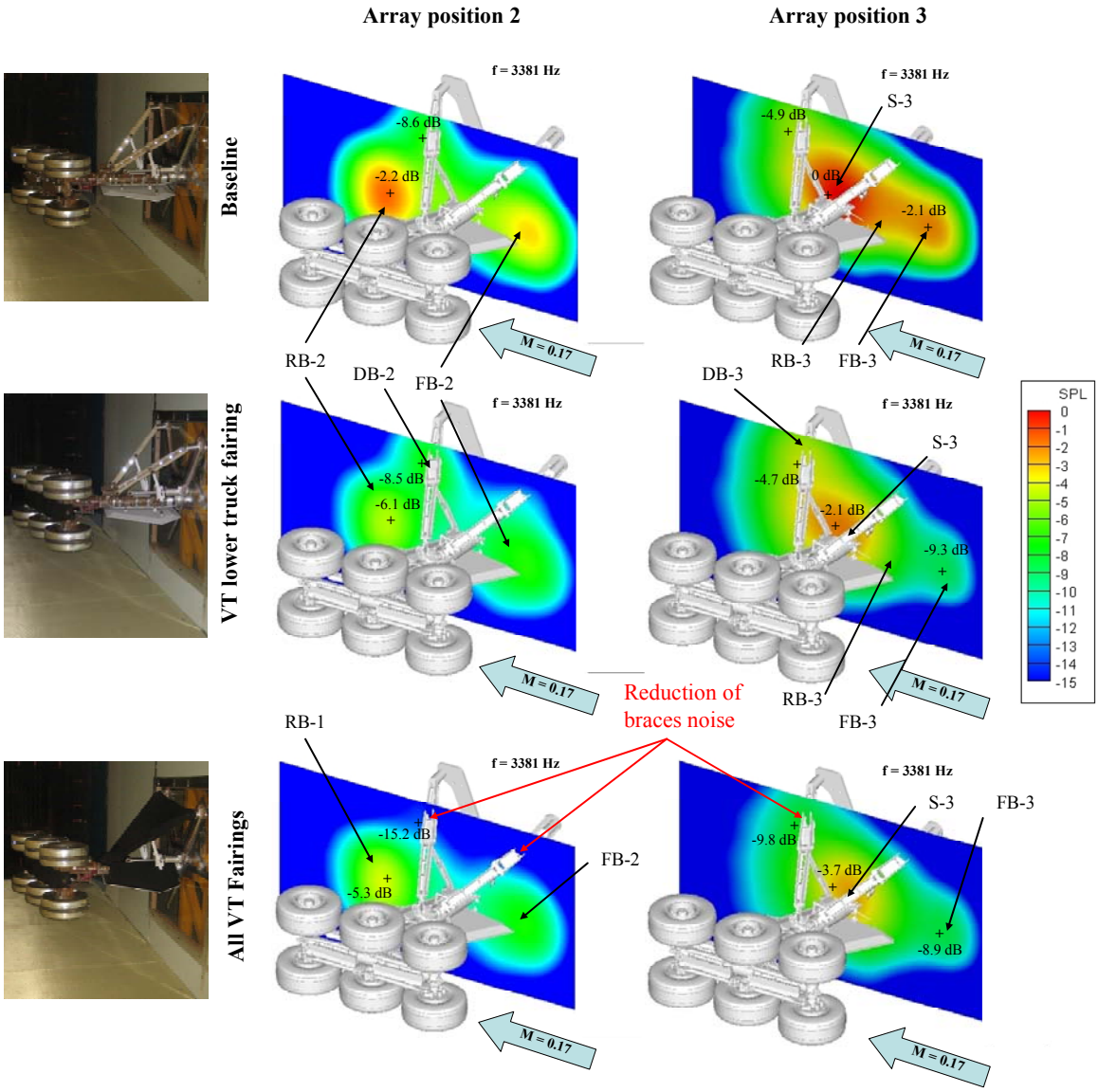

Figure 3.12: Beamforming maps of the baseline, VT-lower-truck-fairing and all-VT-fairings configurations of the landing gear at full scale frequency of 3381 Hz, as obtained with the phased array in the anechoic chamber in positions 2 and 3. Reference 0 dB: peak value of beamforming map of the baseline landing gear with array in position 3 (top right map).

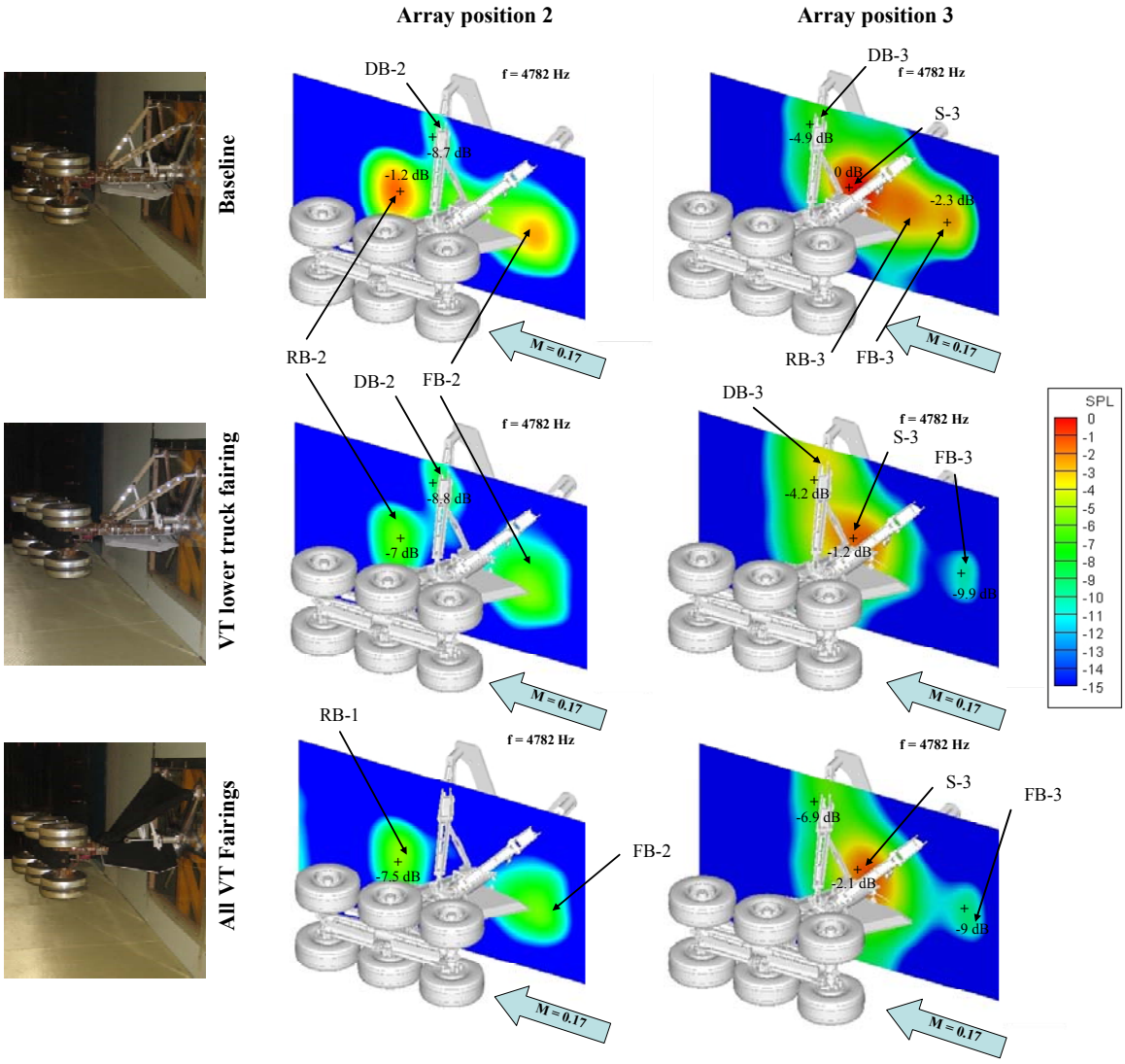

Figure 3.13: Beamforming maps of the baseline, VT-lower-truck-fairing and all-VT-fairings configurations of the landing gear at full scale frequency of 4782 Hz, as obtained with the phased array in the anechoic chamber in positions 2, and 3. Reference 0 dB: peak value of beamforming map of the baseline landing gear with array in position 3 (top right map).

3.3.3 Quantification of noise reduction

In the previous section, noise reduction was discussed qualitatively using beamforming maps of the landing gear on selected planes. In this section, the noise reduction potential of the noise control devices is discussed quantitatively by two methods. First, data from the far-field, phased-array measurements are used to plot the integrated spectra of the landing gear noise in its various configurations. The noise reduction is then estimated from the spectral difference between configurations. Noise

reduction was also estimated in the near-field for comparison with the far-field results. Secondly, noise reduction was estimated from far-field single-microphone measurements. The objectives of these far-field single-microphone measurements were to determine the directivity pattern of landing gear noise in the far-field and to study how phased-array results relate to far-field, single-microphone measurements in term of noise reduction estimation. Finally, the noise reduction estimates from both methods are compared.

Note that no correction has been applied to the data to predict the reduction for an actual flight configuration of the aircraft. These corrections, described in reference 40, are beyond the scope of this study and will not be applied to the results presented in this section.

3.3.3.1 Quantification of noise reduction by integration of the beamforming maps

The beamforming maps of the landing gear noise in its various configurations were integrated. Like in Section 3.1, the volume of integration was a grid of 323031 points, encompassing the entire landing gear, and with dimensions 70 x 56 x 39 inches. The objective was to quantify the noise reduction of the whole landing gear rather than individual components so that results can be compared to the far-field, single-microphone measurements.

Figures 3.14 and 3.15 depict the noise reduction due to the NASA toboggan (blue curve), VT-truck-fairing (red curve), and all VT fairings (truck, braces, and strut fairings - green curve). Results in Figure 3.14 indicate that when the array is in position 2, the NASA toboggan achieves up to 7.7 dB noise reduction at 3000 Hz. The VT-lower-truck fairing and all-VT-fairings configurations have levels up to 3 dB and 4.5 dB quieter than the baseline gear, respectively. Therefore, when the array is in position 2, the NASA toboggan is the most effective passive noise control device. This result is consistent with the observations made in Sections 3.3.1 and 3.3.2 that the NASA toboggan was the most effective truck device, producing reductions beyond what the array could identify.

As indicated by the results in Figure 3.15, for the array in position 3, the noise reduction achieved by the NASA toboggan is only up to a maximum of 4 dB at 3000 Hz as compared to 7.7 dB underneath the gear (array position 2). As a result, the NASA toboggan and all the VT fairings achieve comparable noise reduction. The effectiveness of the VT braces and strut fairings is much more noticeable for the array in position 3 than for the array in position 2. For instance, for the array in position 2 at 5000 Hz, both the VT-truck and all the VT fairings achieved the same 3 dB reduction. On the other hand, for the array in position 3 at 5000 Hz, the all-VT-fairings configuration is 1 dB quieter than the VT-lower truck fairing configuration. These observations are in very good agreement with the beamforming maps discussed earlier on. It was shown that, as the array is moved to a position where the strut and the braces are no longer shielded by the lower truck, the effectiveness of a device streamlining the lower truck only (VT lower truck fairing or NASA toboggan) is significantly reduced.

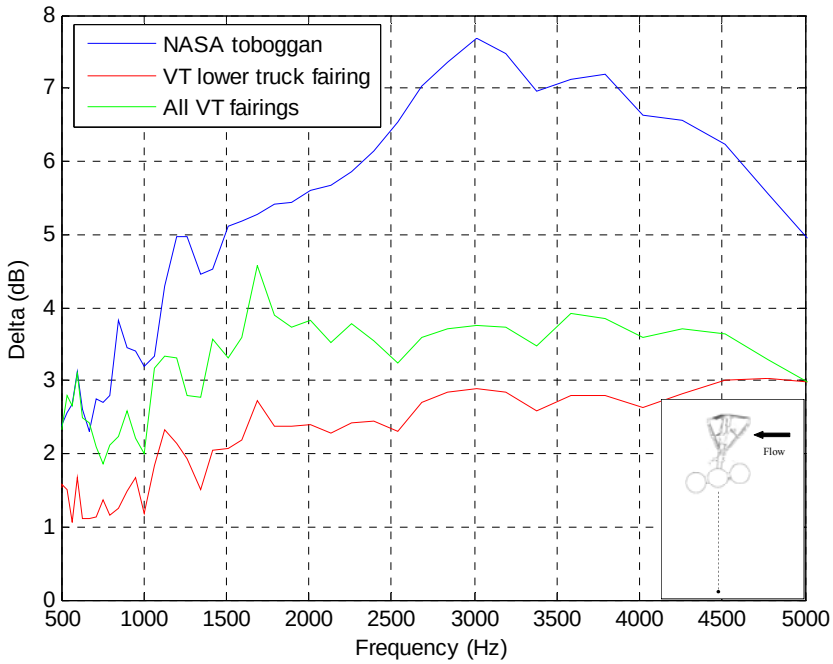

Figure 3.14: Noise reduction due to the NASA toboggan (blue curve), VT-lower-truck-fairing (red curve), and all VT fairings (truck, braces, and strut fairings - green curve) as estimated with the integrated spectra. The phased array was in the far-field in position 2.

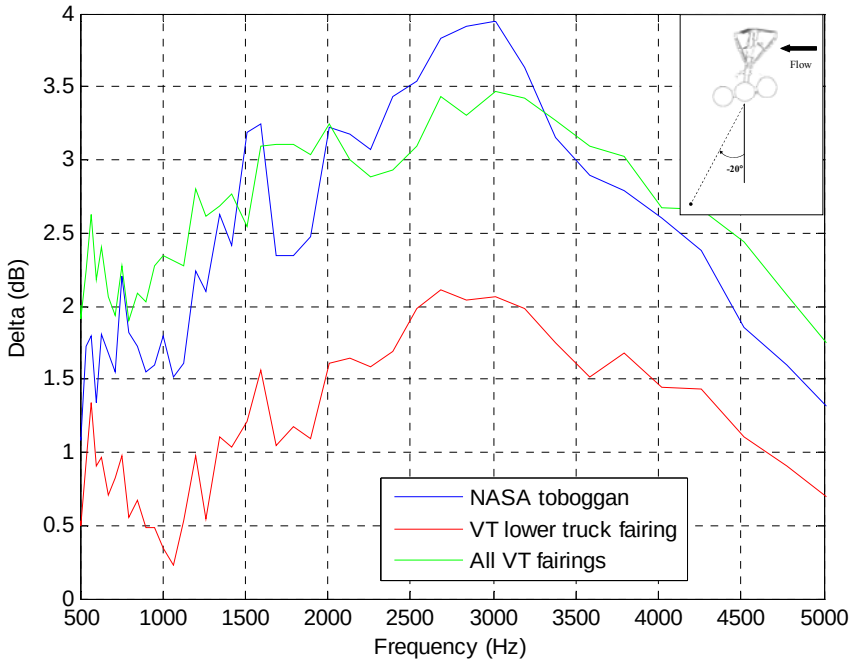

Figure 3.15: Noise reduction due to the NASA toboggan (blue curve), VT-lower-truck-fairing (red curve), and all VT fairings (truck, braces, and strut fairings - green curve) as estimated with the integrated spectra. The phased array was in the far-field in position 3.

The above results suggest that a larger noise reduction may be achieved if the NASA toboggan is used in conjunction with the VT braces and strut fairings. To this end, the noise reduction that the braces and strut fairings would achieve alone was estimated. The result was then added to the noise reduction achieved by the NASA toboggan to obtain the noise reduction due to the combination of the NASA toboggan and VT-fairings. Let Δ_T, Δ_{SB}, Δ_{TSB}, and Δ_N denote the noise reduction from the VT-truck fairing, VT-strut+braces fairings, truck+strut+braces fairings, and NASA-toboggan, respectively. The noise reduction from the strut+braces fairings may be estimated with the following relation,

$$\Delta_{SB} = \Delta_{TSB} - \Delta_T. \tag{3.2}$$

This estimated noise reduction due to the VT-strut+braces can now be added to the NASA-toboggan fairing. Figure 3.16 depicts the noise reduction due to the NASA toboggan plus the VT-braces and -strut fairings (solid curves) and NASA toboggan alone (dashed curves) as measured with the phased array in the far-field in positions 2 (blue curves) and 3 (red curves). On the flyover path, straight under the landing gear, the noise reduction due to the NASA+VT fairings (solid blue curve) ranges from 3.5 dB at 500 Hz

to 8.5 dB at 3000 Hz. On the rear arc (solid red curve) the reduction is more modest and ranges from 2.5 dB at 5000 Hz up to 5.3 dB at 3000 Hz. For both array positions, levels of the solid curve are higher than the ones of the dashed curve. In other words, adding the VT braces and strut fairings to the NASA-toboggan configuration results in a significant increase in noise reduction ranging from 0 to 1.84 dB for the array in position 2 and from 0.5 to 2.1 dB for the array in position 3.

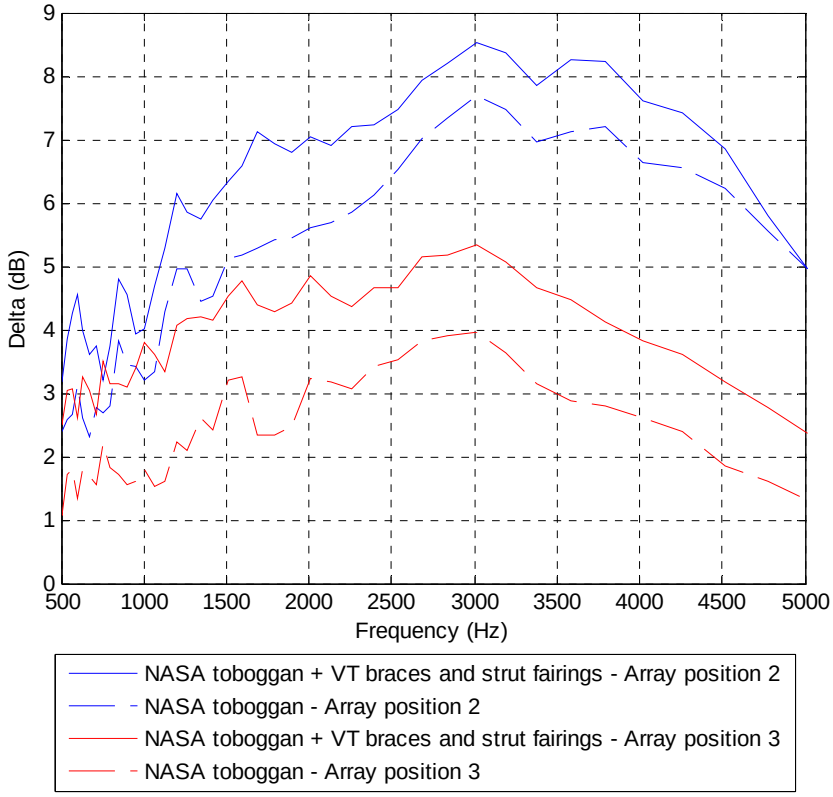

Figure 3.16: Noise reduction due to the NASA toboggan plus the VT braces and strut fairings (solid curves) and NASA toboggan alone (dashed curves) as estimated with the integrated spectra. The phased array was in the far-field in positions 2 (blue curves) and 3 (red curves).

Figure 3.17 shows the same results as Figures 3.14 and 3.15 except that the noise reduction was estimated from measurements conducted in the VT hard-walled wind tunnel, in the near-field of the model. On the flyover path, right under the gear, the landing gear noise reduction was estimated to be up to 15.2 dB at 2130 Hz. Noise reduction due to the VT-lower-truck fairing (red curve) is comparable to the one achieved by all the VT fairings (green curve). These observations are consistent with the analysis

presented in this chapter. The NASA toboggan was shown to significantly reduce noise from the lower truck. In the near-field, noise generated by components behind the truck cannot be seen. Therefore, with the array in the near-field, the noise reduction achieved by the NASA toboggan on the overall landing gear noise is overestimated. The same reasoning explains why the VT-lower truck fairing and all the VT fairings achieve comparable noise reductions.

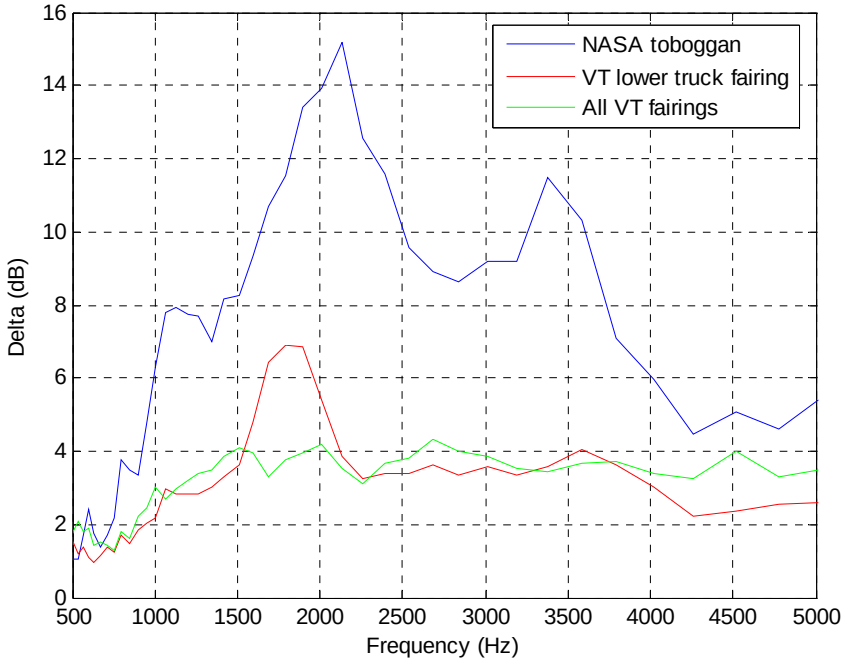

Figure 3.17: Noise reduction due to the NASA toboggan (blue curve), VT-lower-truck-fairing (red curve), and all VT fairings (truck, braces, and strut fairings - green curve) as estimated with the integrated spectra. Hard-walled test section - phased array in the near-field in position 1.

3.3.3.2 Quantification of noise reduction using single-microphone measurements

The second approach to estimate the noise reduction due to the control devices was to use far-field, single-microphone measurements. As mentioned earlier, the objectives of these far-field measurements were to determine the directivity pattern of landing gear noise in the far-field and to study how phased-array results relate to far-field, single-microphone measurements in term of noise reduction estimation.

First, measurements were carried out with the linear array of 15 microphones described in Section 2.3.2. As explained in Section 2.4.2, the linear array was placed in

the far-field about 10 inches from the back of the chamber. Though the microphones were positioned along a straight line, data was plotted along an arc with constant radius r = 123 inches. To this end, acoustic data was corrected using the spherical spreading law. The center of this arc was chosen such that the center microphone of the linear array was aligned with the center of the lower truck. The radiation pattern was determined from ±30°. Tests were conducted at M = 0.12 and 0.15 with the landing gear in its baseline and NASA-toboggan configurations (see Table 2.2). Noise generated by the landing gear is determined by its aerodynamic load and the squared sound pressures are expected to increase with the 6th power of flow velocity [4]. Data collected at M = 0.15 was then corrected to estimate the noise generated by the landing gear at M = 0.17 by using the 6^{th} power relationship.

Due to time limitation, only four cases could be tested with the linear array. As an alternative to the far-field microphone, one of the microphones in the phased-array located the closest to the array center was used as a far-field, single microphone. The microphone was calibrated with a pistonphone. The sound pressure levels were subtracted 6 dB to account for the presence of the hard surface of the array. The distance from the center of the truck to the single microphone in the array (basically the array center) is denoted by d_n where the subscript n indicates the array position. For the array in position 3, data was corrected using the spherical spreading law such that the noise levels were computed for $d_3 = d_2 = 129$ inches (3.28 m).

In the linear-array results, the landing-gear noise levels included the background noise. The actual noise levels may be obtained by removing the background noise from the data. Unfortunately, the background noise levels could not be measured during the landing-gear test entry (again due to time constrains). Measurements from another entry in the fully-anechoic wind tunnel (one anechoic chamber on each side of the test section) were used to provide an estimate of the background noise levels in the semi-anechoic test section. Data was collected with a single microphone from another 63-element microphone phased array at M = 0.092. To estimate the background noise at M = 0.17, data collected at M = 0.092 was corrected using the 6^{th} power of the flow velocity.

In the rest of the document, single microphones from the linear array and phased array are denoted by LM_n and PM_n, respectively, where the subscript n refers to the location of the single microphone. Straight under the landing gear (phased-array position 2) and on the rear arc (phased-array position 3), the index n takes values 2 and 3, respectively.

Figure 3.18 shows the radiation pattern of the landing gear in its baseline (top maps) and NASA-toboggan (bottom maps) configurations at full-scale frequencies of 1898 (left maps), 3381 (center maps), and 4782 Hz (right maps). Note that the background noise was not removed from these results. The directivity pattern of the baseline landing gear noise (top maps) suggests that noise levels do not vary much as the radiation angle changes. At full-scale frequencies of 1898, 3381, and 4782 Hz, levels of the baseline landing gear noise reach maxima at 8.8, 21.7, and 21.7°, and minima at -17.5, 4.4, and 4.4°, respectively. For the three frequencies shown, a comparison between the landing gear with (bottom) and without (top maps) the NASA toboggan indicates that the NASA toboggan achieves significant noise reduction but does not alter the directivity pattern.

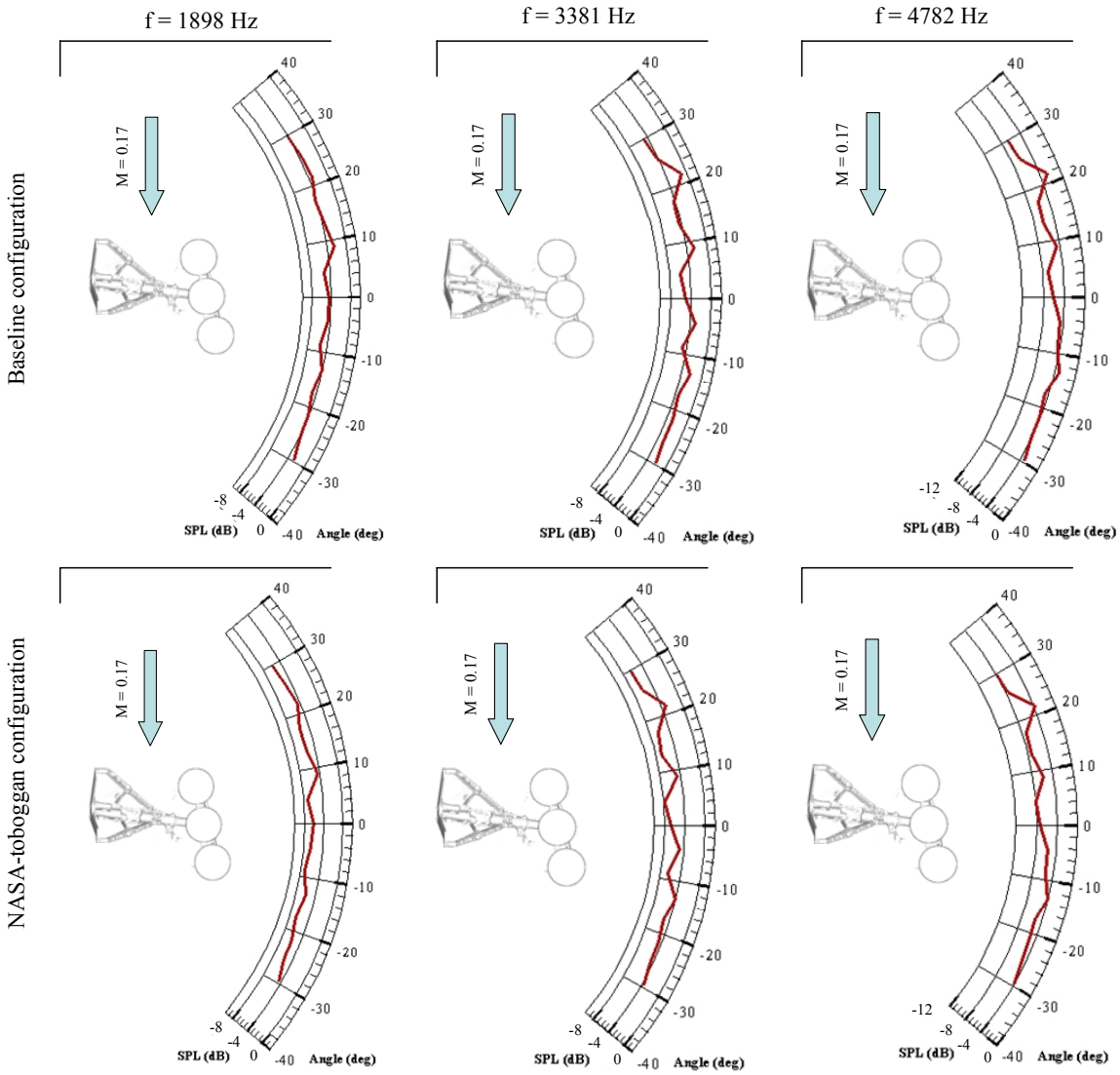

Figure 3.18: Radiation pattern of the landing gear in its baseline (left maps) and NASA-toboggan (right maps) configurations at M = 0.17 as obtained with the linear array of 15 microphones on the flyover path at full-scale frequencies of 1898 (top maps), 3381 (middle maps), and 4782 Hz (bottom maps).

A more convenient way to discuss the noise reduction potential of the NASA toboggan is to plot the difference between the radiation patterns of the baseline and NASA-toboggan configurations, i.e. difference between left and right curves in Figure 3.18. Figure 3.19 shows the noise reduction achieved by the NASA toboggan as functions of angle and frequency. In the figure, a positive value corresponds to a noise reduction.

The results indicate that noise reduction reaches maxima between 2392 and 3383 Hz, depending on the angle considered. For instance, at an angle of 0° (microphone LM_2) which corresponds to radiation directly underneath the landing gear, the noise reduction reached a maximum of 2.9 Hz at 2534 Hz. At an angle of -20° (LM_3), the maximum reduction is observed at 3014 Hz and is about 2.9 dB. At higher and lower frequencies from the 2400-3400 Hz range, the noise reduction rolls off from the maximum of around 3 dB to 1 dB.

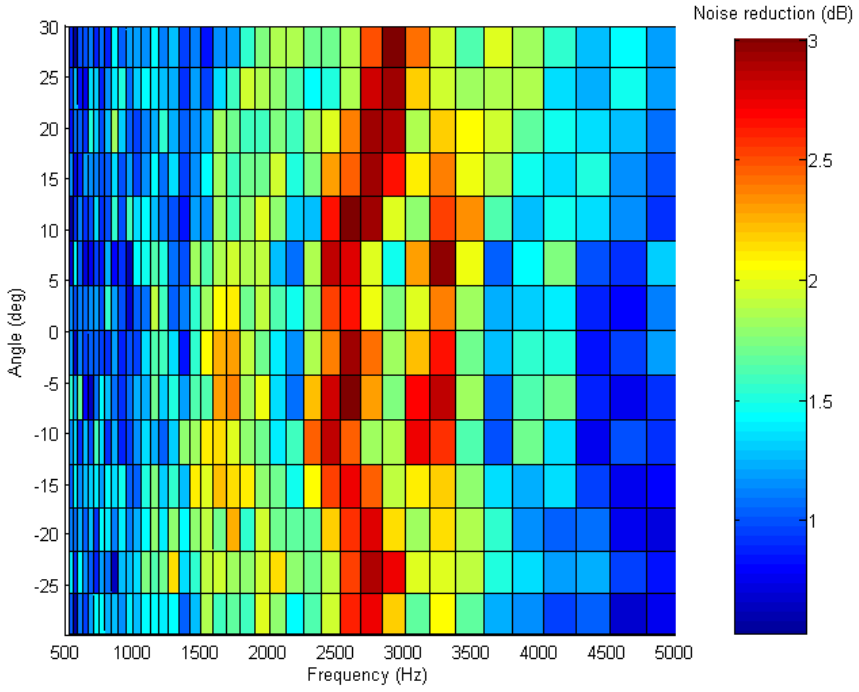

Figure 3.19: Noise reduction achieved by the NASA toboggan as functions of angle and frequency.

Figure 3.20 depicts the noise spectrum in 12th octave bands of the baseline landing gear measured with microphones PM_2 (blue curve – underneath the landing gear or 0° angle) and PM_3 (red curve - rear sector at -20° angle). Background noise was not removed from the data, i.e no background noise correction. Therefore in Figure 3.20, the levels corresponding to the landing gear noise are higher than the actual ones. The estimate of the background noise levels in the semi-anechoic test section is also plotted (magenta curve). The background noise levels are 4 to 10 dB below the landing gear noise depending on frequency and microphone position.

At M = 0.17 and at full-scale frequencies of 1898, 3381, and 4782 Hz, noise levels of the baseline landing gear, as measured with PM_2 (blue curve), are 67.7, 64.3, and 63.2 dB, respectively. The same levels measured with LM_2 yielded 67.6, 63.2, and 61.9 dB, respectively (Figure 3.18 – top maps). Results are in very good agreement considering the many differences between the measurement systems. For example, in the linear array, the microphones were not baffled and the mounting support was acoustically treated. On the other hand, the single microphone of the phased array was flushed with an aluminum plate. Therefore, the single microphone measurements can be estimated using a microphone from the phased array.

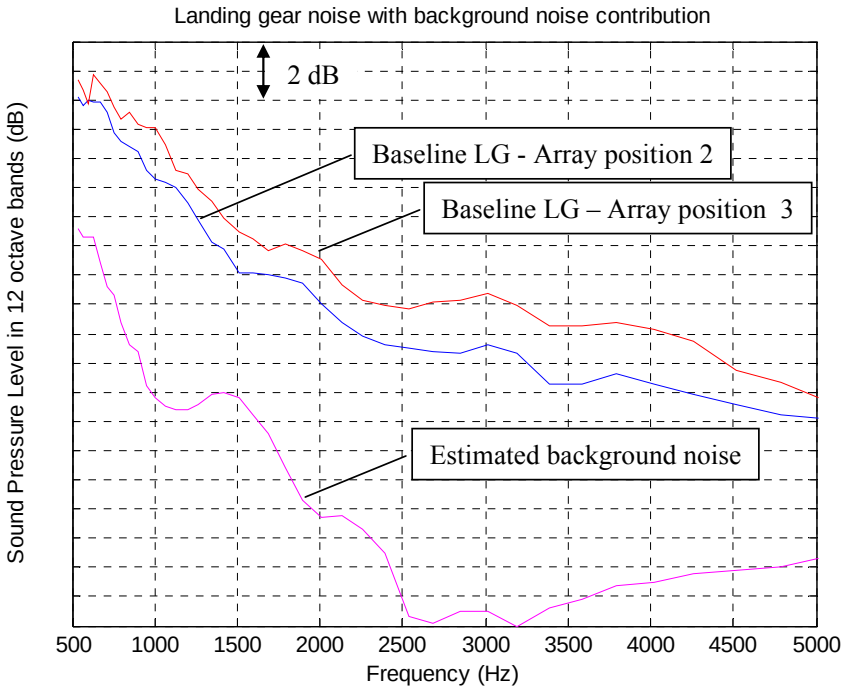

Figure 3.20: Sound pressure levels in 12th octave band of the baseline landing gear as measured with a PM_2 (blue curve) and PM_3 (red curve). Data not corrected for background noise. Background noise levels in 12th octave bands in the fully-anechoic test section (magenta curve).

Figure 3.21 shows the same results as in Figure 3.20 but the background noise was removed from the data. Levels of the landing gear are higher on rear arc (red curve), than straight under the gear (blue curve) at all frequencies. The difference in levels ranges from 0 to 2.3 dB. As shown in Section 3.2, in the far-field straight under the gear, some of the noise sources located behind the truck cannot be located. However, the contribution of these noise sources to the overall landing gear noise is significant on the

rear arc. Levels of the overall landing gear noise are thus expected to be higher on the rear arc than straight under the gear.

Figure 3.21: Sound pressure levels in 12th octave band of the baseline landing gear as measured with a PM_2 (blue curve) and PM_3 (red curve). Background noise was removed from the data.

To better visualize noise reduction, the spectral difference between baseline and noise control configurations was plotted. First, data was plotted without removing the background noise for comparison with the linear-array results. The background noise was then removed to estimate the actual noise reduction.

Figure 3.22 depicts the noise reduction due to the NASA toboggan. The noise reduction was estimated with PM_2 (blue solid curve) and LM_2 (blue dashed curve). Background noise was not removed from the data. Both curves exhibit very similar patterns, e.g. far-field single microphone data from the linear and phased array are in fairly good agreement. In both cases, the NASA toboggan achieves a maximum noise reduction of about 3 dB in the range 2500 – 3000 Hz. The curves roll off to 1 dB as the frequency approaches 500 and 5000 Hz. Once again these results indicate that the single microphone measurements can be estimated using a microphone from the phased array.

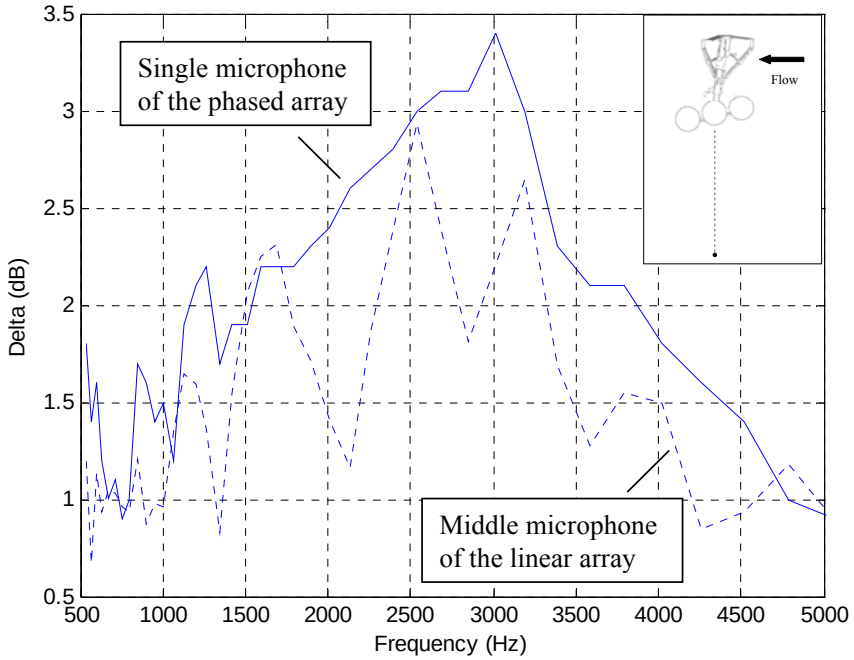

Figure 3.22: Noise reduction from single far-field microphone due to the NASA toboggan estimated with PM_2 (solid curve) and LM_2 (dashed curve).

Figure 3.23 depicts the noise reduction due to the NASA toboggan (blue curve), VT-lower-truck fairing (red curve), and all VT fairings (green curve). Data was collected with a single microphone of the phased array in positions 2 (Figure 3.23a) and 3 (Figure 3.23b). Background noise was again removed from the data. As a result, levels of noise reduction due to the NASA toboggan differ in Figures 3.22 and 3.23a (solid blue curve in both figures). The results shown in Figure 3.23 are thus closer to the actual levels of noise reduction but still remain an estimate. The main reason is that the background noise was estimated from measurements in the fully-anechoic wind tunnel at lower speed. Therefore, the data had to first be extrapolated from M = 0.092 to 0.17. The second possible source of error is due to the fact that measurements were performed with another measurement system in a different configuration of the facility, e.g. larger 63-element microphone phased array in fully-anechoic wind tunnel. In this sense, the background noise levels in Figure 3.20 (magenta curve) are probably underestimated. Consequently, the noise reduction potential of the NASA toboggan is also probably underestimated.

In the frequency range of 2000 – 3500 Hz and for PM_2 (Figure 3.23a), the NASA toboggan is the most effective noise control device. At 3000 Hz, a 4.2 dB noise reduction is achieved by the NASA toboggan, as compared to 3.4 dB when background noise is not removed from the data. Comparing the solid blue curves in Figure 3.22 and 3.23a suggests that if the actual background noise levels in the semi-anechoic test section were used, levels of noise reduction in Figure 3.23 should be higher. In the frequency ranges of 500 – 1600 Hz and 3500 – 5000 Hz, the NASA toboggan and all the VT fairings achieve comparable noise reductions. The curves corresponding to the VT-lower-truck fairing and all-VT fairings, red and green curves, respectively, have similar pattern. However, the VT-lower-truck fairing alone is significantly less effective than when all VT fairings are used. For example, in the frequency range of 2000 – 4000 Hz, the VT lower-truck fairing alone (red curve) is about a decibel less effective. In Figure 3.23a, the three curves exhibit a peak around 1550 Hz. This peak is the result of a noise reduction of a landing gear component radiating noise at 1550 Hz. In Figure 3.14 where the integrated spectra difference between configurations is plotted, a peak was also observed around 1550 Hz for the VT-lower-truck-fairing and all-VT-fairings configurations. However, the amplitude of this peak was smaller.

In the frequency range of 500 – 3000 Hz and for PM_3 (Figure 3.23b), the NASA-toboggan and all the VT fairings achieve comparable noise reduction. Both devices are most effective at 3000 Hz and reduce the landing gear noise by about 2.5 dB, as compared to a maximum of 4.2 dB with the array in position 2. Like for the integrated spectra results shown in Section 3.3.1, the noise reduction potential of the streamlining devices as estimated with a single microphone is smaller on the rear-arc than straight under the landing gear. For frequencies larger than 3000 Hz, all the VT fairings combined are 0.5 dB more effective than the NASA toboggan in reducing landing gear noise.

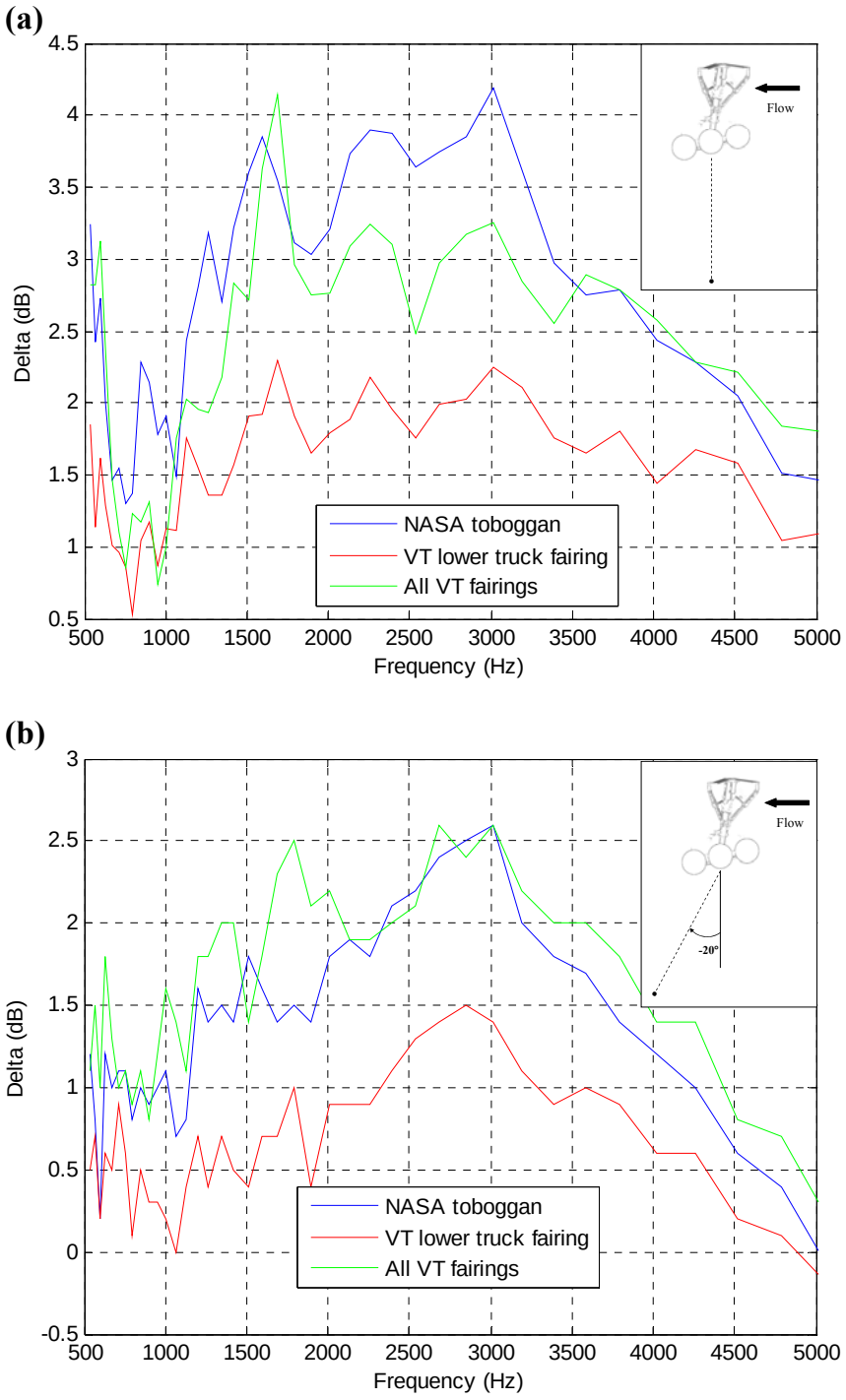

Figure 3.23: Noise reduction from single far-field microphone due to the NASA toboggan (blue curve), VT-lower-truck fairing (red curve), and all VT fairings (green curve). Data was collected with MP_2 underneath the gear (Figure 3.23a) and MP_3 in the rear arc (Figure 3.23b). Background noise was removed from the data.

3.3.3.3 Comparison between two methods for estimating noise reduction

In Sections 3.3.3.1, noise reduction was estimated by integrating the beamforming maps of the landing gear noise in its various configurations and then by calculating the integrated spectra difference between baseline and streamlined configurations. In Section 3.3.3.2, noise reduction was estimated by using far-field, single-microphone measurements. In this section, the two approaches are compared.

In Figures 3.14 and 3.15, noise reduction was estimated using the integrated spectra for far-field phased array positions 2 and 3, respectively. Far-field, single microphones measurements are shown in Figures 3.23a and b, for MP_2 and MP_3, respectively. To make the comparison easier, the results from these figures are plotted together in Figures 3.24 and 3.25 for the two positions. The solid and dashed curves correspond to phased array (integrated spectra) and single microphone measurements, respectively.

Qualitatively, single-microphone and phased-array measurements are in good agreement i.e. results show same trends and relative attenuation between control devices. For both far-field positions, both approaches indicated that the fairings tested achieved the largest noise reduction around 3000 Hz and some significant noise reduction in the frequency range of 1500 and 2000 Hz. Both approaches also showed that the NASA toboggan is the most effective noise control device straight under the gear (position 2), but as effective as all the VT fairings combined on the rear arc (position 3).

However, in term of reduction levels there are some differences between phased array and single-microphone measurements. This is particularly evident for the NASA toboggan straight under the gear (position 2) with differences in the reduction levels as high as 3.5 dB. For the VT devices and both array positions, the difference between the two methods is much smaller, i.e. 0.5-1 dB. It is consistently observed that phased-array estimated noise reduction is always larger than single microphone results. For example, phased-array results predicted maximum noise reductions of 7.7 and 4 dB for the NASA toboggan, from array positions 2 and 3, respectively. On the other hand, single-microphones results predicted 4.2 and 3.0 dB.

Possible sources or causes for the difference in levels are the reflections of the landing gear noise on the hard wall of the semi-anechoic test section, flow effects, and background noise. In the phased-array results, the reflections and background noise were removed from the data by the beamforming process, e.g. using diagonal removal. The flow effects were accounted for by using a Green's function, exact solution of the convected wave equation. On the other hand, reflections and flow effects were not removed from the single-microphone results. Besides, single-microphone results were corrected for background noise using, most likely, underestimated background noise levels. The effect of each possible source for the difference was not quantified and is beyond the scope of this study.

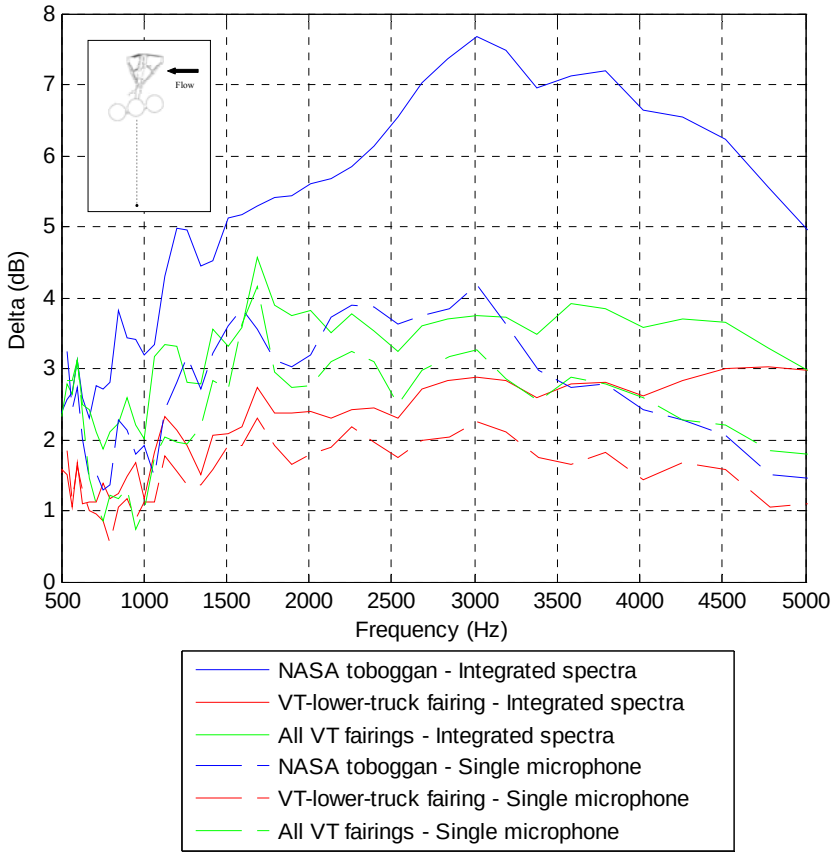

Figure 3.24: Noise reduction due to the NASA toboggan (blue curves), VT truck fairing (red curves), and all VT fairings (green curves) as estimated with integrated spectra (solid curves) and single far-field microphone measurements. Reduction was estimated from phased array (solid curves) and single microphone measurements straight under the gear in the far-field.

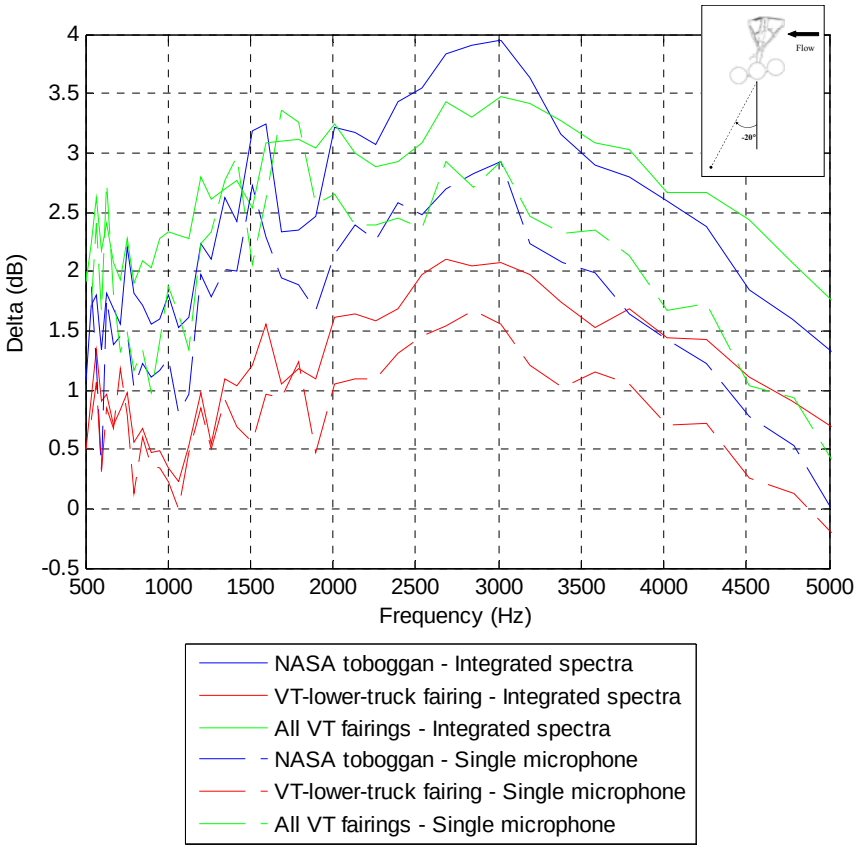

Figure 3.25: Noise reduction due to the NASA toboggan (blue curves), VT truck fairing (red curves), and all VT fairings (green curves) as estimated with integrated spectra (solid curves) and single far-field microphone measurements. Reduction was estimated from phased array (solid curves) and single microphone measurements on the rear arc.

4 CONCLUSIONS

Aeroacoustic measurements of the noise generated by a high-fidelity 26%-scale Boeing 777 main landing gear on the flyover path were performed in the VT semi-anechoic wind tunnel using a 63-element phased array and linear array of 15 microphones. Through this study, some limitations of aeroacoustic measurements of the landing gear noise in hard-walled wind tunnels were addressed.

First, data was collected in the near-field with the phased array, straight under the landing gear. In term of noise source location, the lower truck components such as front and rear brakes were the only noise sources identified. A comparison with near-field, hard-walled results showed that reducing the background noise levels leads to cleaner beamforming maps. By using the integrated spectra for the baseline landing gear, it was pointed out that in hard-walled test section the levels of the landing gear noise were overestimated.

Phased array measurements were also performed in the far-field. A comparison with near-field results showed that straight under the gear, the front and rear brakes, and the braces were shown to be the major noise sources. It was thus demonstrated that near-field, phased-array measurements of the landing gear noise straight under the gear are not suitable, i.e. they do not allow noise components located behind the truck to be identified. The array was also placed in the far-field, on the rear-arc of the landing gear. From this position, other noise sources such as the strut could be identified. This result demonstrated that noise from the landing gear on the flyover path cannot be characterized by only taking phased array measurement straight under the gear.

The noise reduction potential of three VT fairings and the NASA toboggan was estimated from far-field, phased-array and single-microphone measurements. With the phased array straight under the gear, the phased-array results indicated that the NASA toboggan was the most efficient noise control device. As noise generated by the truck was reduced, other noise sources located behind the truck such as the leading edge of the door and the braces could be identified more clearly. On the rear arc, the effectiveness of

the fairings was deteriorated. The NASA toboggan and the combination of all VT fairings achieved comparable noise reduction. It was shown that for both far-field, phased-array positions, the VT braces fairing reduced significantly the noise radiated from the braces. Further noise reduction could be achieved by combining the NASA-toboggan and the VT braces and strut fairings.

Finally, far-field phased-array (using integrated spectra) and single-microphone estimated noise reduction for the control devices were compared. Qualitatively, results were in good agreement. However, difference in levels was observed between the two approaches, in particular directly underneath the gear for the NASA toboggan. The reduction estimated from integrated spectra (phased-array) is always larger than from single microphone data. It was speculated that this difference was likely due to reflections of the landing gear noise on the hard wall of the semi-anechoic test section, flow effects, and background noise.

REFERENCES

[1] http://www.airliners.net

[2] H. H. Heller, and W. M. Dobrzynski, "Sound Radiation from Aircraft Wheel-Well/Landing-Gear Configurations," Journal of Aircraft, 14 (8), pp.768-774, 1977.

[3] H. Davy, and R. Remy, "Airframe Noise Characteristics on a 1/11 Scale Airbus Model," 4th AIAA/CEAS Aeroacoustics Conference, Toulouse, France, June 2-4, 1998. AIAA-1998-2335

[4] W. Dobrzynski, and H. Buchholz, "Full-Scale Noise Testing on Airbus Landing Gears in the German Dutch Wind Tunnel," 3rd AIAA/CEAS Aeroacoustics Conference, Atlanta, GA, May 1997. AIAA 97-1597-CP

[5] Lazos, B.,"Surface Topology on the Wheels of a Generic Four-Wheel Landing Gear," AIAA Journal, 40, 12, 2002, pp. 2402-2411

[6] P. M. Morse, and K. U. Ingard, Theoretical Acoustics, Princeton University Press, pp. 761-763, 1968.

[7] M. G. Macaraeg, "Fundamental Investigations of Airframe Noise," 4th CEAS/AIAA Aeroacoustics Conference, Toulouse, France, June 2-4, 1998. AIAA 98-2224

[8] P. T. Soderman, "Aeroacoustic Research Techniques – Jets to Autos," 3rd ASME/JSME Joint Fluids Engineering Conference, San Francisco, CA, July 1999. FEDSM99-7240

[9] E. Duell, J. Yen, S. Arnette, and J. Walter, "Recent Advances in Large Scale Aeroacoustic Wind Tunnels," 8th AIAA/CEAS Aeroacoustics Conference and Exhibit, Breckenridge, CO, June 17-19, 2002. AIAA-2002-2503

[10] J. A. Hayes, W. C. Horne, P. T. Soderman, and P. H. Bent, "Airframe Noise Characteristics of a 4.7% Scale DC-10 Model," 3rd AIAA/CEAS Aeroacoustics Conference, Atlanta, GA, 1997. AIAA 97-1594

[11] S. M. Jaeger, N. J. Burnside, P. T. Soderman, W. C. Horne, and K. D. James, "Microphone Array Assessment of an Isolated, 26%-Scale, High Fidelity Landing Gear," 8th AIAA/CEAS Aeroacoustics Conference and Exhibit, Breckenridge, CO, June 17-19, 2002. AIAA 2002-2410

[12] P. A. Ravetta, R. A. Burdisso, and W. F. Ng, "Wind Tunnel Aeroacoustic Measurements of a 26%-scale 777 Main Landing Gear Model", 10th AIAA/CEAS Aeroacoustics Conference and Exhibit, Manchester, United Kingdom, May 10-12, 2004. AIAA 2004-2885

[13] R. W. Stoker, and R. Sen, "An Experimental Investigation of Airframe Noise Using a Model-Scale Boeing 777," 39th AIAA Aerospace Sciences Meeting and Exhibit, Reno, NV, January, 2001. AIAA 2001-0987

[14] W. Dobrzynski, L. C. Chow, P. Guion, and D. Shiells, "A European Study on Landing Gear Airframe Noise Sources," 6th AIAA/CEAS Aeroacoustics Conference and Exhibit, Lahaina, HI, June 2000. AIAA 2000-1971

[15] W. Dobrzynski, L. C. Chow, P. Guion, and D. Shiells, "Research into Landing Gear Airframe Noise Reduction," 8th AIAA/CEAS Aeroacoustics Conference and Exhibit, Breckenridge, CO, June 17-19, 2002. AIAA 2002-2409

[16] Langley News, "Flight Tests Confirm New Technologies Can Help Quiet the Skies," http://www.nasa.gov, 2005

[17] W. H. Herkes, R. F. Olsen, and S. Uellenberg, "The Quiet Technology Demonstrator Program: Flight Validation of Airplane Noise-Reduction Concepts," 12th AIAA/CEAS Aeroacoustics Conference, Cambridge, MA, May 8 – 10, 2006. AIAA 2006-2720

[18] R. W. Stoker, Y. Guo, and C. Streett, "Airframe Noise Source Locations of a 777 Aircraft in Flight and Comparisons with Past Model Scale Tests," 9th AIAA/CEAS Aeroacoustics Conference and Exhibit, Hilton Head, SC, May 2003. AIAA 2003-3232

[19] W. C. Horne, K. D. James, T. K. Arledge, P. T. Soderman, N. J. Burnside, and S. M. Jaeger, "Measurements of 26%-scale 777 Airframe Noise in the NASA Ames 40- by 80 Foot Wind Tunnel," 11th AIAA/CEAS Aeroacoustics Conference and Exhibit, Monterey, CA, May 2005. AIAA 2005-2810

[20] N. J. Burnside, P. T. Soderman, W. C. Horne, and K. D. James, "Aeroacoustic Study of an Isolated, High-Fidelity, 26%-scale Landing Gear Model," November 2004. TP-2004-212815

[21] P. A. Ravetta, R. A. Burdisso, W. F. Ng, M. R. Khorrami, R. W. Stoker, and A. Abeysinghe, "Screening of Potential Landing Gear Noise Control Devices at Virginia Tech for QTD II Flight Test," 13th AIAA/CEAS conference, Rome, Italy, May 21-23, 2007

[22] Lazos, B. S., "Mean Flow Features Around the Inline Wheels of Four-Wheel Landing Gear," AIAA Journal, Volume 40, Issue 2, 2002, pp. 193–198

[23] F. O. Thomas, A. Kozlov, and T. C. Corke, "Plasma Actuators for Landing Gear Noise Reduction," 11th AIAA/CEAS Aeroacoustics Conference, Monterey, California, May 23-25, 2005. AIAA 2005-3010

[24] F. J. Souliez, L. N. Long, P. J. Morris, and A. Sharma, "Landing Gear Aerodynamic Noise Prediction Using Unstructured Grids," AIAA Aerospace Sciences Meeting and Exhibit, 40th, Reno, NV, January 14-17, 2002. AIAA-2002-799

[25] D. P. Lockard, "A Comparison of Ffowcs Williams-Hawkings Solvers for Airframe Noise Applications," 8th AIAA/CEAS Aeroacoustics Conference and Exhibit, Breckenridge, CO, June 17-19, 2002. AIAA-2002-2580

[26] D. P. Lockard, M R. Khorrami, and Fei Li, "Aeroacoustic Analysis of a Simplified Landing Gear," 9th AIAA/CEAS Aeroacoustics Conference and Exhibit, Hilton Head, SC, May 2003. AIAA 2003-3111

[27] E. F. Sheta, and A. Frendi, "Wavelet-Based Adaptive Multiresolution Methodology For Airframe Noise Prediction," 11th AIAA/CEAS Aeroacoustics Conference, Monterey, California, May 23-25, 2005. AIAA 2005-3056

[28] J. E. Ffowcs Williams, and D.L. Hawkings, "Sound generation by turbulence and surfaces in arbitrary motion," Philosophical Transactions for the Royal Society of London. Series A, Mathematical and Physical Sciences, Volume 264, Issue 1151, 1969, pp. 321-342

[29] M.G. Smith and L.C. Chow, "Validation of a Prediction model for Aerodynamic Noise from Aircraft Landing Gear," 8th AIAA/CEAS Aeroacoustics Conference and Exhibit, Breckenridge, CO, May 2002. AIAA 2002-2581

[30] Y. Guo, "A Statistical Model for Landing Gear Noise Prediction," 9th AIAA/CEAS Aeroacoustics Conference and Exhibit, Hilton Head, SC, May 2003. AIAA 2003-3227

[31] S. J. Pietrzko, and R. F. Hofmann, "Mathematical Modeling of Aircraft Noise Based on Identified Directivity Patterns," 2nd AIAA/CEAS Aeroacoustics Conference, State College, PA, May 1996. AIAA 96-1768

[32] S. M. Jaeger, and B. E. Smith, "Acoustic Measurements of a Model Semi-span Symmetry Plane," 2nd AIAA and CEAS Aeroacoustics Conference, State College, PA, May 6-8, 1996. AIAA 96-1715

[33] R. P. Dougherty, "Turbulent Decorrelation of Aeroacoustic Phased Arrays: Lessons from Atmospheric Science and Astronomy," 9th AIAA/CEAS Aeroacoustics Conference and Exhibit, Hilton Head, SC, May 2003. AIAA 2003-3200

[34] H. E. Camargo, R. A. Burdisso, "Noise Control of a Low Speed Wind Tunnel Fan," considered for publication in the proceedings of the INTER-NOISE 2006 conference, Honolulu, Hawai, December 3-6, 2006

[35] S. M. Jaeger, W. C. Horne, and C. S. Allen, "Effect of Surface Treatment on Array Microphone Self-Noise," 6th AIAA/CEAS Aeroacoustics Conference, Lahaina, HI, June 2000. AIAA 2000-1937

[36] http://sweetcomposites.com

[37] P. A. Ravetta, "LORE Approach for Phased Array Measurements and Noise Control of Landing Gears," Ph.D. dissertation, Virginia Polytechnic Institute and State University, 2005

[38] M. Mosher, M. E. Watts, S. Jovic, and S. M. Jaeger, "Calibration of Microphone Array for Phased Array Processing," 3rd AIAA/CEAS Aeroacoustics Conference, Atlanta, GA, May 12-14, 1997. AIAA 1997-1678

[39] M. C. Remillieux, R. A. Burdisso, and W. F. Ng, "Noise Source Location and Control of a 26%-Scale High-Fidelity Boeing 777 Main Landing Gear in a Semi-Anechoic-Wind-Tunnel Test Section" NASA technical report, April 2007

[40] P. T. Soderman and C. S. Allen, "Microphone Measurements In and Out of Airstream" in Aeroacoustic Measurements, Ed. T. J. Mueller, Springer Verlarg, Berlin, 2002

[41] R. P. Dougherty, "Beamforming in Acoustic Testing," in Aeroacoustic Measurements, Ed. T. J. Mueller, Springer Verlarg, Berlin, 2002

[42] G. B. Whitham, Linear and Nonlinear Waves, Wiley, New York, 1974

[43] M. Mosher, "Low Frequency Rotational Noise in Closed-Test-Section Wind Tunnels'," Journal of the American Helicopter Society, 1991

[44] R. K. Amiet, "Correction of Open Jet Wind Tunnel Measurements for Shear Layer Refraction," 2nd AIAA Aeroacoustics Conference, Hampton, VA, March 24-26, 1975. AIAA 75-532

[45] R. K. Amiet, "Refraction of sound by a shear layer," 15th Aerospace Sciences Meeting, Los Angeles, CA, January 24-26, 1977. AIAA-1977-54

[46] R. H. Schlinker and R. K. Amiet, "Refraction of Sound by a Shear Layer – Experimental Assessment," 5th Aeroacoustics Conference, Seattle, WA., March 12-14, 1979. AIAA-1979-628

[47] S. M. Candel, "Application of Geometrical Techniques to Aeroacoutic Problems," 3rd Aeroacoustics Conference, Palo Alto, CA, July 20-23, 1976. AIAA 76-546

[48] A. D. Pierce, Acoustics, An Introduction to its Physical Principles and Applications, Acoustical Society of America, Woodbury, NY, 1989

[49] H. S. Ribner, “Reflection, Transmission and Amplification of Sound by a Moving Medum,” Journal of the Acoustical Society of America, 1957

APPENDIX A: THEORETICAL DEVELOPMENT

A microphone phased array was primarily utilized in this study to locate the noise sources of the landing gear. The acoustic data collected with the array was post-processed in the frequency domain with a beamforming algorithm that accounts for flow effects. To describe this algorithm, the conventional beamforming process, which does not account for flow effects, is derived first. Subsequently, the Green's functions used to modify the conventional beamforming code are determined.

A.1 Conventional beamforming

Following Dougherty [40], the conventional beamforming process is derived. First, let us consider a single monopole source and an N-element microphone phased array. The process starts with simultaneous time series measurements of the pressure, $\chi_n(t)$, at each of the N microphones of the array. Since a frequency domain analysis is conducted, the time series are partitioned into time blocks and a FFT over each finite time intervals and each microphone is performed. The pressure of each microphone in the frequency domain is defined as,

$$p_n(f) = \frac{2}{T}\int_0^T \Psi(t)\chi_n(t)e^{-2\pi i f t}\,dt, \tag{A.1}$$

where f is the frequency and $\Psi(t)$ is an optimal "window" function.

The microphone auto-spectra and cross-spectra, denoted as $C_{nn}(f)$ and $C_{mn}(f)$, respectively, are then computed,

$$C_{nn}(f) = \frac{1}{2}\left\langle p_n(f)p_n^*(f)\right\rangle, \tag{A.2}$$

$$C_{mn}(f) = \frac{1}{2}\left\langle p_m(f)p_n^*(f)\right\rangle, \tag{A.3}$$

where * is referred to as the complex conjugate and <…> as the average over the number of time blocks. The above quantities are rearranged in vector form, so that,

$$\mathbf{p} = \begin{Bmatrix} p_1(f) \\ \vdots \\ p_N(f) \end{Bmatrix}, \tag{A.4}$$

and,

$$\mathbf{C} = \frac{1}{2}\left\langle \mathbf{p}\mathbf{p}^* \right\rangle, \tag{A.5}$$

where * is referred to as the Hermitian. It was shown that the diagonal elements of the cross spectral matrix (C_{nn}) contain the microphones self-noise [41]. Including these terms in the beamforming process does not contribute to resolution and can be detrimental by introducing the microphones self-noise. Therefore, in the beamforming code used in this study, the diagonal of the cross spectral matrix, C_{nn}, was neglected, i.e. diagonal removal technique [41].

The beamforming output may be written symbolically as,

$$b = \mathbf{w}^* \mathbf{C} \mathbf{w}, \tag{A.6}$$

where **w** is an N-dimensional vector, referred to as the weight vector, that is dependent on an assumed source model at a point in space, e.g. monopole at a grid point, and b is the resulting power for that source direction. The weight vector is such that unit gain is found for unit sources in the assumed direction,

$$\mathbf{w}^* \mathbf{g} = 1, \tag{A.7}$$

where **g** is the steering vector, consisting of microphone pressure amplitudes, induced by a unit source. Since the source is a monopole, in a medium at rest, **g** has the form,

$$g_n = \frac{-1}{4\pi R_n} e^{-ikR_n}, \tag{A.8}$$

where R_n is the distance between the source and the n^{th} microphone, and k is the free-field wavenumber associated with the frequency f.

Now consider there are multiple sources to be located. A scanning grid of K points containing the potential noise sources is defined. In the beamforming process, it is assumed that each point of the grid is a monopole source and that the sources associated

with distinct points are uncorrelated. The resulting pressure measured by the microphones becomes,

$$\mathbf{p} = \sum_{k=1}^{K} \mathbf{p}_k \ . \tag{A.9}$$

The cross spectral matrix becomes,

$$\mathbf{C} = \frac{1}{2}\left\langle \left(\sum_{k=1}^{K} \mathbf{p}_k \right) \left(\sum_{k=1}^{K} \mathbf{p}_k \right)^* \right\rangle = \frac{1}{2} \sum_{k=1}^{K} \sum_{l=1}^{K} \left\langle \mathbf{p}_k \mathbf{p}_l^* \right\rangle . \tag{A.10}$$

Therefore, equation (A.6) can be written as,

$$\mathbf{b} = \frac{1}{2} \sum_{k=1}^{K} \sum_{l=1}^{K} \mathbf{w}^* \left\langle \mathbf{p}_k \mathbf{p}_l^* \right\rangle \mathbf{w} \ . \tag{A.11}$$

Since it is assumed that the grid points are uncorrelated, the cross-product $\mathbf{p}_k \mathbf{p}_l^*$ have random phase and will disappear by averaging. In the limit, the single summation remains, and the beamforming output may be written as,

$$\mathbf{b} = \frac{1}{2} \sum_{k=1}^{K} \mathbf{w}^* \left\langle \mathbf{p}_k \mathbf{p}_k^* \right\rangle \mathbf{w} \ . \tag{A.12}$$

A.2 Determination of Green's functions for aeroacoustic measurement of a source in a moving medium

In the beamforming process presented earlier on, it is assumed that between the source and the receiver the medium is at rest, which is not the case in the herein study. This section presents theoretical elements of aeroacoustics to account for flow effects in the beamforming process.

A.2.1 Monopole source and receiver in a uniform flow

Let us consider a monopole source and a receiver in a uniform flow moving parallel to the x direction and with a Mach number M, as depicted in Figure A.1. In the figure, S, R, and E denote the positions of the source, microphone and moving center of the wave-front, respectively. A wave-front is defined as a surface of points having the same phase. If the ambient medium is moving with velocity **v**, the wave velocity c**n** seen by someone moving with the fluid becomes c**n**+**v**. Here **n** is the unit vector normal to the wave-front;

it coincides with the direction of propagation if the coordinate system is moving with the local ambient fluid velocity **v**. However, the direction of propagation perceived by a stationary observer is not necessarily the same as that of **n**. In the figure, E can be seen as the moving center with speed **v** of a wavefront propagating with speed c**n**. The center of the wave-front is shifted along the direction given by **v** for a duration equal to the travel time, τ, or by a distance equal to Mcτ. The distance between the source and the receiver is denoted by *r*.

The situation described here is, for example, the case of a model tested in a hard-walled wind tunnel with a microphone phased array flush mounted on a wall of the test section. The problem is studied in the context of geometrical acoustics, following Whitham [42].

In a moving medium with speed $\mathbf{v} = v_x\mathbf{e}_\mathbf{x}$, the acoustic pressure obeys the convected wave equation

$$\nabla^2 p - \frac{1}{c^2}\left(\frac{\partial}{\partial t} + v_x\frac{\partial}{\partial x}\right)^2 p = 0, \tag{A.13}$$

One seeks a high-frequency asymptotic expansion of the form,

$$p(\mathbf{x},t) \sim e^{-i\omega(t-\tau(\mathbf{x}))}\sum_0^\infty \phi_n(\mathbf{x})(-i\omega)^{-n}, \tag{A.14}$$

where τ is the travel time, i.e. time for the wave to travel from the moving center of the wave-front to the receiver. The first term of the expansion is found by replacing equation (A.13) into (A.14) to yield

$$p_0 = \frac{e^{-i\omega(t-\tau)}}{4\pi c\tau}, \tag{A.15}$$

which is solution to,

$$2M\left(\frac{1}{c} - M\frac{\partial\tau}{\partial x}\right)\frac{\partial\phi_0}{\partial x} + 2(\nabla\tau)\cdot(\nabla\phi_0) = \left(M^2\frac{\partial^2\tau}{\partial x^2} - (\nabla\tau)\cdot(\nabla\tau)\right)\phi_0, \tag{A.16}$$

To have complete knowledge of p_0, the travel time τ must be determined. The triangle RSE and the law of sines yield

$$(c\tau)^2 = (r_r\sin\theta_r)^2 + (r_r\cos\theta_r + Mc\tau)^2 \tag{A.17}$$

Rearranging terms and solving the second order equation for $\left(\frac{c\tau}{r_r}\right)$ yields

$$\tau = r_r\left[\frac{M\cos\theta_r + \sqrt{1-M^2\sin^2\theta_r}}{c\left(1-M^2\right)}\right], \tag{A.18}$$

or,

$$\tau = \frac{1}{c}\frac{R-Mx}{1-M^2}, \tag{A.19}$$

where $R = \sqrt{x^2 + \left(y^2+z^2\right)\left(1-M^2\right)}$.

The geometrical approach used here is very convenient for this type of problems because it provides a very intuitive description of the propagation phenomena. However, it also includes some limitations since it is restricted to high frequency sound propagation, cf. equation (A.14).

Mosher [42] proposed an exact solution to the convected wave equation by replacing $c\tau$ by R in the denominator of p_0. The Green's function is then written as,

$$p = \frac{e^{-i\omega(t-\tau)}}{4\pi R}. \tag{A.20}$$

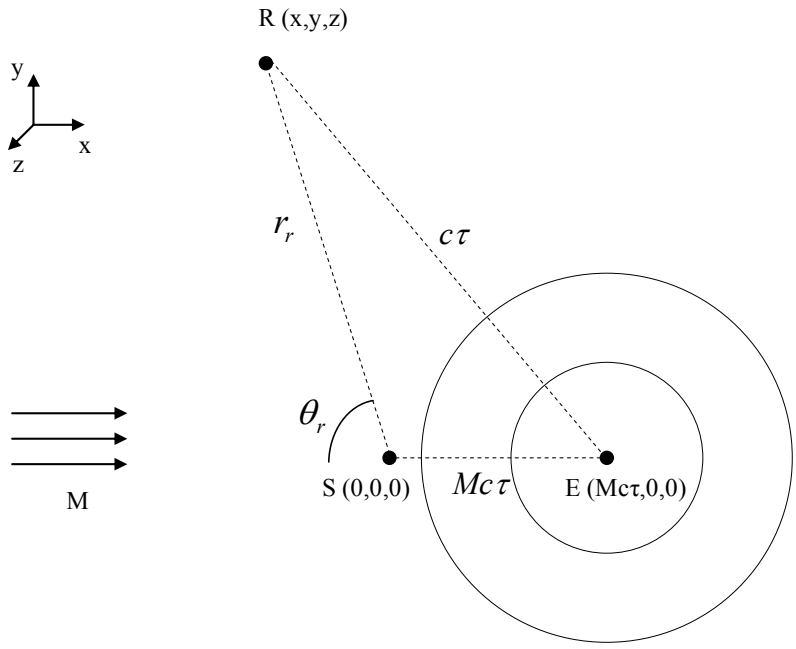

Figure A.1: Sound wave propagation in a uniform flow.

Ravetta et al. [12] used a classical beamforming algorithm to locate noise sources. In this case the green's function is defined as,

$$p = \frac{e^{-i\omega(t-r/c)}}{4\pi r}, \tag{A.21}$$

where r is the distance from the source to the receiver. From the reasoning outlined above, this results in seeing the source at E instead of S. In other words, when conventional beamforming is used, the source will be located at the position of the moving center, E, of the wave-front. To overcome this problem, in reference [12] the beamforming maps were shifted by a distance d. This distance was determined experimentally by placing a point source in the wind tunnel at (0,h,0), where h is the distance between the center of the array and the source and (0,0,0) is the center of the phased array, and by using a conventional beamforming code to locate the position of the apparent source (d,h,0). From equation (A.19), d is also,

$$d = M\frac{h}{\sqrt{1-M^2}}. \tag{A.22}$$

It was shown earlier that τ varies with (x,y,z). Thus, considering d constant over the plane y = h introduces errors in the beamforming map as we move away from the point with coordinates (0,h,0). The non-normalized error is defined as Mcτ-d and is plotted in Figure A.2 as a function of x and z. The error was plotted for -0.5 < x < 0.5 and -0.5 < z < 0.5. The error is 0 at the point where the shift was computed, i.e. point of coordinates (0,h,0), and reaches a maximum of 5.6 cm at (-0.5,h,-0.5) and (-0.5,h,0.5). Note that the error is larger downstream than upstream the point (0,h,0). For example at (-0.5,h,0.5) and (0.5,h,0.5) the error is 5.6 and 3.7 cm, respectively.

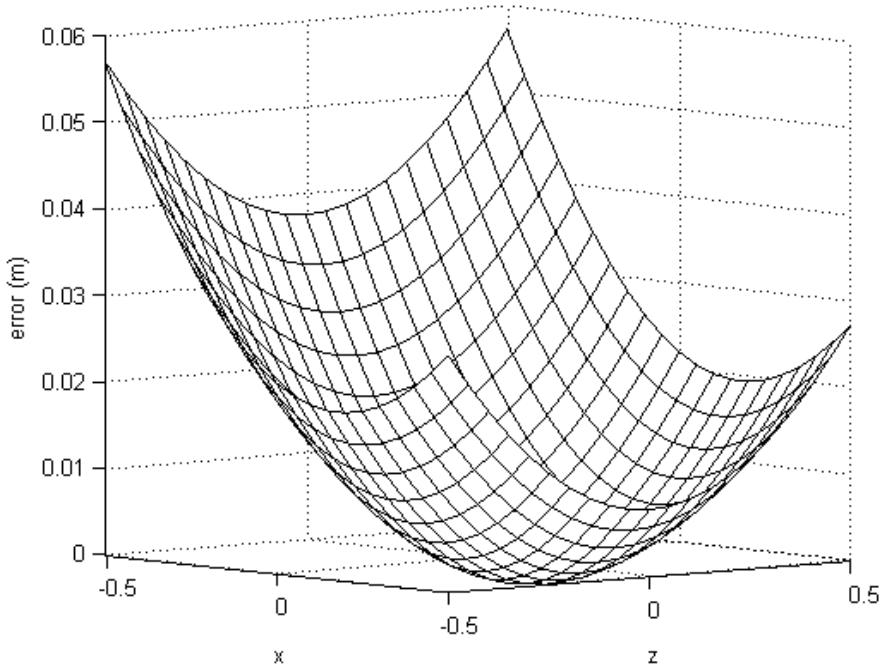

Figure A.2: The non-normalized error in source location over a plane -0.5 < x < 0.5, -0.5 < z < 0.5, h = 0.92 m, when the beamforming map is shifted by a constant $d = M\,h/\sqrt{1-M^2}$, at M = 0.17.

A.2.2 Monopole source in a uniform flow and receiver in a region at rest

Now consider the case of a monopole source in a uniform flow in the x-direction and Mach number M, and a receiver in a region at rest. Commonly, this is the case of a model tested in open-jet wind tunnel. As the sound generated by the model propagates to the sensor located outside the flow, it passes through the jet shear layer, i.e. a velocity discontinuity. The propagating sound wave is then refracted and possibly scattered.

Besides, as we move downstream the jet, the shear layer thickness increases. A considerable amount of work has been devoted to this non-trivial problem. Early work focused on determining angle and amplitude corrections to apply to acoustic measurements in the presence of a shear layer. Amiet [43,44] replaced the free jet shear layer with a vortex-sheet for his correction procedure. In this section, amplitude corrections are not computed since a calibration for the array levels was performed, cf. Appendix B. Amiet's analysis also indicated that the effects of the shear layer thickness were not significant at low Mach numbers. This was later confirmed experimentally by Schlinker et al. [45]. They also showed that scattering of sound due to the turbulence of the shear layer was not important for low mach numbers and frequencies lower than 5 kHz.

Our experiments differ from the open-jet-wind-tunnel case by the nature of the transition region separating the model from the microphone phased array, i.e. a boundary layer on the Kevlar surface. Following Amiet [44,45], the boundary layer may be replaced by a 0-thickness layer. The interface separating the test section from the anechoic chamber is a plane.

Our objective is to determine a Green's function for this particular problem. The solution may be carried out in the context of geometrical acoustics with the limitations it includes. The Green's function may be approximated by the first term of the high frequency asymptotic expansion written in equation (A.15). To determine the travel time from a point of the scanning grid to a microphone of the phased array, the numerical ray tracing technique developed by Candel [46] and summarized by Pierce [47] is followed here. This technique has the advantage to handle the three-dimensional case very well, i.e. when the source and the receiver are not in a plane normal to the 0-thickness layer.

Before presenting the implementation of the numerical approach, the refraction of an acoustic ray through a flow velocity discontinuity in the two-dimensional case is described in Figure A.3. A ray is emitted from the source with an angle θ_1 with respect to the x-axis. However, due to the flow velocity, the ray propagates from the source to the

boundary layer with an angle θ_c. This is equivalent to say that the ray propagates with an angle θ_1 from the moving center, E, of the wavefronts propagating at speed c**n**. The wave-front intersects the boundary layer at C and its tangent at this point is α or $\pi/2-\theta_1$. Although the boundary layer is depicted with finite thickness in the schematic, it is considered as a 0-thickness layer in this analysis. In the medium at rest, the ray is propagating with an angle θ with respect to the x-axis. The relation between α and θ is obtained by equating the x components of phase velocity across the flow velocity discontinuity. As for the case of a plane wave incident on the discontinuity discussed by Ribner [48]

$$\frac{1}{\sin(\alpha)}+M=\frac{1}{\cos(\theta)}. \tag{A.23}$$

If one is able to find the emission angle θ_1 for which the direction θ will coincide with the direction given by the line CR, then the travel time of the ray SCR can be computed. For the 3-dimensional case, the emission direction is defined by 2 angles. The 2-dimensional analysis can easily be extended to three dimensions by seeking a set of emission angles $\{\theta_1,\theta_2\}$ for which the ray path intersect the position of the receiver R.

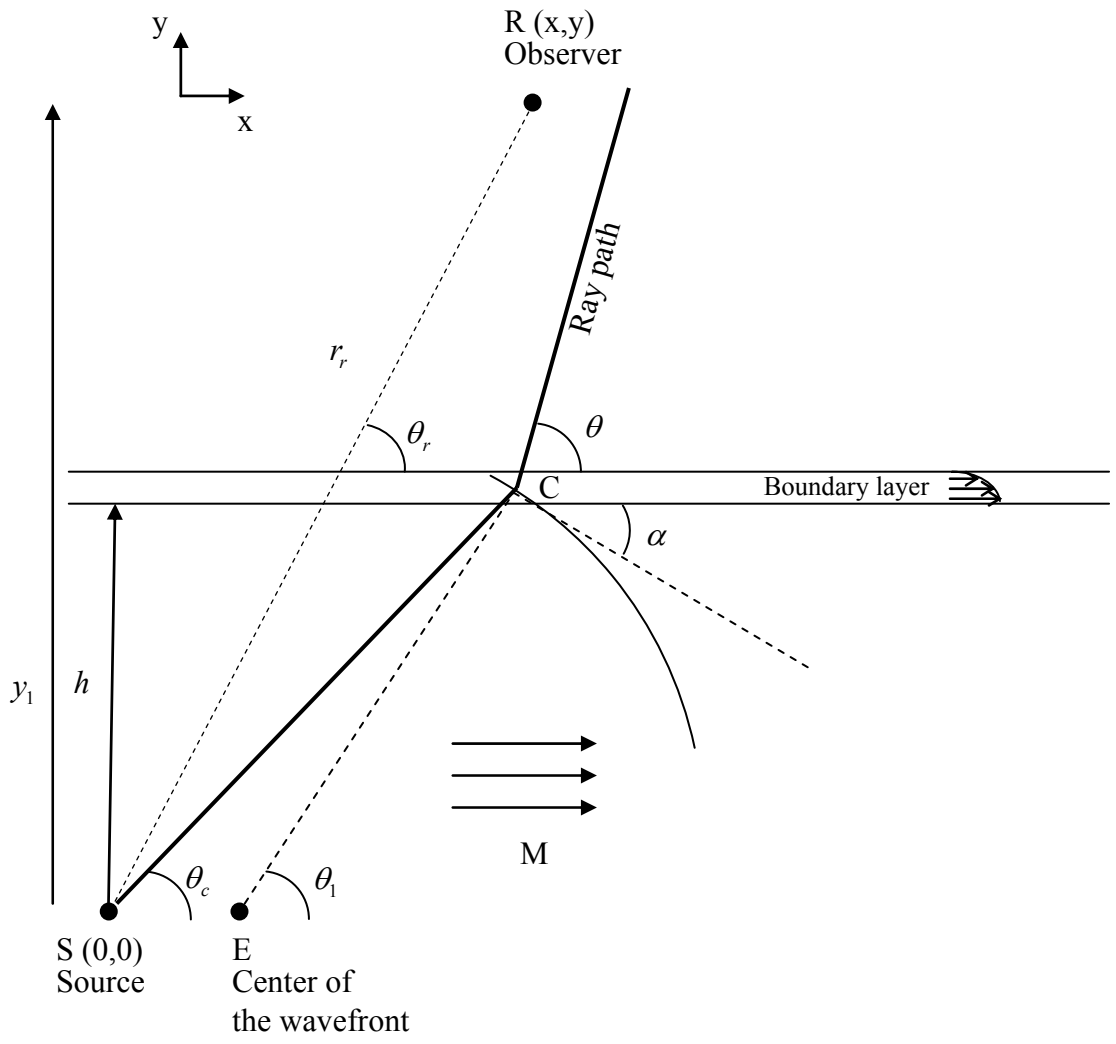

Figure A.3: Sound wave propagation through a boundary layer using ray acoustics.

In the following, the implementation of the numerical approach to determine the travel time from S to R is presented. The ray path, denoted $\mathbf{x}_p(t)$, is a point that lies on the wave-front $t = \tau(x)$. The velocity of the ray path is

$$\mathbf{v}_{ray} = \frac{d\mathbf{x}_p}{dt} = \mathbf{v}\left(\mathbf{x}_p, t\right) + \mathbf{n}\left(\mathbf{x}_p, t\right)c\,, \tag{A.24}$$

Where, for this problem, the fluid velocity is defined as,

$$\begin{cases} \mathbf{v}(y < h, t) = Mc\mathbf{e}_x \\ \mathbf{v}(y > h, t) = 0 \end{cases}. \tag{A.25}$$

Another differential equation is used to obtain the time rate of change of **n**. Instead of using **n** directly, the wave-slowness vector **s** is defined,

$$\mathbf{s}(\mathbf{x}) = \nabla\tau(\mathbf{x}_p), \tag{A.26}$$

which is parallel to **n** since $\nabla\tau(\mathbf{x}_p)$ is perpendicular to the surface $t = \tau(\mathbf{x}_p)$. The eikonal equation provides the length of **s**,

$$s^2 = \frac{\Omega^2}{c^2}, \tag{A.27}$$

where $\Omega = 1 - \mathbf{v}\cdot\mathbf{s}$. Considering c constant in both media and **v** = v_x $\mathbf{e}_x$, where v_x is constant, in the flow area. Equation (A.24), written in Cartesian coordinates, is,

$$\frac{dx_{pi}}{dt} = v_i + \frac{c^2 s_i}{\Omega}, \tag{A.28}$$

and the time rate of change of **s** is,

$$\frac{ds_i}{dt} = -\frac{\Omega}{c}\frac{\partial c}{\partial x_i} - \sum_{j=1}^{3} s_j \frac{\partial}{\partial x_i} v_j = 0. \tag{A.29}$$

The ray path, $\mathbf{x}_p(t)$, may be determined by integrating equations (A.28) and (A.29). From equation (A.29) it may be inferred that s_i is constant. The initial slowness vector is specified with direction $\{\theta_1, \theta_2\}$ and length s. The direction specified is a guess and the values of θ_1 and θ_2 need to be adjusted until the ray intersects the receiver position. Since the source is in the flow, using equation (A.27), |**s** (t = 0)| is,

$$s(t=0) = \frac{1}{c + v_x \cos(\theta_1)\cos(\theta_2)}, \tag{A.30}$$

where θ_1 and θ_2 are the angles between the projection of the slowness vector in the plane z = 0 and the x-axis, and between the slowness vector and the z-axis, respectively, as depicted in Figure A.4.

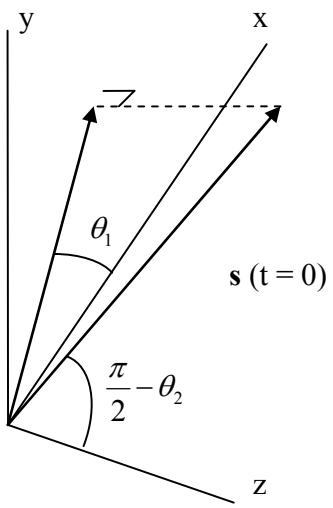

Figure A.4: Orientation of the initial slowness vector.

As aforementioned, **s** is a constant. Projecting equation (A.30) on the x, y, and z axes yields,

$$\begin{cases} s_1 = \cos(\theta_1)\cos(\theta_2)/(c + v_x \cos(\theta_1)\cos(\theta_2)) \\ s_2 = \sin(\theta_1)\cos(\theta_2)/(c + v_x \cos(\theta_1)\cos(\theta_2)) \\ s_3 = \sin(\theta_2)/(c + v_x \cos(\theta_1)\cos(\theta_2)) \end{cases}. \tag{A.31}$$

The position vector in the flow region, $\mathbf{x}_p^f$, and the position vector in the no-flow region, $\mathbf{x}_p^{nf}$, are obtained by integrating equation (A.28),

$$\begin{cases} x_{p1}^f = \left(c^2 s_1/(1 - v_x s_1) + v_x\right)t + x_s \\ x_{p2}^f = \left(c^2 s_2/(1 - v_x s_1)\right)t + y_s \\ x_{p3}^f = \left(c^2 s_3/(1 - v_x s_1)\right)t + z_s \end{cases}, \tag{A.32}$$

$$\begin{cases} x_{p1}^{nf} = c^2 s_1 t + b_1 \\ x_{p2}^{nf} = c^2 s_2 t + b_2 \\ x_{p3}^{nf} = c^2 s_3 t + b_3 \end{cases}, \tag{A.33}$$

where x_s, y_s, and z_s are the coordinates of the source and b_1, b_2, and b_3 are constant of integrations. For convenience, x_s, y_s, and z_s are chosen to be the origin of the coordinate system, i.e. $x_s = 0$, $y_s = 0$, and $z_s = 0$. The b_i's are determined by the following relation,

$$x_{pi}^{nf}(t = 0) = b_i = x_{pi}^f(t = t_{sw}), \tag{A.34}$$

where t_{sw} is the time for the ray to travel from the source to the velocity discontinuity. For the particular problem studied here, t_{sw} is,

$$t_{sw} = x_{p2}^{f}\left(1 - v_x s_1\right) / \left(c^2 s_2\right). \tag{A.35}$$

Using the constraint, $\left(x_{p1}^{nf}\right)^2 + \left(x_{p2}^{nf}\right)^2 + \left(x_{p3}^{nf}\right)^2 = r^2$, where r is the distance between the source and the receiver, the travel time, t_{wr}, from the velocity discontinuity to the source may be computed and is given by the following expression in index notation,

$$t_{wr} = \left[-2\left(a_i b_i\right) + \sqrt{\left(a_i b_i\right)^2 - 4 a_i a_i \left(b_j b_j - r^2\right)} \right] \Big/ \left(2 a_i a_i\right), \tag{A.36}$$

where $a_i = \left(c^2 s_i\right)$ and $b_i = \left(\left(c^2 s_i\right) / \left(1 - v_x s_1\right) + v_x \delta_{1i}\right) t_{sw}$. The total travel time t_t is,

$$t_t = t_{sw} + t_{wr}. \tag{A.37}$$

Note that this iterative procedure has to be repeated for each point of the beamforming grid and each microphone of the phased array. As a result, the modified beamforming algorithm will determine the location of the noise sources while accounting for convection and refraction effects, at the expense of a larger computing time.

A two dimensional case was implemented in MATLAB with M = 0.17, the source located at (0,0,0), the receiver at (0.5,2,0) and the 0-thickness boundary layer at y = 0.92 m. The travel time was found to be 6.1 ms. The same case was run but this time included a finite-thickness boundary layer with thickness δ = 0.12 m and a velocity profile quadratic in y. The travel time was found to be 6 ms, or 1.6% lower than the 0-thickness-boundary-layer case. This confirms the fact that the boundary-layer thickness is not a significant parameter of the travel-time calculation. Figures A.5a and b depict the ray path for the 2 cases.

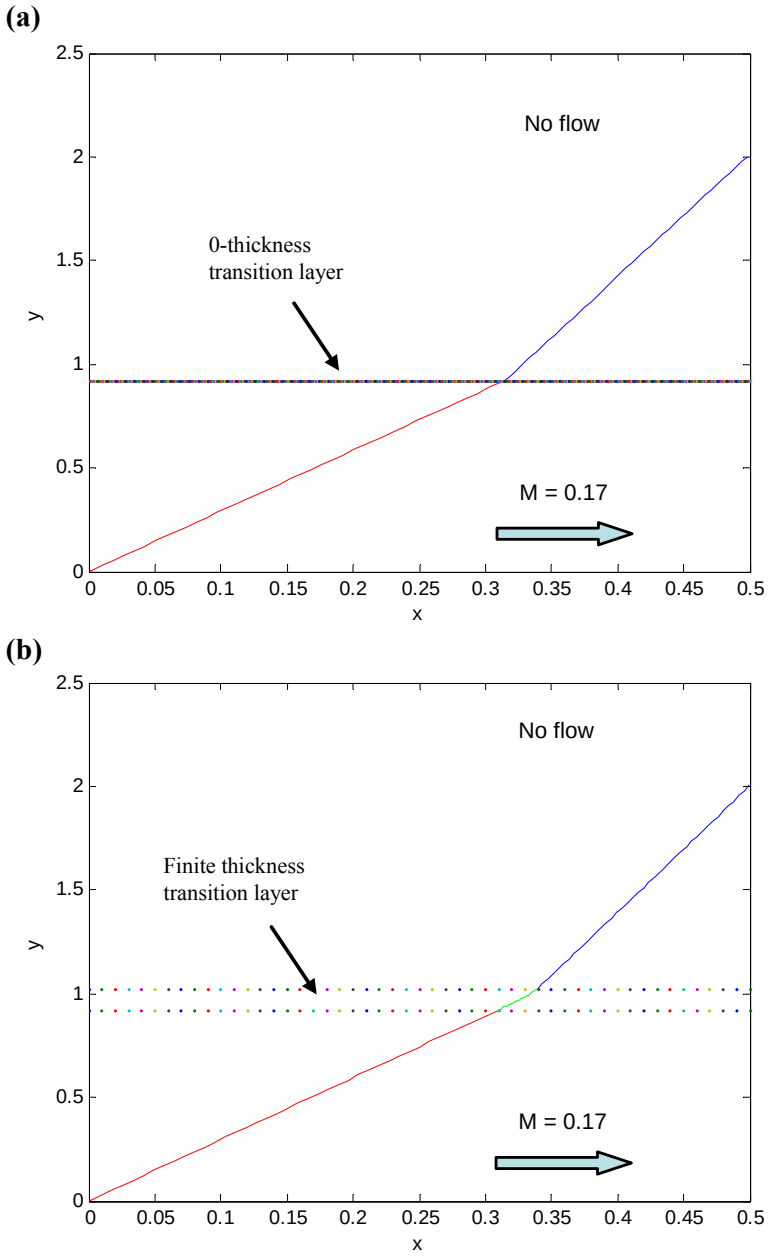

Figure A.5: Ray path from a source located at (0,0,0) to a receiver located at (0.5,2,0) in the case of a 0-thickness transition layer (a), and a 0.12 m thick boundary layer (b). The red, green and blue lines represent the ray paths in the flow region, boundary layer and no flow region, respectively.

APPENDIX B: PRELIMINARY TESTS

In this section, results from preliminary tests are reported. First, the analysis on sound propagation through a flow velocity discontinuity, described in Appendix A.2.2, is validated experimentally. Ultimately, a detailed description of the calibration procedure for the array levels is given.

B.1 Experimental validation of Green's function formulation for sound propagation through a velocity discontinuity

In Appendix A.2.2, the Green's function for propagation of sound waves through a velocity discontinuity was formulated. The approach was based on the calculation of the travel time of a sound wave propagating from a monopole source in flow to a receiver in a medium at rest. To validate the analytical formulation of the Green's function the following approach is followed. First, the distance between the actual source and the center of the moving wave-front is computed analytically. This distance, which will be referred to as "shift" in the rest of this appendix, may be expressed as the product of the flow speed and the travel time of the acoustic wave from the source to the velocity discontinuity. In this section, the shift was determined experimentally using a calibrated point source and the 63-element microphone phased array. Acoustic data was post-processed with conventional beamforming, which resulted in locating the center of the moving wave-front. The distance between the actual and apparent source is measured to provide the experimental value of the shift.

Figure B.1 is a description of the experimental setup. Sound was generated by a 60 W compression driver from P.Audio (model D440) with 1 inch throat and frequency range [1.5 - 18 kHz]. A 70 inch-long aluminum pipe with an inner diameter of 1/2 inch, referred to as the "speaker pipe", was connected to the speaker via a circular aluminum plate. The "speaker pipe" was allowed to slide inside an aluminum pipe with larger diameter that was bolted to the hard wall of the test section via a circular aluminum plate. The opening in the hard wall was sealed with a 1/4-inch-thick honeycomb panel. Although the "speaker-pipe" source could be bolted to the panel at nine different

locations, five positions, labeled from 1 to 5, were tested. Since the speaker pipe was allowed to slide inside the supporting pipe, the position of the source could be adjusted along the z-direction inside the test section. The source was tested at 15 different locations in the test section, represented by numbered black dots. In order to minimize the deflection and vibration of the source against the air flowing in the test section, for positions 8 and 13 of the source, strings connected the tip of the source to the hard wall of the test section.

The 63-element phased array was located in the anechoic chamber at 3 different locations corresponding to the positions used to locate noise sources in the landing gear. A detailed description of these positions may be found in Section 2.3. Tests were conducted at the speeds, M = 0, 0.12, 0.15 and 0.17, that correspond to the speeds of the landing gear testing.

The objective was to test 15 source positions for each of the 3 array positions at all flow speeds, i.e. 180 tests. However, due to time constraints about half of the test matrix could be completed. The configurations that could be completed during the test entry are listed in Table B.1.

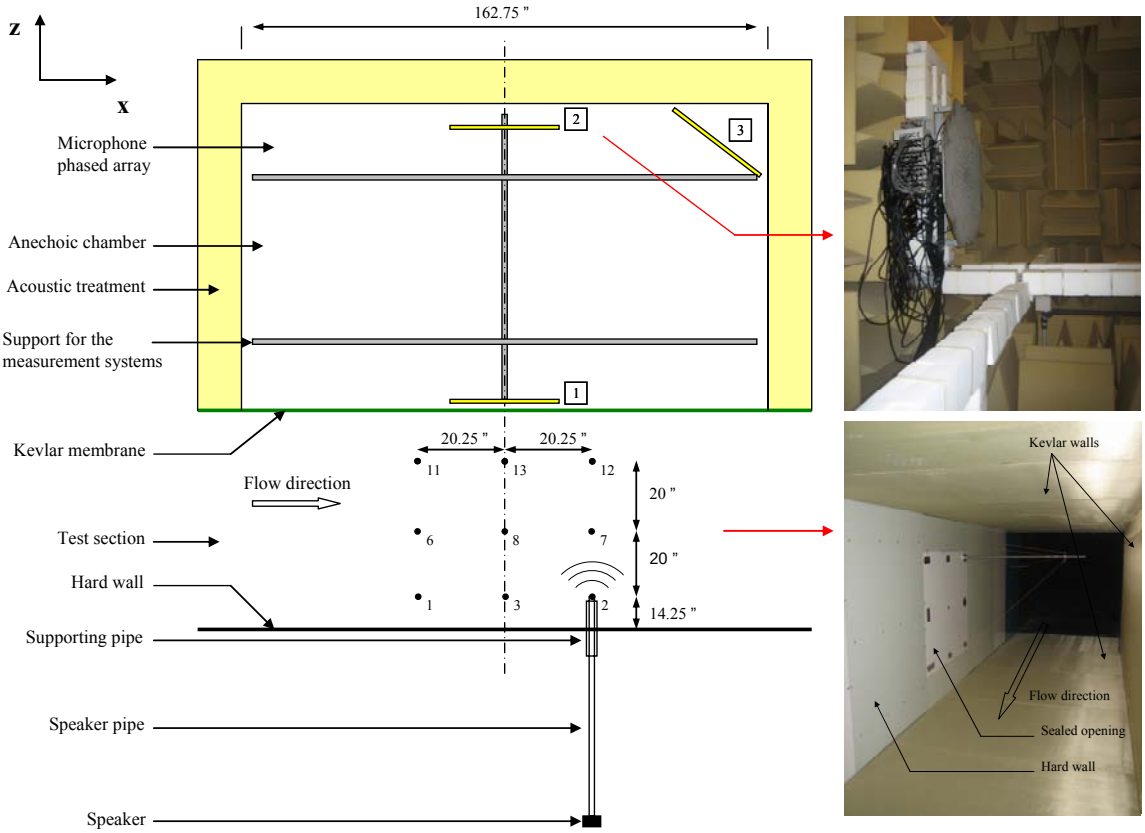

Figure B.1: The experimental setup for noise location of a point source in the wind-tunnel test section.

Table B.1: The various configurations of the experimental setup.

source position	array position	Mach number		source position	array position	Mach number
1	2	0		1	3	0
3	2	0		2	3	0
5	2	0		3	3	0
6	2	0		4	3	0
8	2	0		5	3	0
10	2	0		6	3	0
11	2	0		7	3	0
13	2	0		8	3	0
15	2	0		9	3	0
1	2	0.12		10	3	0
3	2	0.12		11	3	0
5	2	0.12		12	3	0
6	2	0.12		13	3	0
8	2	0.12		14	3	0
10	2	0.12		15	3	0
11	2	0.12		1	3	0.12
13	2	0.12		2	3	0.12
15	2	0.12		3	3	0.12
1	2	0.15		4	3	0.12
3	2	0.15		5	3	0.12
5	2	0.15		6	3	0.12
6	2	0.15		7	3	0.12
8	2	0.15		8	3	0.12
10	2	0.15		9	3	0.12
11	2	0.15		10	3	0.12
13	2	0.15		11	3	0.12
15	2	0.15		12	3	0.12
1	2	0.17		13	3	0.12
3	2	0.17		14	3	0.12
5	2	0.17		15	3	0.12
6	2	0.17		1	3	0.15
8	2	0.17		2	3	0.15
10	2	0.17		3	3	0.15
11	2	0.17		4	3	0.15
13	2	0.17		5	3	0.15
15	2	0.17		6	3	0.15
				7	3	0.15
				8	3	0.15
				9	3	0.15
				10	3	0.15
				11	3	0.15
				12	3	0.15
				13	3	0.15
				14	3	0.15
				15	3	0.15
				1	3	0.17
				2	3	0.17
				3	3	0.17
				4	3	0.17
				5	3	0.17
				6	3	0.17
				7	3	0.17
				8	3	0.17
				9	3	0.17
				10	3	0.17
				11	3	0.17
				12	3	0.17
				13	3	0.17
				14	3	0.17
				15	3	0.17

Figures B.2a through d show the beamforming maps of the "speaker-pipe" source in position 8 with the microphone phased array in position 2. The beamforming maps were obtained by using a conventional beamforming code. Noise levels are of secondary importance in this analysis. Therefore, the maps presented are not calibrated for levels. The vertical dashed lines indicate the abscissa of the apparent source as located with conventional beamforming. The shift is measured from the graphs and compared to the shift computed with the approach presented in Appendix A.2.2. Results for this particular case are summarized in table B.2. The error in source position is less than 3% for the 3 cases shown. Similar results were obtained for other source positions. Analytical and experimental results are thus in very good agreement.

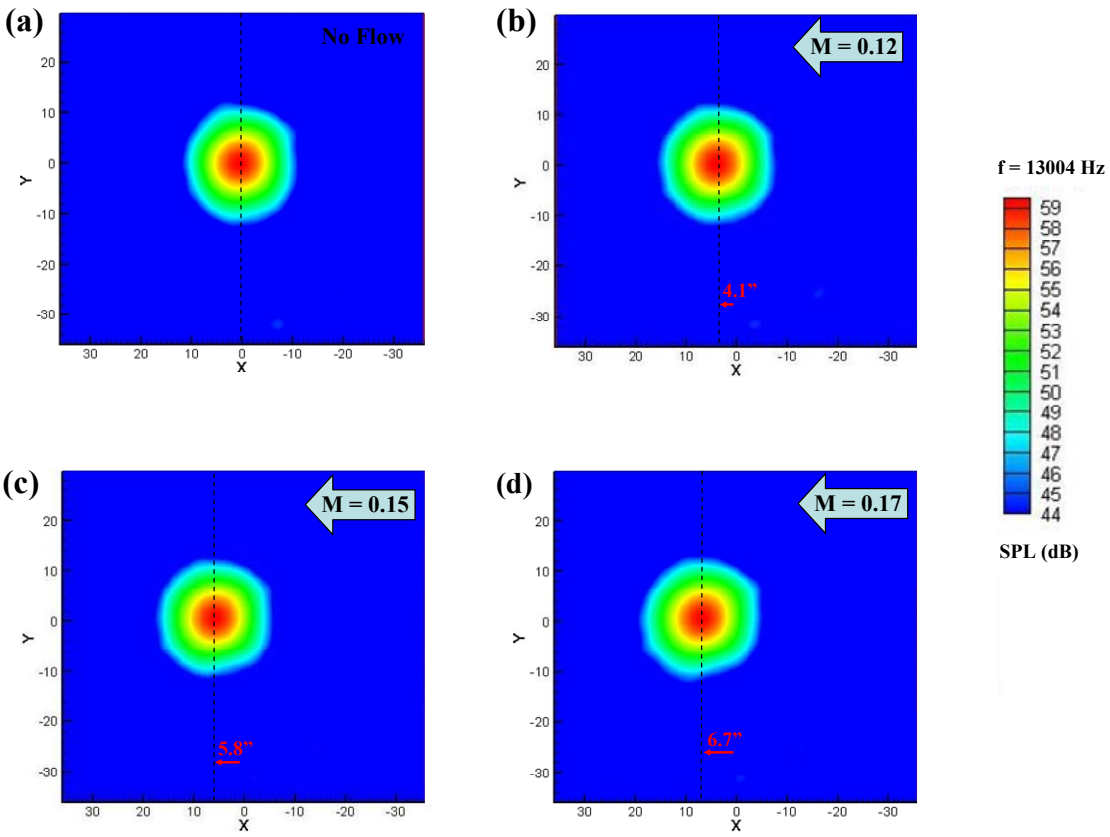

Figure B.2: Beamforming maps of the point source in position 8 at f = 13004 Hz as obtained with a conventional beamforming code. Data was collected with the microphone phased array in position 2 at speeds, (a) M = 0, (b) 0.12, (c) 0.15, and (d) 0.17.

Table B.2: The travel time of a sound wave from the source in position 8 to the center of the phased array in position 2, and the distance between the actual source and the apparent source located with conventional beamforming at the flow speeds, M = 0.12, 0.15, and 0.17.

Mach Number	Theoretical Shift (in)	Exp. Shift (in)	Error (%)
0.12	4.198	4.1	2.4
0.15	5.885	5.8	1.5
0.17	6.67	6.7	0.4

The formulation of the Green's function accounting for the refraction effect was shown to be in very good agreement with experimental results. This new Green's function was implemented in the beamforming code. The cases shown in Figure B.2 were post-processed with the revised beamforming code. Figures B.3a through d depict the beamforming maps of the point source in position 8 with the microphone phased array in position 2. The point source was located by the array near x = 0 for all the cases presented, suggesting the validity of the new beamforming code.

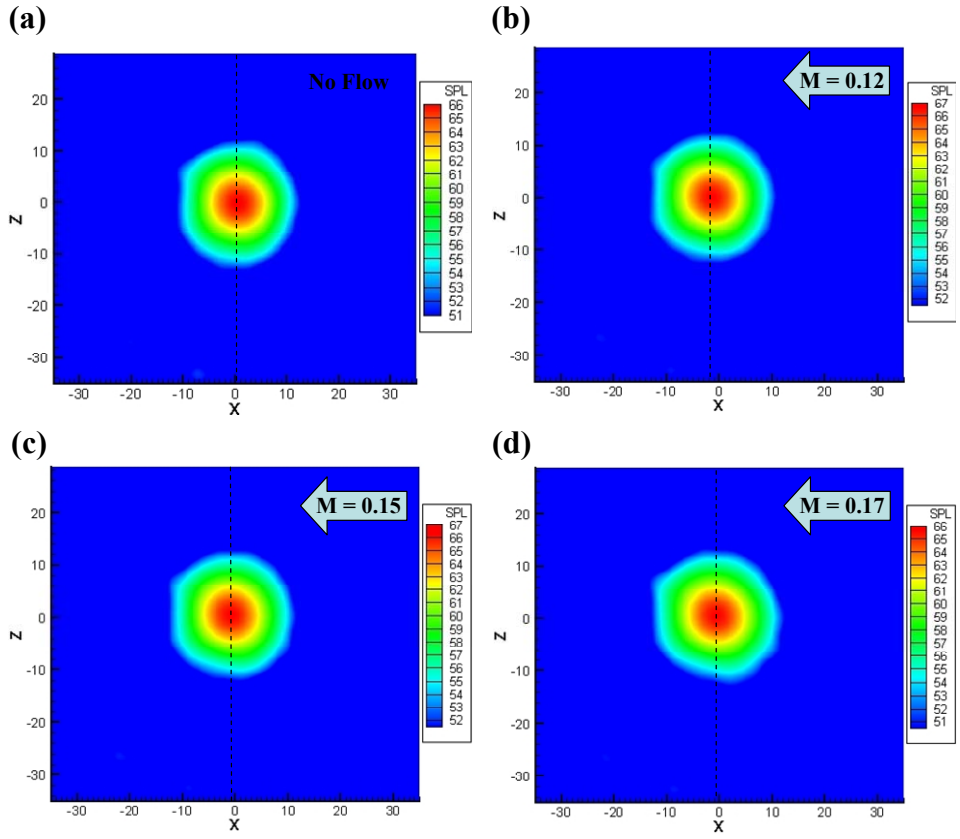

Figure B.3: Beamforming maps of the point source in position 8 at f = 13004 Hz as obtain with a beamforming code that accounts for flow. Data was collected with the microphone phased array in position 2 at speeds, (a) M = 0, (b) 0.12, (c) 0.15, and (d) 0.17.

B.2 Amplitude calibration of the array

In this section the procedure for the calibration of the array levels is presented. In a preliminary subsection, results on the characterization of the "speaker-pipe" source are shown.

B.2.1 Sound characteristics of the "speaker-pipe" source

Experiments were conducted in an anechoic chamber to determine the sound characteristics of the "speaker-pipe" source used to calibrate the array for amplitude.

Figure B.4 is a photograph of the experimental setup for measuring the "speaker-pipe" source radiation. The source was standing vertically in the anechoic chamber. An L-beam mounted 12 inches from the top of the speaker pipe supported a 43-inch diameter rim. The rim was a nearly perfect half-circle with an accuracy of ±1/8 inch. The microphone position could be adjusted so that the distance between the tip of the "speaker pipe" and the microphone was exactly 20.5 inch for all test configurations. The rim supported a 1/4-inch diameter B&K microphone that was moved by increments of 12° along the rim (angle α) and rotated around the center line of the "speaker pipe" by increments of 45° (angle β). Therefore, sound could be measured over a semi spherical surface.

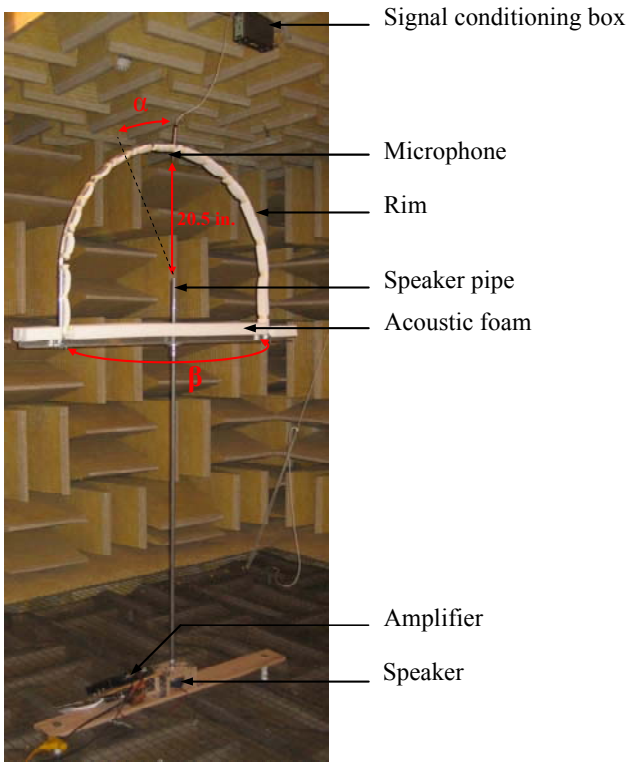

Figure B.4: A photograph of the test setup for determining the sound characteristics of the point source.

Figure B.5 depicts the SPL 1/12th octave band measured 20.5 inches from the source for $\alpha = 0$ and $\beta = 0$, as a function of frequency. Note that the frequency response is nearly flat from 9 kHz to 20 kHz. The frequency range of the speaker was 800 - 20 kHz. However, the figure indicates that results are not workable for frequencies smaller than 2150 Hz. This does not represent an issue since the beamforming maps of the gear noise were carried out for model-scale frequencies larger than 4000 Hz.

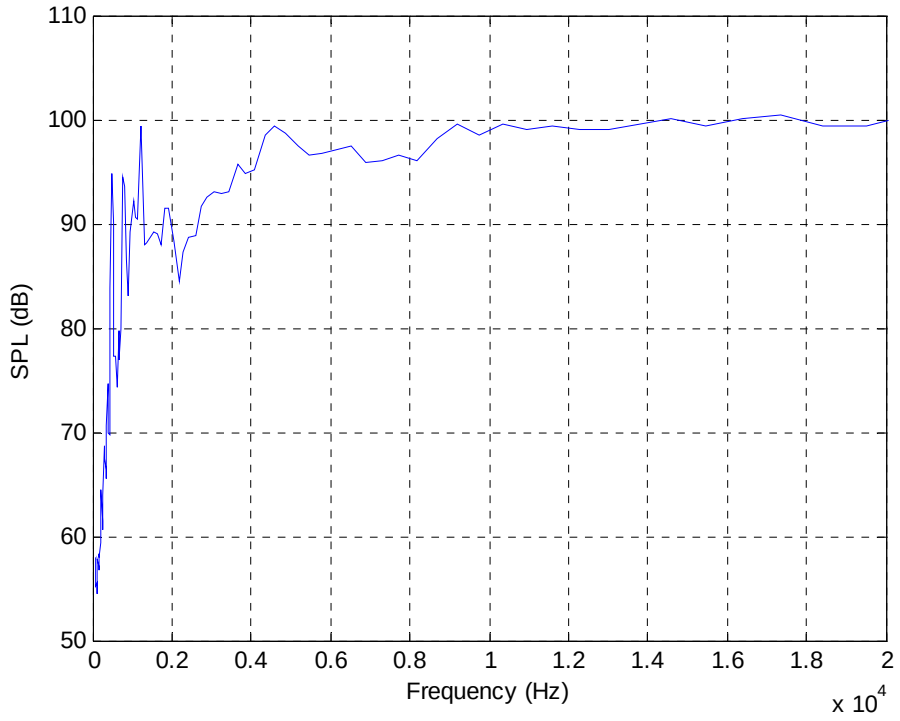

Figure B.5: The sound pressure level in 1/12th octave band measured 20.5 inches from the point source, with $\alpha = 0$ and $\beta = 0$, as a function of frequency.

Figures B.6a and b depict the SPL as a function of β for two 1/12th octave band frequencies, i.e. $f_c = 4339$ and 12937 Hz, respectively. Results are presented for three α angles denoted as solid circles ($\alpha = 12°$), solid squares ($\alpha = 48°$) and solid triangles ($\alpha = 84°$). The figure indicates that, for a fixed angle α, the SPL is virtually constant as the angle β varies.

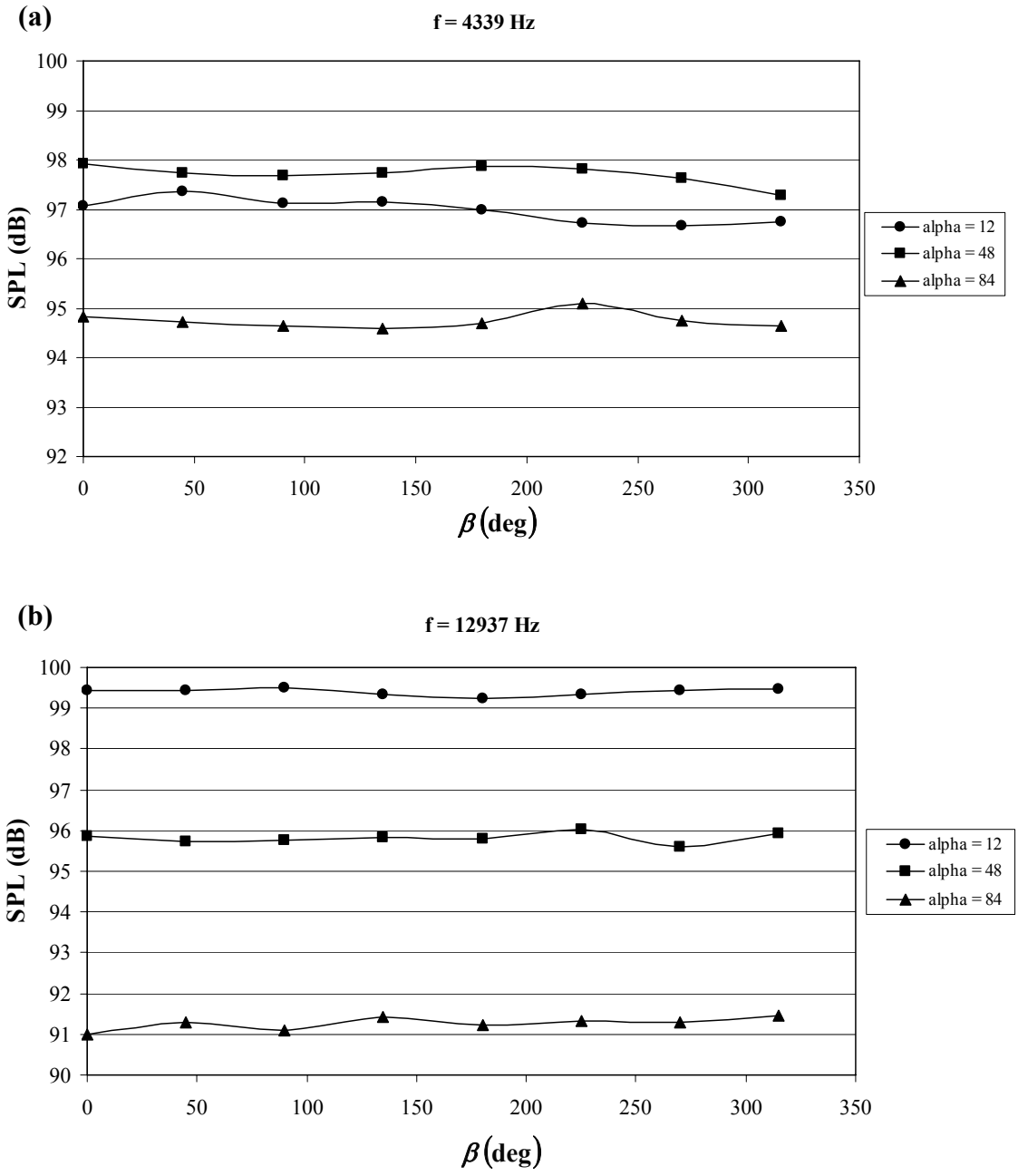

Figure B.6: The sound pressure level in 1/12th octave band with central frequencies, (a) f_c = 4339 and (b) 12937 Hz, measured 20.5 inches from the point source as a function of the angle beta. The solid circles, solid squares and solid triangles correspond to $\alpha = 12°$, 48° and 84°, respectively.

Figure B.7 depicts the SPL 1/12th octave band measured 20.5 inches from the point source as a function of the angle α when $\beta = 0$. The hollow diamonds, hollow squares, hollow triangles and hollow circles correspond to the central frequencies f_c = 4339, 7298,

12937, and 16392 Hz, respectively. The figure suggests that increasing the frequency and the angle α results in a significantly lower SPL.

These results demonstrate that the "speaker-pipe" source does not produce perfect spherical waves. However, the results from this test provide a well calibrated source to be used for amplitude and phase calibration of the phased array.

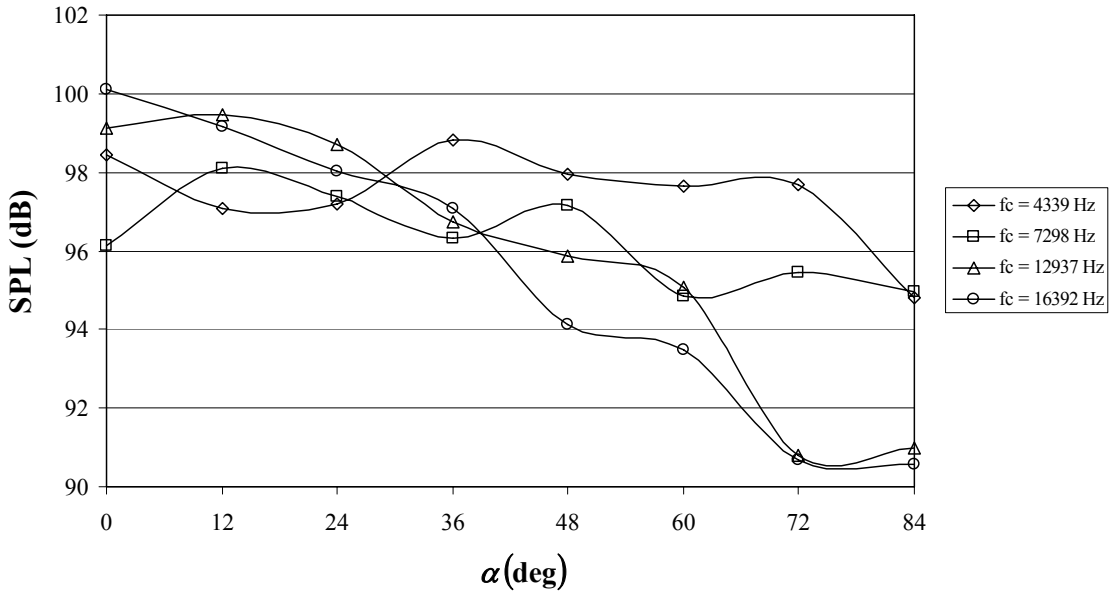

Figure B.7: The sound pressure level in 1/12th octave band measured 20.5 inches from the point source as a function of the angle α when β = 0. The hollow diamonds, hollow squares, hollow triangles and hollow circles correspond to the central frequencies f_c = 4339, 7298, 12937, and 16392 Hz, respectively.

B.2.2 Procedure for the calibration for the array levels

The calibration of the array was based on a calibration of the beamforming output and not an individual calibration of each microphone of the array. First, measurements of a known "monopole-like" source are carried out with the non-calibrated phased array. The beamforming maps of the noise generated by the source are integrated to provide the levels of the source. Since the array is not calibrated, the levels measured are not the actual ones. Then, the levels of the source at the center of the array are determined analytically. Since the characteristics of the source are known, the actual levels of the source may be obtained by extrapolation. The difference between the extrapolated levels and integrated-spectra levels defines the correction factor for the array levels in the

absence of flow, Δ_{AL}. An additional correction factor may be carried out to account for flow effects. The levels of the source are determined without and with flow, using the integrated spectra. The difference between the levels without and with flow defines the correction factor for flow effects, Δ_{Flow}. Ultimately, the correction factors are added to the beamforming output such that,

$$SPL_{True} = SPL_{Measured} + \Delta_{AL} + \Delta_{Flow}. \quad (B.1)$$

These correction factors are dependent on frequency and on the position of the source relative to the array.

The experimental setup for the calibration tests was the same as the one shown in Figure B.1. The configurations listed are listed in Table B.1. The calibration of the array was performed in the semi-anechoic wind tunnel. The presence of the Kevlar window and the hard-wall was thus accounted for in the calibration procedure.

a. Correction factor for array levels in the absence of flow

Figures B.8a through f depict the difference between the predicted SPL and the integrated spectra of the "speaker-pipe" source as a function of frequency, for the array and source in positions, (a) 2 and 3, (b) 3 and 3, (c) 2 and 8, (d) 3 and 8, (e) 2 and 13, and (f) 3 and 13.

Ideally, each grid point of the scanning grid encompassing the landing gear should be calibrated. However, this is not feasible in practice. As a coarse approximation, only results from source positions 3 and 8 were used. The source positions 3 and 8 correspond approximately to the center of beamforming maps of the landing gear noise on the "strut" and "truck" planes, respectively.

For example, the map on the "truck" plane obtained at 10 kHz (model-scale frequency) with the array in the far-field straight under the gear (array position 2) and no flow in the test section, will be added Δ_{AL} = 16.2 dB (Figure B.8c).

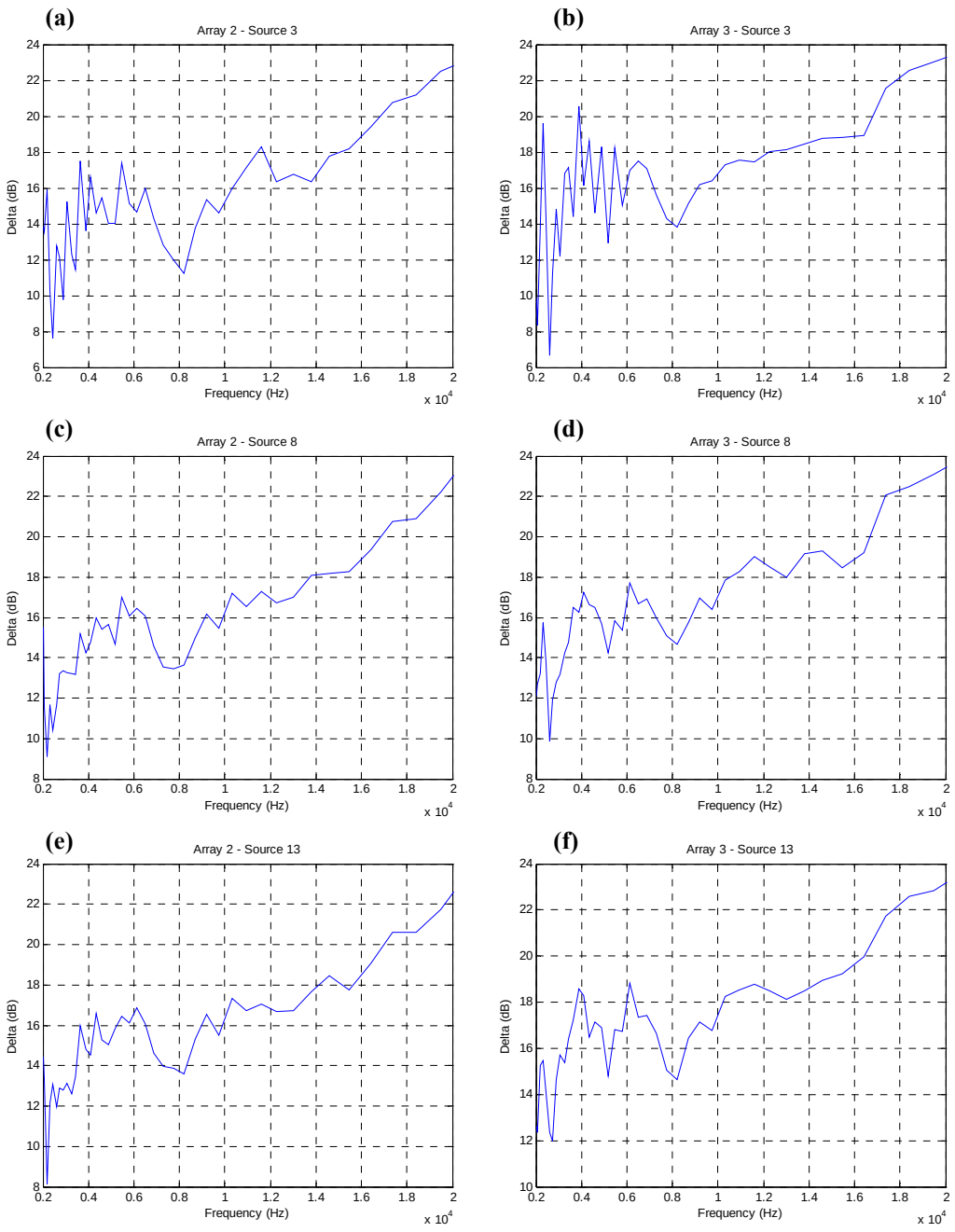

Figure B.8: Difference between the predicted SPL and the integrated spectra of the point source as a function of frequency, for the array and source in positions, (a) 2 and 3, (b) 3 and 3, (c) 2 and 8, (d) 3 and 8, (e) 2 and 13, and (f) 3 and 13.

b. Correction factors for flow effects

Figure B.9 depicts the difference between integrated spectra of the "speaker-pipe" source at M = 0.12 and M = 0 (blue curve), at M = 0.15 and M = 0 (red curve), and at M = 0.17 and M = 0 (green curve), as a function of frequency. Figures B.9a through f

correspond to the positions of the array and source, 2 and 3, 3 and 3, 2 and 8, 3 and 8, 2 and 13, and 3 and 13, respectively.

Note that for positions 8 and 13 of the source, the curves exhibit a peak around 5.5 kHz at M = 0.15 and around 6.5 kHz at M = 0.17. As mentioned in Section B.1.1, to minimize the deflection and vibration of the source against the air flowing in the test section, for positions 8 and 13 of the source in the test section in Figure B.1, strings connected the tip of the source to the hard wall of the test section. The diameter of the strings was nearly 2 mm. The vortex shedding frequency is defined as $f = S_t U_\infty / l$, where S_t is the Stoühal number, U_∞ is the free-stream airspeed, and l is the characteristic length of the body equal to the vortex separation distance [40]. The vortex shedding frequency of the string is f = 5402 Hz at M = 0.15 and f = 6123 Hz at M = 0.17, which correspond to frequencies where the peaks are observed. The correction factors for frequencies between f = 4500 and 9000 Hz may be obtained by extrapolation.

For example, the map on the "truck" plane obtained at 10000 Hz with the array in the far-field straight under the gear (array position 2) at wind-tunnel speed M = 0.17, will be added Δ_{AL} = 16.2 dB (Figure B.8c) and Δ_F = 0.9 dB (Figure B.9c – green curve).

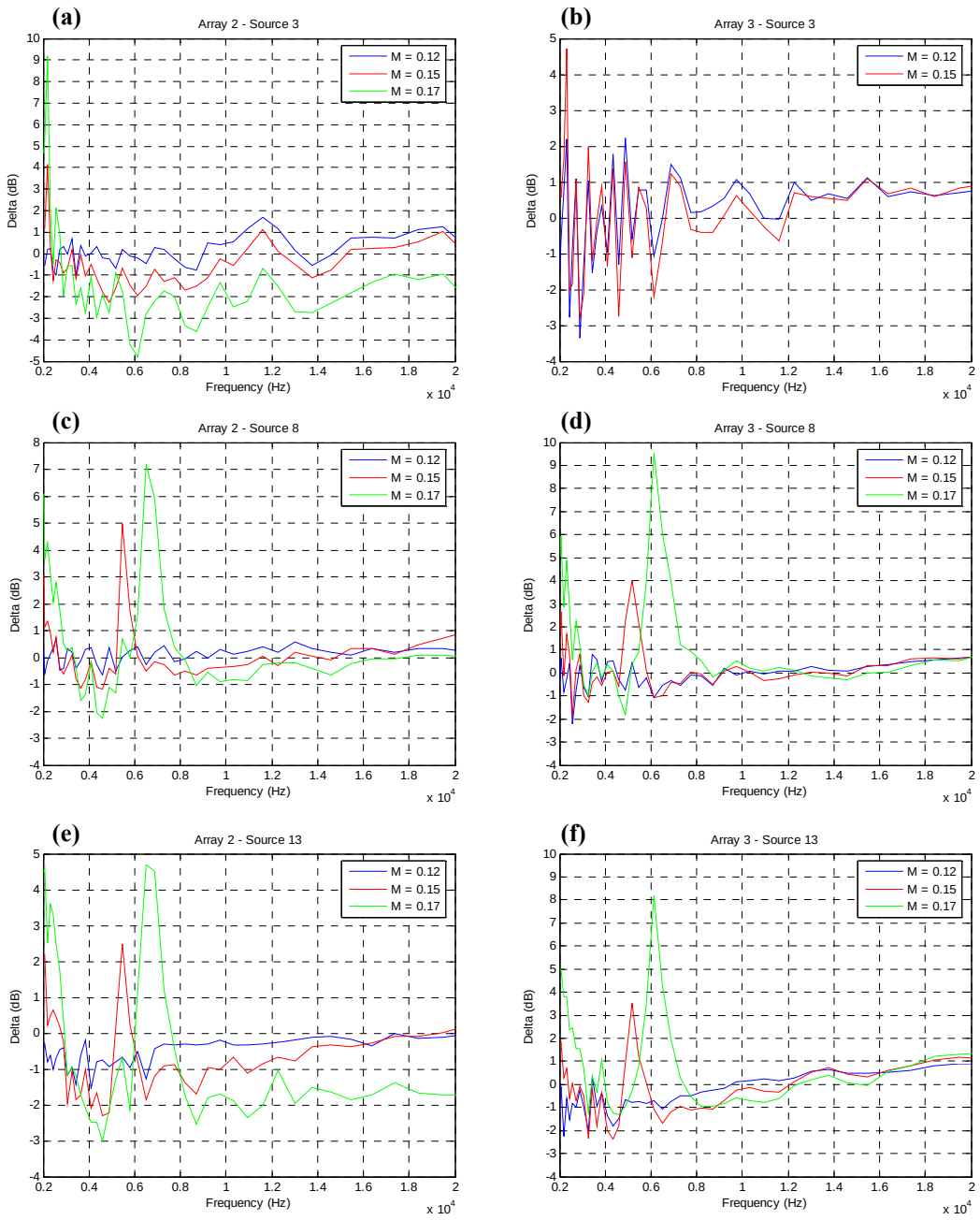

Figure B.9: Difference between integrated spectra at M = 0.12 and M = 0 (blue curve), at M = 0.15 and M = 0 (red curve), and at M = 0.17 and M = 0 (green curve), as a function of frequency. Figures a through f correspond to the array and source in positions, 2 and 3, 3 and 3, 2 and 8, 3 and 8, 2 and 13, and 3 and 13, respectively.